THE UNIVERSITY OF CHICAGO

PHOTOSYNTHETIC DESIGN PRINCIPLES FOR ULTRAFAST ENERGY TRANSFER PROCESSES

A DISSERTATION SUBMITTED TO
THE FACULTY OF THE DIVISION OF THE PHYSICAL SCIENCES
IN CANDIDACY FOR THE DEGREE OF
DOCTOR OF PHILOSOPHY

DEPARTMENT OF CHEMISTRY

BY
SARA HESS SOHAIL

CHICAGO, ILLINOIS
MARCH 2020

To my husband, Faraz, and my daughter, Talia.

Look deep into nature, and then you will understand everything better.

-Albert Einstein

TABLE OF CONTENTS

LIST OF FIGURES

LIST OF TABLES

ACKNOWLEDGMENTS

I was supported by a National Defense Science and Engineering Graduate (NDSEG) Fellowship from the Department of Defense, Air Force Office of Scientific Research (AFOSR). The research presented here was additionally funded by the Vannevar Bush Faculty Fellowship program and AFOSR, and completed in part with resources provided by the National Science Foundation MRSEC.

I am grateful to everyone who has helped me achieve this PhD. First, I would like to thank my incredibly supportive research advisor Professor Gregory Engel. Thank you for enabling me to forge an unorthodox path, for offering scientific and professional guidance when needed, and for giving me the freedom to design my own projects and experiments, many of which were high risk. Thank you for believing in my capabilities and my ideas.

I am grateful to my committee members, Professor Andrei Tokmakoff and Professor Suri Vaikuntanathan, for their guidance and mentorship.

I would like to thank my collaborators in the Hunter Group, Prof. C. Neil Hunter, Elizabeth Martin, Dr. Andrew Hitchcock, and Dr. Craig MacGregor-Chatwin for generously providing me with mutant *Rba. sphaeroides* cells and mutant *Synechocystis* sp cells and membrane fragments. I also thank my collaborators, Dr. Joseph Melinger and Dr. Paul Cunningham for designing the DNA-dye constructs.

I am so thankful that I was able to conduct my research with the support and collaboration of an amazing group of labmates in the Engel Group. Thank you for giving me a hand, being a second set of eyes, talking through problems, and teaching me to be a better scientist. Thank you to my mentors, Dr. Sara Massey and Dr. Peter Dahlberg, who gave me their confidence from the beginning. To my peers, Richard Mazuski and Ryan Wood, I am happy to have had you to share these experiences with. To my fellow Condon labmates, Po-Chieh Ting, Jacob Higgins, Nicholas Cleland, Dr. Marco Allodi, and Lawson Lloyd, thanks for making the lab a fun and supportive environment. Thank you to Dr. Karen Watters for

her scientific editing and helping me improve my own writing.

I am grateful to my undergraduate research advisor, Prof. Casey Londergan, for introducing me to scientific research and believing in me from the start. Thank you for your continuous support and encouragement.

I owe a special thank you to my parents, Debbie Kenyon and Peter Hess, for teaching me to believe I could do anything I wanted and for supporting my choices. Thank you for providing me with the opportunities to get to where I am today. I am lucky to have you cheering me on. I want to thank my sister, Rachel Hess, for her continuous encouragement and moral support. Thank you to my daughter, Talia, you bring me so much joy and make me more fulfilled than you will ever know. Faraz, my amazing husband, you bolster me to go after what I want and are always there no matter the outcomes. I am grateful for your flexibilty, respect, unwavering support, and all the happiness you bring me.

ABSTRACT

As chemists, we often aim to solve each new problem with a unique molecule. Biology takes the opposite approach. Photosynthetic organisms have evolved to survive in diverse habitats by densely packing many of the same pigment molecules to spatially delocalize excitations and support vibronic coherence between pigments. Pigment-pigment and pigment-environment interactions tune chromophore absorption to capture broad wavelengths of light. We seek to understand the design principles that govern the ultrafast dynamics of light harvesting on a femtosecond (10^{-15} s) timescale and apply these design principles to develop molecular artificial light harvesting systems. In this thesis, I present two-dimensional electronic spectra on living cells of the anoxygenic purple bacterium *Rhodobacter sphaeroides*, the fused antenna/reaction center photosystems from the oxygenic cyanobacterium *Synechocystsis* sp. PCC 6803 in their native membrane environment, and DNA-dye constructs that are candidates for artificial light harvesting applications. In *Rhodobacter sphaeroides*, we collected the first fully absorptive two-dimensional electronic spectra of a living cell, revealing a sub-100 fs intracomplex relaxation in light harvesting complex 1. We present a synthetic system of coupled cyanine dyes that supports vibronic coherence, a photosynthetic design principle implicated in efficient exciton energy transfer in photosynthetic organisms, by tethering the dyes to a DNA scaffold. It is the first report of using DNA to engineer vibronic coherence. We use singlet-singlet annihilation to track inter-complex energy transfer between isoenergetic complexes in intact thylakoids prepared from wild-type and mutant cyanobacterial cells. We observe diffusion-limited trapping behavior between red Chl pools on neighboring Photosystem I monomers in these *Synechocystis* sp. PCC 6803 membrane fragments. We also present the first two-dimensional electronic spectra of living cyanobacteria. This represents a major advance in *in vivo* ultrafast spectroscopy, opening the door to studying regulatory and response mechanisms in these more complex oxygenic phototrophes. Future planned experiments include the investigation of the effects of light quantity and

quality on the organization of the photosynthetic machinery in cyanobacteria, experiments to elucidate the molecular mechanics and quantum dynamics of photoprotective quenching in green algae, and engineering efficient energy transfer aided by vibronic coherence in a synthetic dye-DNA assembly.

CHAPTER 1

INTRODUCTION TO PHOTOSYNTHETIC DESIGN PRINCIPLES FOR ULTRAFAST PROCESSES

1.1 Photosynthetic Design Principles for Energy Transfer

Over the past 2.5 billion years, photosynthetic organisms have evolved to harvest solar excitations with near unity quantum efficiency. These organisms use a set of highly conserved design principles to maximize photosynthetic efficiency and minimize loss. Photosynthetic organisms contain reaction centers (RC), where trapping of solar excitations occurs and photochemistry is initiated, and antenna complexes, whose role is to capture solar radiation and transfer it to the reaction center. Efficient energy transfer through networks of antenna complexes to the reaction center is essential. Photosynthetic organisms have a myriad of strategies for optimizing this transfer process that involve both classical and quantum energy transfer processes.

All photosynthetic organisms use an energetic funnel to harvest solar energy and transfer excitations to the reaction center. This entire process occurs on a tens of picoseconds timescale, orders of magnitude shorter than the nanosecond lifetime of the pigment fluorescence. Photosynthetic organisms use densely packed chromophores in pigment-protein complexes containing many molecules of the same pigment to create this energetic gradient. Chromophore absorption is tuned through pigment-pigment interactions and interactions between the pigments and the surrounding protein scaffold. These design principles are conserved across anoxygenic phototrophs, cyanobacteria, algae, and green plants, though the gradient of the funnel can vary. The depth of the energetic funnel and how spatially separated the highest energy absorbers are from the trap influence how strongly the organism relies on classical or quantum transport methods (Figure 1.1).

Photosynthetic design principles can inform approaches to synthetic light harvesting.

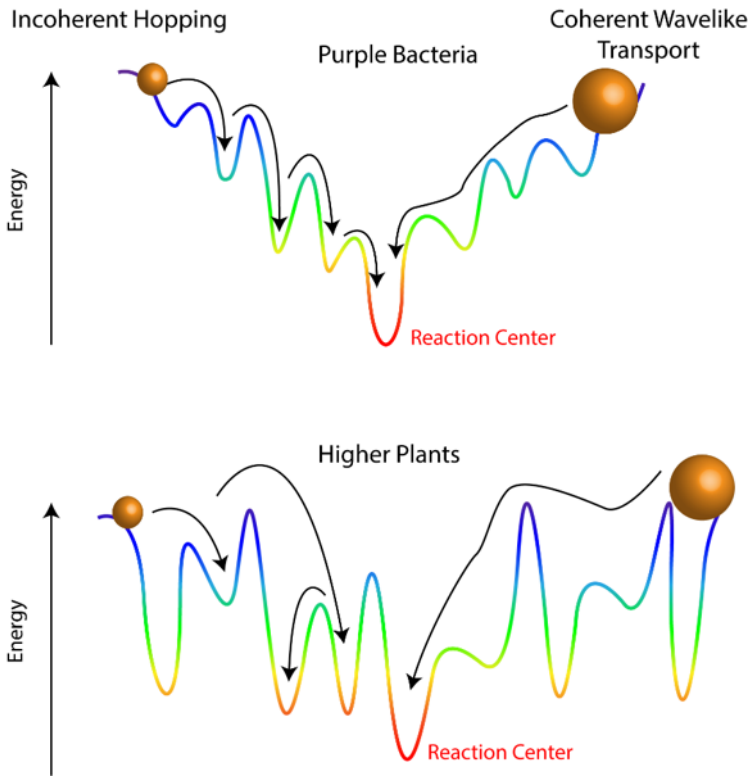

Figure 1.1: Photosynthetic energy transfer is a balance between incoherent hopping and wavelike (quantum) transport. (Top) In purple bacteria, there is a steep energetic and spatial funnel towards the reaction center. Pigments closer to the reaction center absorb at lower energies. Incoherent hopping could suffice in this energetic landscape with quantum transport aiding the transfer process. (Bottom) The energetic landscape in higher plants is much more rugged. While the reaction center offers an energetic trap, the pigments with the highest transition energies are not the most distal from the reaction center. Quantum coherent transport is likely much more important to traverse this energetic landscape effectively. Adapted with permission from [1]

.

This thesis will focus on light-harvesting and energy transfer in the purple bacterium *Rhodobacter sphaeroides* (*Rba. sphaeroides*) and the cyanobacterium *Synechocystis* sp. PCC 6803 and how photosynthetic design principles can be used in DNA-based bio-mimetic light-harvesting devices.

1.1.1 Light Harvesting in Purple Bacteria

Purple bacteria such as *Rba. sphaeroides* are capable of anoxygenic photosynthetic or chemotrophic growth making them excellent model organisms for studying photosynthetic energy transfer. [2] The antenna complexes in *Rba. sphaeroides* are completely spectrally resolved from each other which makes following energy transfer pathways in this organism much more straightforward than following energy transfer pathways in cyanobacteria, algae, or green plants. In these oxygenic phototrophs, the absorption of the photosynthetic antenna and reaction center complexes are nearly completely overlapping. [3]

Rba. sphaeroides contains a peripheral light-harvesting antenna, Light-Harvesting Complex 2 (LH2), and a core antenna, Light-Harvesting Complex 1 (LH1). LH1, along with a small protein complex PufX, surrounds the RC. Energy is absorbed by LH2, transferred to LH1 and then onto the RC. LH2 contains two rings of bacteriochlorophyll *a* (BChl *a*). The B800 ring is comprised of 9 weakly coupled ($\sim$20cm^{-1}) BChl *a* pigments. It is named for its characteristic absorption at 800 nm. The B850 ring contains 18 strongly coupled ($\sim$300 cm^{-1}) BChl *a* pigments. The strong coupling between the pigments red shifts their absorption to 850 nm. [7] LH1 exists *in vivo* predominately as an S-shaped dimer, with each monomer containing 28 strongly coupled ($\sim$300 cm^{-1}) BChl *a* pigments. The strong coupling in LH1 shift its absorption to 875 nm and, as such, its monomeric rings of BChl *a* are named B875. [8] Each B875 ring of BChl *a* surrounds the bacterial RC. The special pair of BChl *a* in the RC absorb at 870 nm; therefore transfer from B875 to the RC is slightly energetically unfavorable (65 cm^{-1} uphill). [8, 9] Energy transfers from B800 to B850 within

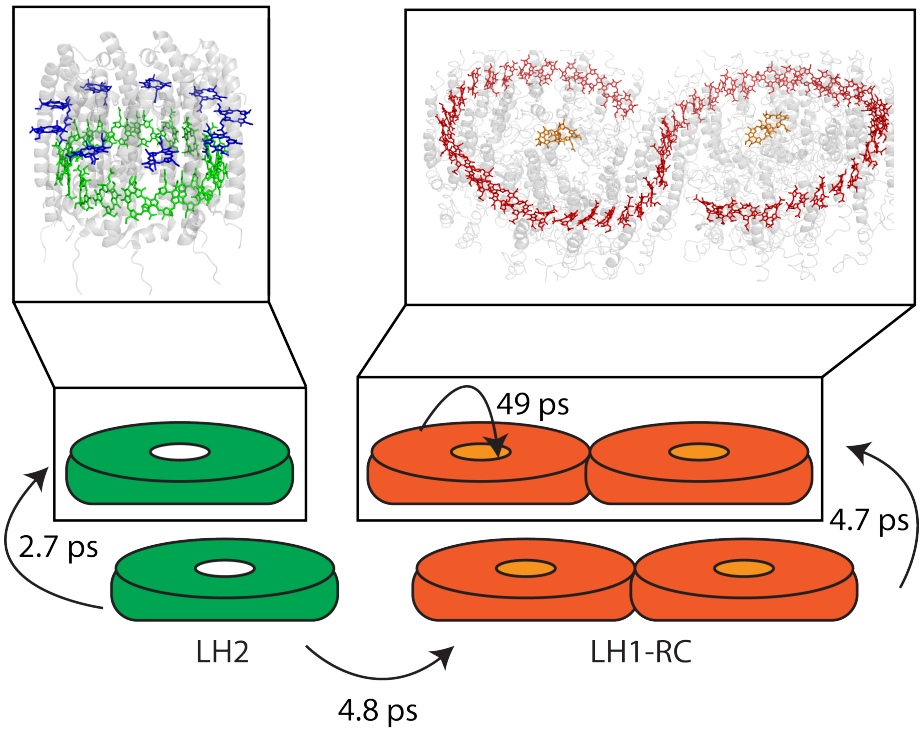

Figure 1.2: Energy transfer rates between light-harvesting complexes in the purple bacteria *Rba. sphaeroides*. Inter-complex transfer rates were determined by Dahlberg, et al. [4] Crystal structures for LH2 (PDB ID: 1KZU [5]) and the LH1-RC-PufX dimer (PDB ID: 4V9G [6]) are shown above the cartoons corresponding to each light-harvesting complex.

LH2 in 700 fs. Inter-complex B850 transfer occurs within a few picoseconds, as does transfer from B850 to B875. The uphill transfer from B875 to the RC takes tens of picoseconds. [4]

1.1.2 Light Harvesting in Cyanobacteria

Cyanobacterial photosynthesis, unlike purple bacterial photosynthesis, is oxygenic. Absorbed excitations are transferred to the RC where charge separation and primary photochemistry occur. Oxygen gas is produced as a byproduct of water oxidation. [10] Cyanobacteria, algae, and plants all contain the core fused antenna/reaction center complexes, Photosystem I (PSI) and Photosystem II (PSII), and peripheral light-harvesting complexes. PSI and PSII are transmembrane complexes embedded in intracellular stacks of membranes known as thylakoids. The similarities in light-harvesting design principles between cyanobacteria and higher photosynthetic organisms (plants and algae) make cyanobacteria a good model system for oxygenic photosynthesis.

In plants and algae, peripheral light-harvesting antenna are also embedded in the thylakoid membrane. Cyanobacteria do not have these additional transmembrane light-harvesting complexes, but they use an extra-membrane antenna called the phycobilisome (PBS) to funnel excitations to PSI and PSII. [11] The PBS is a spatial and energetic funnel that transports harvested excitations to the RCs. The PBS is comprised of 6-8 rods fanned around a core containing 2-5 cylinders of 1-2 hexamers of the phycobiliprotein allophycocyanin (APC). The makeup of the rod is species-dependent, but the most distal phycobiliproteins absorb the highest energy photons and the proximal rod phycobiliproteins absorb lower energy photons. The proximal phycobiliproteins in the rods are commonly phycocyanin (PC), absorbing at 620 nm. The APC core is the lowest energy site, a trap within the PBS, absorbing at 670 nm. [12]

The PBS can couple to both PSI and PSII. Excitations are transferred from the APC core of the PBS to the photosystems within 100-200 ps. [15, 16] The crystal structures of PSI and

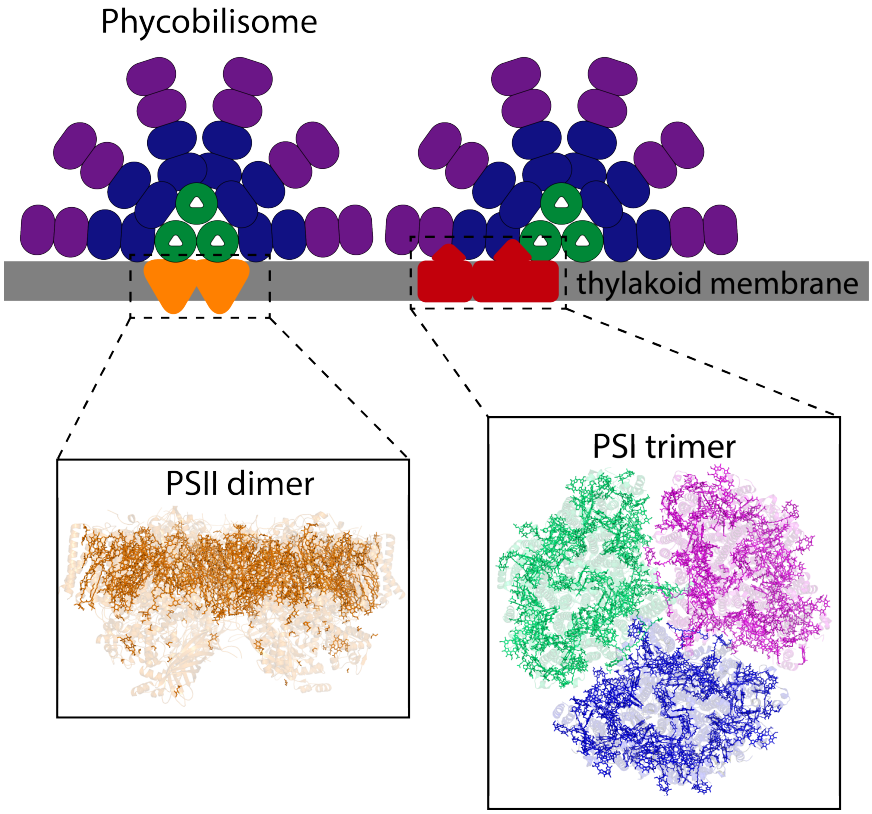

Figure 1.3: Cartoon of the peripheral and core light-harvesting complexes in the cyanobacteria *Synechocystis* sp. PCC 6803. The phycobilisomes contain phycobiliproteins phycoerythrin (purple) and phycocyanin (blue) in their rods. The phycobilisome core is composed of the phycobiliprotein allophycocyanin (green). The phycobilisomes are on the cytoplasmic side of the thylakoid membrane. They can associate with the fused antenna/reaction center complexes PSI and PSII. Crystal structures for the PSII dimer (PDB ID: 3WU2 [13]) and the PSI trimer (PDB ID: 1JB0 [14]) are shown beneath their cartoon representations.

PSII are shown in Figure 1.3. PSI exists *in vivo* in dynamic equilibrium between monomers and trimers, though it is believed that the trimeric form dominates. [17] Each PSI monomer contain 96 Chl molecules. PSII exists as a dimer with each monomer containing 35 Chl molecules. [12, 18] PSII contains the oxygen-evolving complex, the site of water oxidation and molecular oxygen evolution. [11] The PSI:PSII ratio is dependent on illumination intensity during cell growth, but ranges between 2:1 and 10:1. [11] PSI is the dominant Chl source in cyanobacteria.

1.2 Theories of Photosynthetic Energy Transfer

Photosynthetic light-harvesting has an extremely high efficiency demand. Excitations must be transported over nanometer length scales with high fidelity. Energy transfer in photosynthesis can be described by three distinct theories of energy transfer: Förster Theory, Redfield Theory, and Quantum Coherent Transport. [19] Which of the three theories applies to a given energy transfer event depends on the inter-pigment coupling. When the inter-pigment coupling is weak, Förster Theory is applicable. When the inter-pigment coupling is strong, Redfield Theory is applicable. In the intermediate regime, the system must be treated quantum mechanically as the coherent evolution of the system affects transfer dynamics.

1.2.1 Förster Resonance Energy Transfer

Förster Resonance Energy Transfer (FRET) describes photosynthetic energy transfer when weak coupling between pigments whose dipole-dipole interactions give way to excitation hopping between chromophores. FRET is distance dependent, with energy transfer efficiency rapidly diminishing with increasing distance. The first order FRET rate constant, based on the dipole-dipole approximation is given by:

$$k_T(r) = \tau_D^{-1}(\frac{R_0}{r})^6 \tag{1.1}$$

In Equation 1.1, τ_D is the fluorescence lifetime of the donor molecule, R_0 is the distance at which energy transfer between the two pigments is 50% efficient, and r is the distance between the donor and acceptor pigments. R_0, the Förster radius, is a function of the spectral overlap between the donor and acceptor pigments and dependent on the relative orientation between donor and acceptor transition dipoles. [18]

$$R_0^6 = \frac{8.79 \times 10^{-5} J \kappa^2}{n^4} \tag{1.2}$$

J in Equation 1.2 is the spectral overlap integral and κ^2 is a measure of the relative orientation between donor and acceptor transition dipoles. [11]

FRET theory can be used to calculate photosynthetic energy transfer rates when inter-chromophore coupling is weak. However, in photosynthetic pigment-protein complexes the pigment concentration is extremely high. This dense packing of chromophores leads to the breakdown of the point dipole approximation used in FRET. Close proximity also causes strong interactions in many cases, requiring additional theories of energy transfer. [3]

1.2.2 Redfield Theory

Redfield theory of energy transfer applies when the coupling between pigments is significantly stronger than the coupling between the pigments and the surrounding protein scaffold. Strong inter-pigment interactions leads to excitons, delocalized excited states. When inter-chromophore coupling is large, we can no longer think of excitations as localized on specific pigments, but as superpositions of excitations at different, but coupled, molecular sites. [3, 19] When applying Redfield theory, we work in the *exciton basis*, rather than the '*site basis*.

1.2.3 Quantum Coherent Energy Transfer

Considering photosynthetic energy transfer in the framework of Förster Theory or Redfield Theory neglects the quantum mechanical nature of the excitation. The excitations are wavefunctions that can sample many pathways simultaneously as long as its phase is preserved. The process through which memory of its initial phase is lost is known as dephasing. By measuring the interaction of the excitation with the system, we observe the excitation in a single state as we have collapsed the wavefunction. Collapse of the wavefunction (complete dephasing of the initial coherence) is also possible prior to the measurement through interactions with bath phonons. In the intermediate coupling regime, when coupling between pigments is on the same order as the coupling between the pigments and the surrounding protein, quantum coherence is necessary to explain energy transfer dynamics. [19]

Coherence can be broken up into two distinct categories, both of which occur during photosynthetic energy transfer processes. State coherences can be observed in a static measurement, as they are a superposition of individual states. Considering excitonic states instead of individual pigments is an example of a state coherence. A process coherence, in the context of photosynthetic energy transfer, characterizes the balance between the system's unitary and dissipative evolution. Unitary evolution is determined by inter-pigment coupling and dissipative evolution is determined by the system-bath coupling. When the system is excited with coherent light, coherent dynamics reflect how long the system can maintain a state coherence. [19] In our two-dimensional electronic spectroscopy experiments, as discussed in 1.3 and 2.1.1, process coherences are manifested as oscillatory dynamics in the waiting time. While sunlight is incoherent light, the property of process coherence is a fundamental design principle of photosynthetic complexes. Quantum coherences become relevant to photosynthetic energy transfer because the coherences drive energy transfer pathways and dynamics. [20]

1.3 Theory of Two-Dimensional Electronic Spectroscopy

In order to interrogate photosynthetic design principles, we turn to ultrafast optical spectroscopies. The focus of this thesis includes experiments using two-dimensional electronic spectroscopy and pump-probe (transient absorption) spectroscopy, both third order nonlinear spectroscopies. I will present a brief theoretical description of these optical techniques to provide a foundation for understanding the experimental work presented in this thesis. For more details on the theoretical framework of optical spectroscopy see [21] and [22].

1.3.1 Light-Matter Interactions

Molecular spectroscopies use light-matter interactions to interrogate molecular properties and behavior. We do not measure the molecular system directly, but rather its influence on the light with which it interacts. We use a semi-classical approach to light-matter interactions when describing optical spectroscopies, treating the light as a classical, oscillating electromagnetic wave and the electronic and vibrational states of the molecular system quantum mechanically. The interaction between the incident electric field and the dipoles of the molecule can be mathematically defined as

$$\hat{W}(t) = -\hat{\mu}E(t) \tag{1.3}$$

In Equation 1.3, $E(t)$ is the classical electric field and $\hat{\mu}$ is the molecular dipole operator. The complete Hamiltonian of the system can be written in terms of $\hat{H}_0$, the Hamiltonian of the molecule in the absence of an incident electric field, and $\hat{W}(t)$:

$$\hat{H} = \hat{H}_0 + \hat{W}(t) \tag{1.4}$$

The time evolution of the wavefunction, $|\Psi\rangle$ follows the time-dependent Schrödinger equation,

$$i\hbar\frac{\partial}{\partial t}|\Psi\rangle = \hat{H}|\Psi\rangle \tag{1.5}$$

In the absence of an incident field, the solution of the overall Hamiltonian is

$$|\Psi\rangle = \sum_n c_n e^{-iE_n t/\hbar}|n\rangle \tag{1.6}$$

With the arrival of the laser pulse, the time evolution can be incorporated into Equation 1.6 using Equation 1.5. The coefficients, c_n, become time-dependent as the incident field couples the molecular eigenstates. The time-evolution of these coefficients is given by

$$\frac{\partial}{\partial t}c_m(t) = -\frac{i}{\hbar}\sum_n c_n(t)e^{-i(E_n-E_m)t/\hbar}\langle m|\hat{W}(t)|n\rangle \tag{1.7}$$

Equation 1.7 is a set of coupled differential equations that describes the time evolution of the wavefunction after interaction with the incident laser pulse of duration t. For a two-level system made of a ground state and an excited state equation, 1.7 can be tractably separated into two coupled equations:

$$\frac{\partial}{\partial t}c_1(t) = +\frac{i}{\hbar}c_g(t)e^{-i\omega_{ge}t}\langle e|\hat{\mu}|g\rangle E(t) \tag{1.8}$$

$$\frac{\partial}{\partial t}c_1(t) = +\frac{i}{\hbar}c_e(t)e^{+i\omega_{ge}t}\langle g|\hat{\mu}|e\rangle E(t) \tag{1.9}$$

In Equations 1.8 and 1.9, $\omega_{ge} = (E_e - E_g)/\hbar$ and $\langle g|\hat{\mu}|e\rangle$ is the transition dipole moment, μ_{eg}. After interaction with an impulsive laser pulse, we see that the system is in a superposition between the ground state, $|g\rangle$, and the excited state, $|e\rangle$. The time evolution of the wavefunction of the system after this interaction is

$$|\psi(t)\rangle = c_0 e^{-iE_g t/\hbar}|g\rangle + ic_1 e^{-iE_e t/\hbar}|e\rangle \tag{1.10}$$

The second term in Equation 1.10 encompasses the complex phase of this wavepacket.

This complex phase is determined by the phase of the incident laser pulse that created the coherent superposition between the ground and excited states. If all of the molecules in an ensemble have their phases synchronized with the laser pulse and the same time evolution, then a nonequilibrium charge distribution known as a macroscopic polarization ($P^{(1)}(t)$) has been generated by the coherently driven dipoles. The oscillating macroscopic polarization emits a field that can be detected experimentally and is mathematically governed by Maxwell's Equations.

$$\begin{aligned} P(t) &= \langle \mu \rangle = \langle \Psi(t) | \hat{\mu} | \Psi(t) \rangle \\ &= (c_g e^{iE_0 t/\hbar} \langle g| - i c_e e^{iE_e t/\hbar} \langle e|) \hat{\mu} (c_g e^{-iE_g t/\hbar} |g\rangle + i c_e e^{-iE_e t/\hbar} |e\rangle \\ &= c_g c_e \langle g|\hat{\mu}|e\rangle \sin(\omega_{ge} t) + c_g^2 \langle g|\hat{\mu}|g\rangle + c_e^2 \langle e|\hat{\mu}|e\rangle \end{aligned} \tag{1.11}$$

The final two terms in the final line of Equation 1.11 are time independent as they represent permanent dipoles and therefore do not contribute to the emitted field. The first term in the final line of Equation 1.11 describes the emitted field and is dependent on the transition dipole between the ground and excited states.

For a single light interaction interrogating a two-state system, the formalism described above is tractable; however, for multilevel systems in real experiments the system of coupled equations (Equations 1.8 and 1.9) is unmanageable mathematically. To handle multilevel systems, we use the density matrix formalism.

1.3.2 Density Matrix Formalism

The density matrix is another way to describe the wavefunction and is especially useful for time-dependent scenarios.The density matrix is defined as

$$\rho(t) \equiv |\psi(t)\rangle\langle\psi(t)| \tag{1.12}$$

For a statistical average of all the states in an ensemble, we can write

$$\rho = \sum_s p_s |\psi_s\rangle\langle\psi_s| \tag{1.13}$$

where p_s is the statistical probability that the system is in a given quantum state, $|\psi_s\rangle$. The diagonal elements of the density matrix are referred to as populations and they are the probability of occupying a given quantum state with energy E_n. The off-diagonal elements of the density matrix describe the evolution of coherent superpositions between two quantum states of energies E_n and E_m. The off-diagonal elements are referred to as coherences. The time-evolution of the density matrix is described by the Liouville-Von Neumann equation

$$\frac{\partial \rho}{\partial t} = \frac{-i}{\hbar}[H, \rho] \tag{1.14}$$

which results from combining the time-dependent Schrödinger equation with the definition of the density matrix. The expectation value of any observable can be calculated using the density matrix. We can then easily write the macroscopic polarization, the expectation value of the dipole operator, from Equation 1.11 using the density matrix formalism.

$$P(t) = Tr[\hat{\mu}\rho(t)] = \langle\hat{\mu}\rangle \tag{1.15}$$

The density matrix formalism will help us understand the signals detected in our 2DES experiments.

1.3.3 Third-order Nonlinear Spectroscopy

The incident electric fields in optical spectroscopy experiments are sufficiently weak, such that perturbation theory can be used to describe the optical response. 2DES is a third-order nonlinear spectroscopy in which three incident electric fields generate a macroscopic polarization. This is the third order polarization (the fourth term in the perturbative expansion

of the macroscopic polarization). The third order polarization is

$$P^{(3)}(t) = \int_0^\infty dt_3 \int_0^\infty dt_2 \int_0^\infty dt_1 E_3(t-t_3)E_2(t-t_3-t_2)E_1(t-t_3-t_2-t_1)R^{(3)} \quad (1.16)$$

the three time terms in equation 1.16 correspond to the time delays between the three pulses in the two-dimensional electronic spectroscopy experiment. Pulse 1 generates a coherence between the ground state and an excited state. The coherence evolves phase in a specific direction during the time interval τ, referred to as the coherence time (t_1 in equation 1.16). The arrival of pulse 2 ends the phase evolution by establishing a population between two excited or ground states or a coherence between two excited states. The newly established population or coherence evolves over the waiting time, T (t_2 in equation 1.16). During the waiting time, energy transfer between excited states can occur. Pulse 3 initiates another coherence between a ground and an excited states or two excited states, which, again, evolves phase in a specific direction this time over the time interval t, the detection time (t_3 in equation 1.16). [23, 24] The signal generated is a function of the three time delays, τ, T, and t, and is detected by heterodyning with an attenuated fourth pulse, the local oscillator (L.O.). [21, 25]

The third-order response function, $R^{(3)}$ in equation 1.16, written in terms of the three time delays in our 2DES experiment is

$$R^{(3)}(\tau, T, t) \propto -i\langle\hat{\mu}(t+T+\tau)[\hat{\mu}(T+\tau),[\hat{\mu}(\tau),[\hat{\mu}(0),\rho_{00}]]]\rangle \quad (1.17)$$

where ρ_{00} is the first diagonal element of the density matrix. The response function is only not equal to zero when all three time delays are greater than or equal to zero. This ensures that there is only a material response after interaction with the three laser pulses. While equation 1.17 gives the mathematical structure of the third-order response, it is more

tractable to account for the experimental signals using a diagrammatic representation of the third-order response.

Double-sided Feynman diagrams are graphical representations of the Liouville space pathways encompassed within the third-order response. Double-sided Feynman pathways for six types of 2DES signals for a three state system are shown in Figure 1.4. In these Feynman diagrams, arrows pointing toward the diagram are absorption events while those pointing away are emission events. Each arrow represents one of the four light matter interactions in a third-order spectroscopic experiment (interactions with three laser pulses and one generated from the oscillating macroscopic third-order polarization). Time moves upward in these diagrams. The sign convention is chosen such that signal emission is a negative wavevector ($-k_{sig}$). Negative wavevectors are represented by left-pointing arrows while positive wavevectors are represented by right-pointing arrows. The final state of the system must be a population. All signals that obey these rules will be emitted for a given pulse sequence, but signals are only collected in a single, phase-matched direction based on the experimental geometry. The phase-matching condition is determined by the sum of the wavevectors and is given by $k_{sig} = -k_1 + k_2 + k_3$ for our experiments.

The phase evolved during the detection time, t, can either have the same or opposite sign to that evolved during τ. When the system evolves phase with the same sign during the intervals τ and t, the signal generated is a nonrephasing free induction decay. When there is a reversal in the direction (sign) of phase evolution between the intervals τ and t, a rephasing photon echo signal is generated. [21, 26] Figure 1.5 depicts the phase evolution and signal emission for rephasing and nonrephasing signals. Figure 1.4 shows Feynman pathways for the third-order rephasing and nonrephasing stimulated emission, ground state bleach, and excited state absorption signals. Collection of both the rephasing and nonrephasing signals is important as their summation gives the fully absorptive 2DES spectrum. In the rephasing or nonrephasing 2DES spectra, there are unresolved absorptive and dispersive contributions

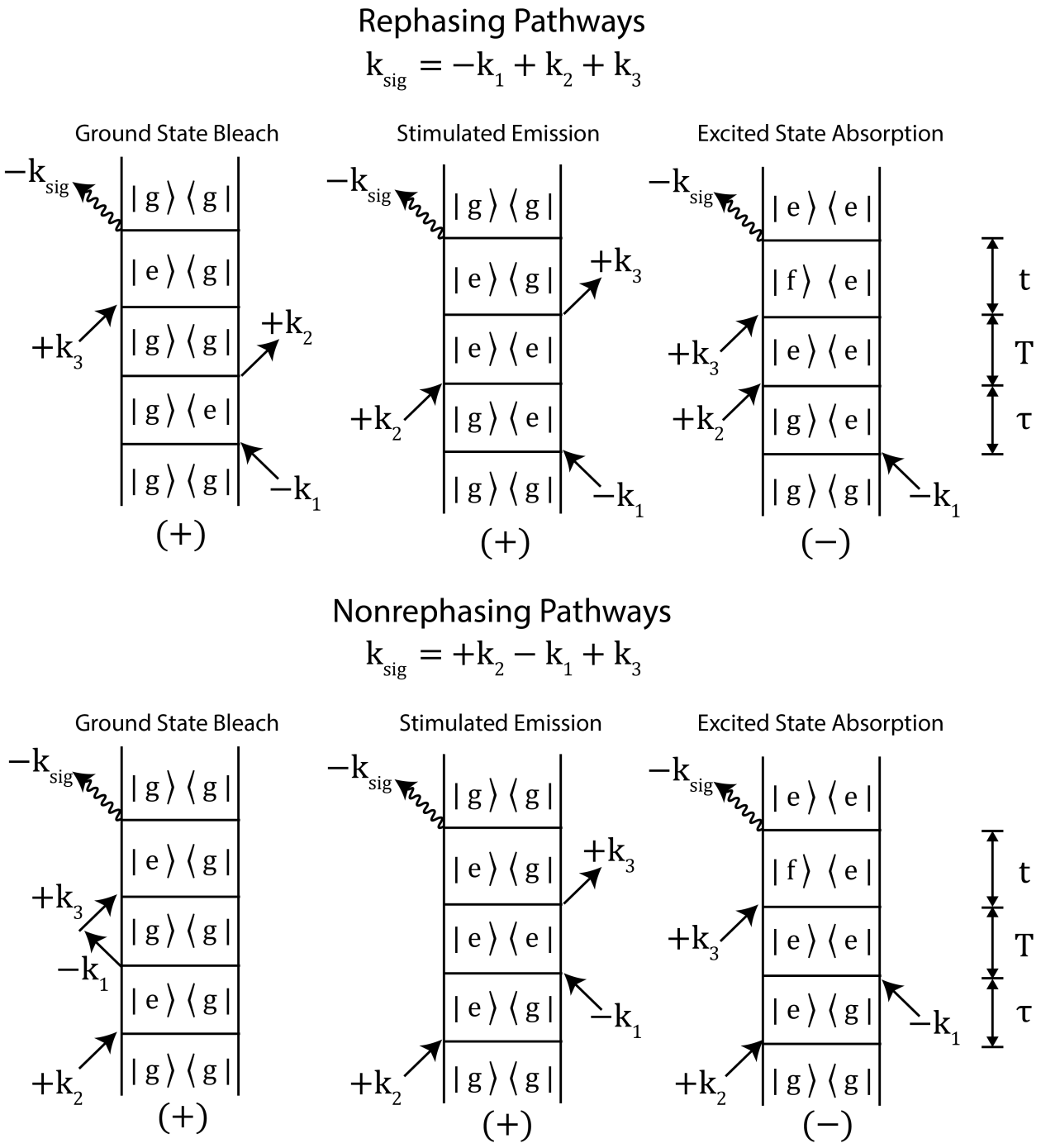

Figure 1.4: Double-sided Feynman pathways for rephasing photon echo signals (top row) and nonrephasing free induction decay signals (bottom row). Three types of signals are generated corresponding to ground state bleach (left), stimulated emission (center), and excited state absorption (right) pathways. The inverse time ordering of pulses 1 and 2 in rephasing and nonrephasing pathways enables the photon echo and free induction decay signals to be emitted in the same phase-matched direction.

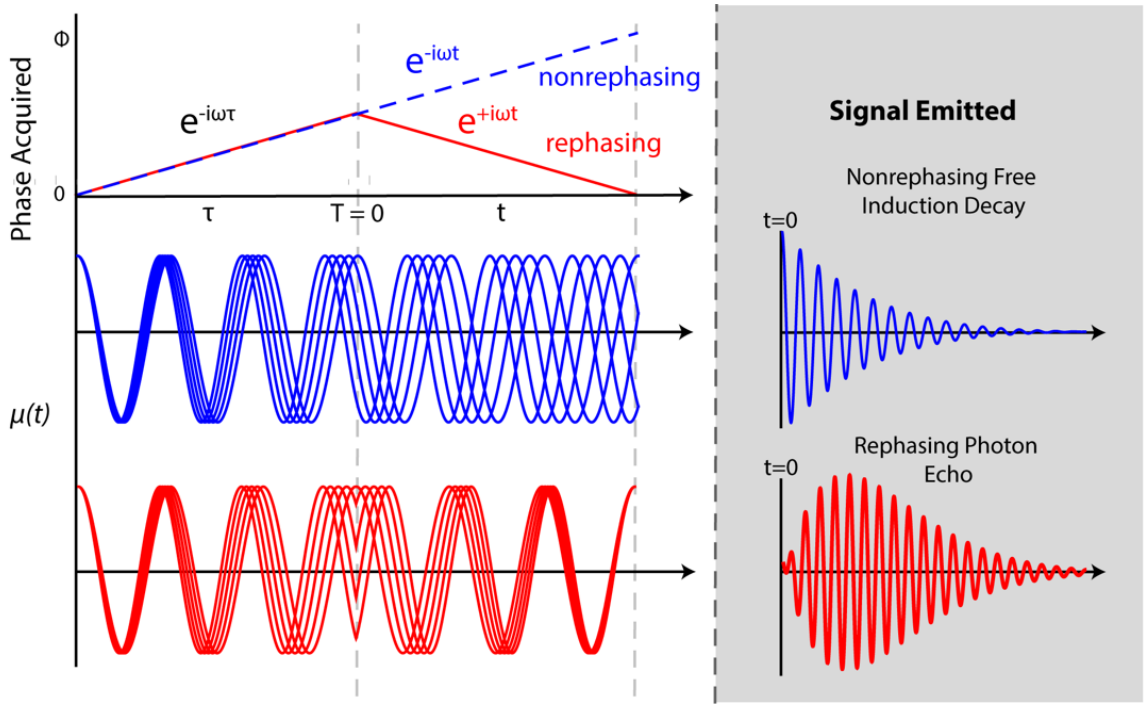

Figure 1.5: For nonrephasing signals (blue), phase is acquired in the same direction during the coherence time (τ) and the detection time (t). For rephasing signals (red), the phase acquired in the coherence time (τ) is reversed during the detection time (t). The relative phase evolution during the coherence time impacts the nature of the signal generated. Nonrephasing pathways generate a free induction decay and rephasing pathways generate a photon echo. Figure adapted from Reference [26].

to the signal, giving the spectrum artificial elongation in a specific direction. This distortion, known as a phase twist, obscures spectral information such as the evolution of spectral line shapes and dynamic peak shifts, which can inform on the underlying electronic structure. [21] The 2DES rephasing and nonrephasing signals are not generated in the same phase-matched direction; however, if the order of the first two pulses in the 2DES sequence are switched, the two signals will be emitted in the same phase-matched direction, $k_{sig} = -k_1 + k_2 + k_3$, enabling a single experimental geometry during collection. [27]

If we expand the commutators in equation 1.17, we can explicitly write down the third-order response function for the rephasing ground state bleach signal (Figure 1.4, top left):

$$R = p_g(\mu_{eg}^*)[e^{-i\omega_{ge}\tau-\Gamma_{ge}\tau}](\mu_{ge}^*)(e^{-i\omega_{gg}T-\Gamma_{gg}T})(\mu_{eg})[e^{-i\omega_{ge}t-\Gamma_{ge}t}](\mu_{ge}) \tag{1.18}$$

where p_g is the probability of initially occupying the ground states, ω_{eg} is the frequency of the energy gap between the ground and excited states ($\omega_{eg} = E_e - E_g/\hbar$), and $\Gamma_{eg} = \Gamma_{ge}$ is damping constant. Equation 1.18 can be simplified to:

$$R = p_g|\mu_{ge}|^4 e^{i\omega_{eg}(\tau-t)-\Gamma_{eg}(\tau+t)-\Gamma_g g(T)} \tag{1.19}$$

In this rephasing pathway, and all rephasing pathways, the phase acquired during the coherence time is $e^{+i\omega_{eg}\tau}$. The reversal of this phase in the during the detection time, $e^{-i\omega_{eg}t}$, generates a photon echo signal. In nonrephasing pathways, the phase evolution during the coherence time, $e^{-i\omega_{eg}\tau}$, and the phase evolution in the detection time, $e^{-i\omega_{eg}t}$, have the same sign which results in emission of a free induction decay signal (Figure 1.5).

The pathways depicted in Figure 1.4 are static pathways. That is, there are no dynamics occurring during the waiting time. There are additional pathways that meet the phase matching conditions, which represent population transfer or coherent dynamics. Examples of these types of pathways are depicted as double-sided Feynman diagrams in Figure 1.6.

A 2DES spectrum presents the signal as a function of two frequencies, the excitation and detection frequencies, and one time, T. The resultant plot is a correlation map between the excitation and detection frequencies. The excitation axis is generated by taking a Fourier transform over the coherence time and the detection axis is generated by spectrally resolving the emitted signal using a grating. A 2D correlation map is produced for every waiting time delay, T. Diagonal features in the 2DES spectrum are related, but not equal to, linear absorption features, as they arise from nonlinear signals that scale as μ^4 rather than μ^2. Off diagonal features, or cross peaks, arise at $T = 0$ as a result of coupling between excitonic

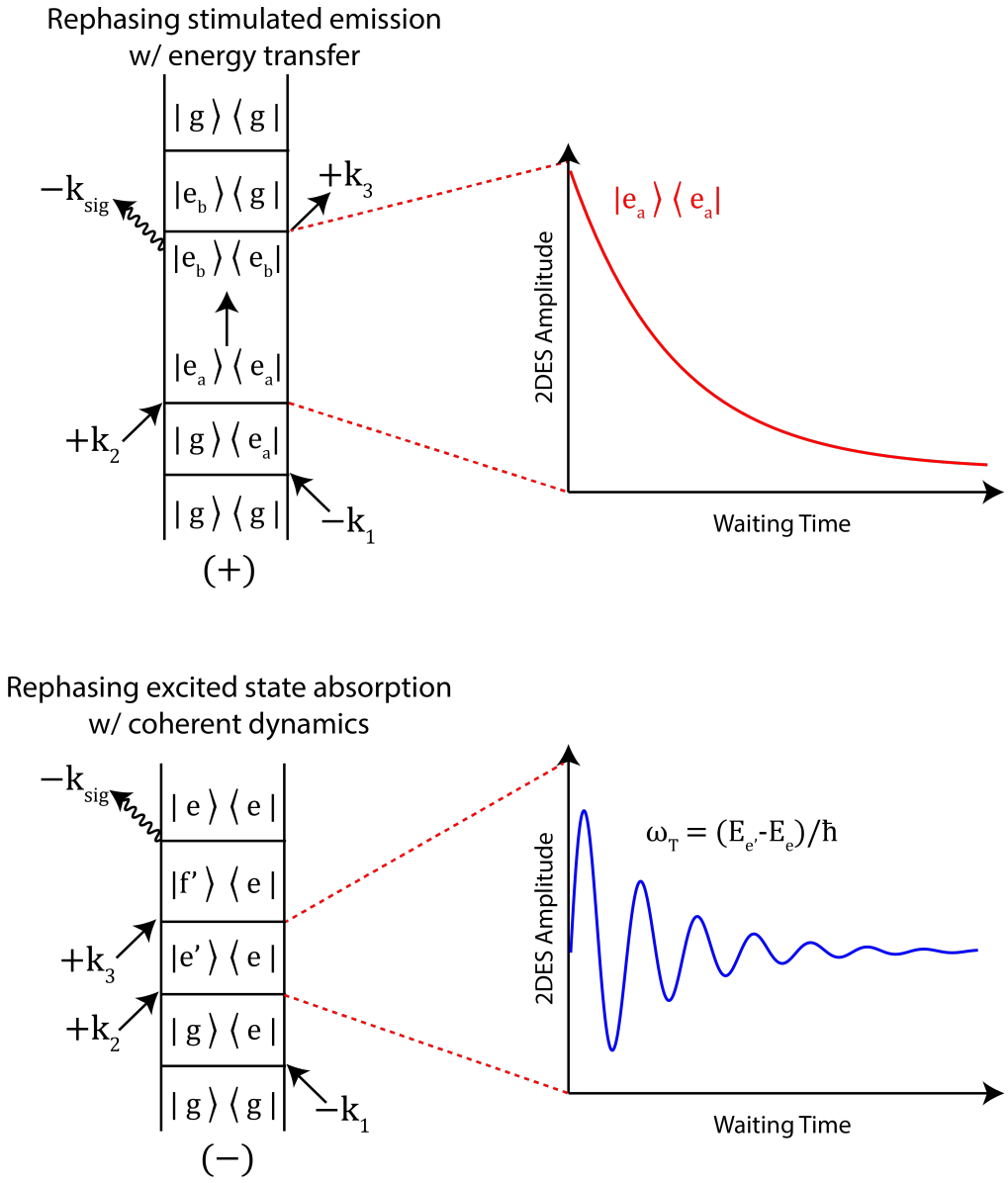

Figure 1.6: (Top) A rephasing stimulated emission pathway showing energy transfer between non-degenerate states a and b. Energy transfer, depicted by a vertical arrow, from a to b occurs during the waiting time. The corresponding waiting time dynamics show an exponential decay of the 2D signal corresponding to the excited state population of a. (Bottom) A rephasing excited state absorption pathway showing coherent dynamics between nondegenerate excited states. Waiting time oscillations occur when a superposition of two excited (or ground) states occurs during to the waiting time. The coherent dynamics dephase due to interactions with the bath. Dephasing timescale can point to the physical origin of the coherent states.

states. At later waiting times, these features report on energy transfer between nondegenerate states. As denoted in Figure 1.4, ground state bleach (GSB) and stimulated emission (SE) signals are positive in 2DES experiments due to stronger signals from emission/bleach, while excited state absorption signals (ESA) are negative due to absorption of incident fields.

The lineshapes of 2DES spectral features report on the degree of correlation between excitation and detection frequencies and the rate at which these correlations are lost. Linear spectra cannot determine the broadening mechanism of spectral lineshapes. In the inhomogeneous limit, the timescale of fluctuation is slow compared to the inverse linewidth. This leads to diagonal elongation of the 2D lineshape, a distinct distribution of chromophores has been captured, and there is a high degree of correlation (or memory) between excitation and detection frequencies. As waiting time progresses, this memory of the initial excitation is lost because the collection of states exchange, or spectrally diffuse, on these longer timescales. [21, 28] After spectral diffusion, elongation is lost and round, homogeneously broadened lineshapes result. [21]

REFERENCES

[1] Gregory S. Engel. Quantum coherence in photosynthesis. *Procedia Chemistry*, 3(1):222–231, 2011.

[2] David J. Mothersole, Philip J. Jackson, Cvetelin Vasilev, Jaimey D. Tucker, Amanda A. Brindley, Mark J. Dickman, and C. Neil Hunter. PucC and LhaA direct efficient assembly of the light-harvesting complexes in *Rhodobacter sphaeroides*. *Molecular Microbiology*, 99(2):307–327, 2016.

[3] Herbert van Amerongen, Rienk van Grondelle, and Leonas Valkunas. Photosynthetic excitons. page 604, 2000.

[4] Peter D. Dahlberg, Po-Chieh Ting, Sara C. Massey, Marco A. Allodi, Elizabeth C. Martin, C. Neil Hunter, and Gregory S. Engel. Mapping the ultrafast flow of harvested solar energy in living photosynthetic cells. *Nature Communications*, 8(1):988, 2017.

[5] Andy Freer, Steve Prince, Ken Sauer, Miroslav Papiz, Anna Hawthornthwaite Lawless, Gerry McDermott, Richard Cogdell, and Neil W. Isaacs. Pigment-pigment interactions and energy transfer in the antenna complex of the photosynthetic bacterium *Rhodopseudomonas acidophila*. *Structure*, 4(4):449–462, 1996.

[6] P. Qian, M. Z. Papiz, P. J. Jackson, A. A. Brindley, I. W. Ng, J. D. Olsen, M. J. Dickman, P. A. Bullough, and C. N. Hunter. Three-dimensional structure of the *Rhodobacter sphaeroides* RC-LH1-PufX complex: dimerization and quinone channels promoted by PufX. *Biochemistry*, 52(43):7575–85, 2013.

[7] Villy Sundström, Tõnu Pullerits, and Rienk van Grondelle. Photosynthetic light-harvesting: Reconciling dynamics and structure of purple bacterial LH2 reveals function of photosynthetic unit. *The Journal of Physical Chemistry B*, 103(13):2327–2346, 1999.

[8] M. Şener, J. Hsin, L. G. Trabuco, E. Villa, P. Qian, C. N. Hunter, and K. Schulten. Structural model and excitonic properties of the dimeric RC-LH1-PufX complex from *Rhodobacter sphaeroides*. *Chem Phys*, 357(1-3):188–197, 2009.

[9] Ana Damjanović, Thorsten Ritz, and Klaus Schulten. Excitation energy trapping by the reaction center of *Rhodobacter sphaeroides*. *International Journal of Quantum Chemistry*, 77(1):139–151, 2000.

[10] Dmitry Shevela, Lars Olof Bjorn, and Govindjee. Oxygenic photosynthesis. pages 13–63, 2013.

[11] Robert E. Blankenship. *Molecular Mechanisms of Photosynthesis*. John Wiley& Sons, Ltd, Chinchester, West Sussex, 2nd edition, 2014.

[12] L. Bar-Eyal, A. Shperberg-Avni, Y. Paltiel, N. Keren, and N. Adir. Light harvesting in cyanobacteria: The phycobilisomes. 2018.

[13] Yasufumi Umena, Keisuke Kawakami, Jian-Ren Shen, and Nobuo Kamiya. Crystal structure of oxygen-evolving Photosystem II at a resolution of 1.9 Å. *Nature*, 473(7345):55–60, 2011.

[14] Patrick Jordan, Petra Fromme, Horst Tobias Witt, Olaf Klukas, Wolfram Saenger, and Norbert Krauß. Three-dimensional structure of cyanobacterial Photosystem I at 2.5 Å resolution. *Nature*, 411(6840):909–917, 2001.

[15] G. W. Suter and A. R. Holzwarth. A kinetic model for the energy transfer in phycobilisomes. *Biophysical journal*, 52(5):673–683, 1987.

[16] J. J. van Thor, C. W. Mullineaux, H. C. P. Matthijs, and K. J. Hellingwerf. Light harvesting and state transitions in cyanobacteria. *Botanica Acta*, 111(6):430–443, 1998.

[17] Craig MacGregor-Chatwin, Melih Sener, Samuel F. H. Barnett, Andrew Hitchcock, Meghan C. Barnhart-Dailey, Karim Maghlaoui, James Barber, Jerilyn A. Timlin, Klaus Schulten, and C. Neil Hunter. Lateral segregation of Photosystem I in cyanobacterial thylakoids. *The Plant Cell*, 29(5):1119, 2017.

[18] Melih Şener, Johan Strümpfer, Jen Hsin, Danielle Chandler, Simon Scheuring, C. Neil Hunter, and Klaus Schulten. Förster energy transfer theory as reflected in the structures of photosynthetic light-harvesting systems. *Chemphyschem : a European journal of chemical physics and physical chemistry*, 12(3):518–531, 2011.

[19] A. Chenu and G. D. Scholes. Coherence in energy transfer and photosynthesis. *Annu Rev Phys Chem*, 66:69–96, 2015.

[20] Elisabetta Collini. Spectroscopic signatures of quantum-coherent energy transfer. *Chemical Society Reviews*, 42(12):4932–4947, 2013.

[21] Peter Hamm and Martin Zanni. Concepts and methods of 2D infrared spectroscopy. 2011.

[22] S. Mukamel. Principles of nonlinear optical spectroscopy. 1995.

[23] Yuan-Chung Cheng, Gregory S. Engel, and Graham R. Fleming. Elucidation of population and coherence dynamics using cross-peaks in two-dimensional electronic spectroscopy. *Chemical Physics*, 341(1):285–295, 2007.

[24] Elad Harel, Andrew F. Fidler, and Gregory S. Engel. Single-shot gradient-assisted photon echo electronic spectroscopy. *The Journal of Physical Chemistry A*, 115(16):3787–3796, 2011.

[25] T. Brixner, T. Mancal, I. V. Stiopkin, and G. R. Fleming. Phase-stabilized two-dimensional electronic spectroscopy. *J Chem Phys*, 121(9):4221–36, 2004.

[26] Andrei Tokmakoff. Nonlinear spectroscopy. http://tdqms.uchicago.edu/page/nonlinear-and-two-dimensional-spectroscopy-notes, 2011.

[27] Minhaeng Cho. Coherent two-dimensional optical spectroscopy. *Chemical Reviews*, 108(4):1331–1418, 2008.

[28] Randy D. Mehlenbacher, Jialiang Wang, Nicholas M. Kearns, Matthew J. Shea, Jessica T. Flach, Thomas J. McDonough, Meng-Yin Wu, Michael S. Arnold, and Martin T. Zanni. Ultrafast exciton hopping observed in bare semiconducting carbon nanotube thin films with two-dimensional white-light spectroscopy. *The Journal of Physical Chemistry Letters*, 7(11):2024–2031, 2016.

CHAPTER 2

EXPERIMENTAL METHODS AND INSTRUMENTATION

2.1 Spectroscopic Methods

We use a Ti:Sapph 80 MHz oscillator (Coherent Micra) (FWHM = 80 nm, $\lambda_{central}$ = 802 nm, ∼350 mW output power) to seed a regenerative amplifier (Coherent Legend Elite). The regenerative amplifier is pumped by a Coherent Evolution ($\lambda_{central}$ = 532 nm, ∼20 W output power). The oscillator output is down-selected in the regenerative amplifier using chirped pulse amplification. During chirped pulse amplification, the output of the oscillator is stretched temporally, amplified, and re-compressed, resulting in 5 kHz output with output power of 2.0 - 2.6 W. The regenerative amplifier output spectrum is centered at 800 nm with 37 nm of bandwidth. The output pulses from the regenerative amplifier are the starting point for the pulses used in our ultrafast experiments. The output of the regenerative amplifier is spectrally broadened via filamentation (described in more detail in section 2.2.2. The spectrally broadband pulses are then sent to a spatial light modulator (SLM) based Multiphoton Intrapulse Phase Scan (MIIPS) compressor (Biophotonics, Inc.). After the MIIPS, the beam can be diverted to the setup for two-dimensional electronic spectroscopy (2DES) experiments or the setup for transient absorption (pump-probe) spectroscopy experiments.

2.1.1 GRadient-Assisted Photon Echo Spectroscopy (GRAPES)

All of the 2DES experiments in this thesis were collected using GRadient Assisted Photon Echo Spectroscopy (GRAPES). GRAPES differs from conventional 2DES spectrometers in that it focuses the ultrafast pulses to lines, rather than points, at the sample. The wavevector of pulse 1 is then geometrically tilted with respect to pulses 2 and 3. The resultant angle between pulses 1 and 2 is ∼1.2 degrees. The spatial separation of pulses 1 and 2 along the vertical height of beams encodes the coherence time delay [1]. This geometry enables the

collection of an entire 2D spectrum at a single waiting time to be collected on each laser shot. Though GRAPES can function as a single-shot spectrometer, we average many of these single-shot spectra during our acquisition to increase the single-to-noise of the measurement.

In order to create the four pulses needed for a GRAPES experiments (three pulses to generate the third-order signal and another to use as a reference or local oscillator, L.O.), we first divide the output of the MIIPS into two equal pulses using a 50:50 beam splitter. The pulse that is transmitted through the beam splitter will become pulse 3 and the L.O. and the pulse that is reflected off the beam splitter will become pulses 1 and 2. The 1/2 beam is sent to a retroreflector on a linear delay stage. Movement of this stage lengthens or shortens the 1/2 beam path relative to the path of pulse 3, therefore controlling the waiting time (temporal separation between pulses 2 and 3). In order to maintain the same temporal profile of all beams, a 1 mm thick piece of compensating glass (UV fused silica) is placed in the 1/2 beam path after the delay line. Beam 1/2 and beam 3/L.O. are then sent to a pair of 60:40 beam splitters with silver mirrors behind them. The portions of the pulses reflected off the beam splitters become pulses 1 and the L.O.. The transmitted fractions of the beams (60 percent of the incident pulse) reflect off the silver mirrors placed behind the beam splitters and then pass back through the beam splitters creating pulses 2 and 3. Higher order reflections off the silver mirror-beam splitter pairs are blocked using a spatial filter. For more details of the design of these beam splitter silver mirror pairs and the wedged beam splitters they replaced see section 2.2.4. At this point the L.O. is attenuated on an as needed basis using a neutral density filter wheel to maximize the heterodyned signal while avoiding saturating the detector in the spectrometer.

All four beams reflect of the *GRAPE optic* which creates the distorted BoxCARS geometry used in the experiment and sets the phase matching condition. Figure 2.1 shows a photograph of the GRAPE optic. Beams 2 and 3 travel parallel to each other while beam 1 and the L.O. are vertically separated from beams 2 and 3 at the GRAPE optic. Beam

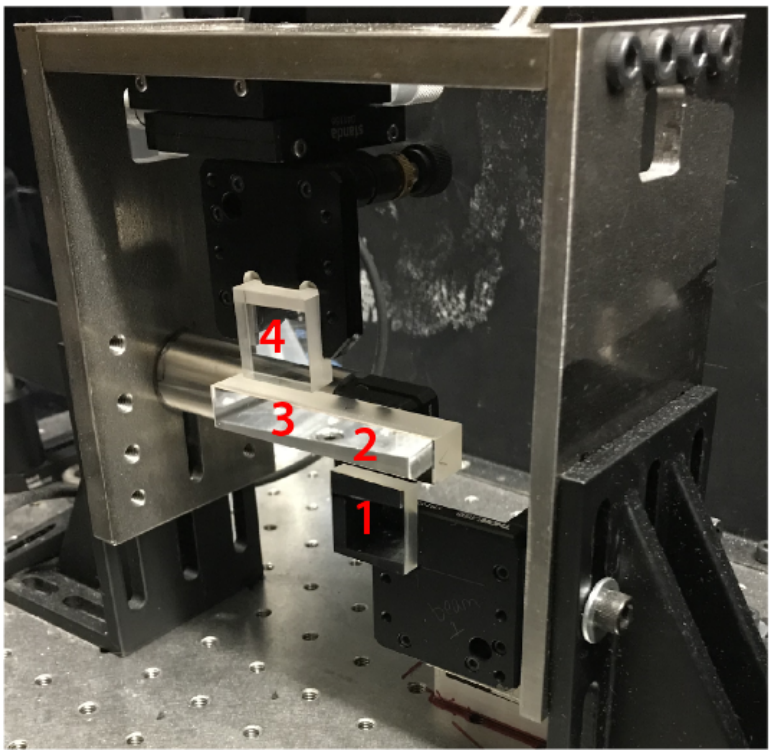

Figure 2.1: This photograph of the GRAPE optic creates the distorted BoxCARS geometry used in GRAPES. Beams 2 and 3 travel parallel to each other and reflect off the center rectangular optic. Beam 1 reflects off the bottom silver mirror which steers the beam upwards such that it spatially overlaps with beams 2 and 3 at the sample. Beam 4 is steered downward by the upper optic which is a piece of UV fused silica. The angle of this piece of glass steers the reflected portion of beam 4 such that is overlaps with the other 3 beams at the sample.

1 is steered upward by the GRAPE optic and the L.O. is steered downward such that all four beams spatially overlap at the sample. The L.O. reflects off of a piece of UV fused silica on the GRAPE optic while the other three beams reflect off of silver mirrors. The Fresnel reflection off the piece of UV fused silica serves to attenuate the L.O. both so that it does not interfere with the desired 2DES pulse sequence and to ensure an intensity that is manageable by the detector in the spectrometer. After the GRAPE optic, all four beams travel to a cylindrical mirror (Lattice Optics, f= 250 mm) which focuses the beams in the horizontal dimension while collimating them in the vertical dimension. This results in beams that are 1 cm tall by 100 μm wide at the sample. We align the beams to overlap spatially at their focal point and set the crossing point between beams 1 and 2 to be near the middle of the beam height.

The sample flow cell is mounted on a micrometer stage and positioned at the crossing point of the beams. The flow cell tubing is attached to a peristaltic pump which is set to its maximum speed during the experiment. Flowing helps diminish scatter and prevents photobleaching. The sample cell is mounted at an angle that is not aligned with the direction of flow. The phase matching condition of the distorted BoxCARS geometry used in GRAPES prescribes that the generated third-order signal will co-propagate with the L.O. As such, the L.O. is aligned through a spatial filter after the sample set to block beams 1, 2 and 3 and scattered light before being focused through the slit of the spectrometer (Andor Shamrock 303i) coupled to a sCMOS camera. The data presented in this thesis was either collected using a Phantom Miro M310 CMOS array camera or an Andor Neo 5.5 sCMOS 2D array camera. The reasoning behind switching from the Miro to the Neo is described in detail in section 2.2.7. The detection wavelength is resolved by the grating in the spectrometer and is mapped onto the horizontal axis of the detector. The coherence time is mapped onto the vertical axis of the detector.

Data acquisition speed is set by down-selecting the TTL signal from the regenerative

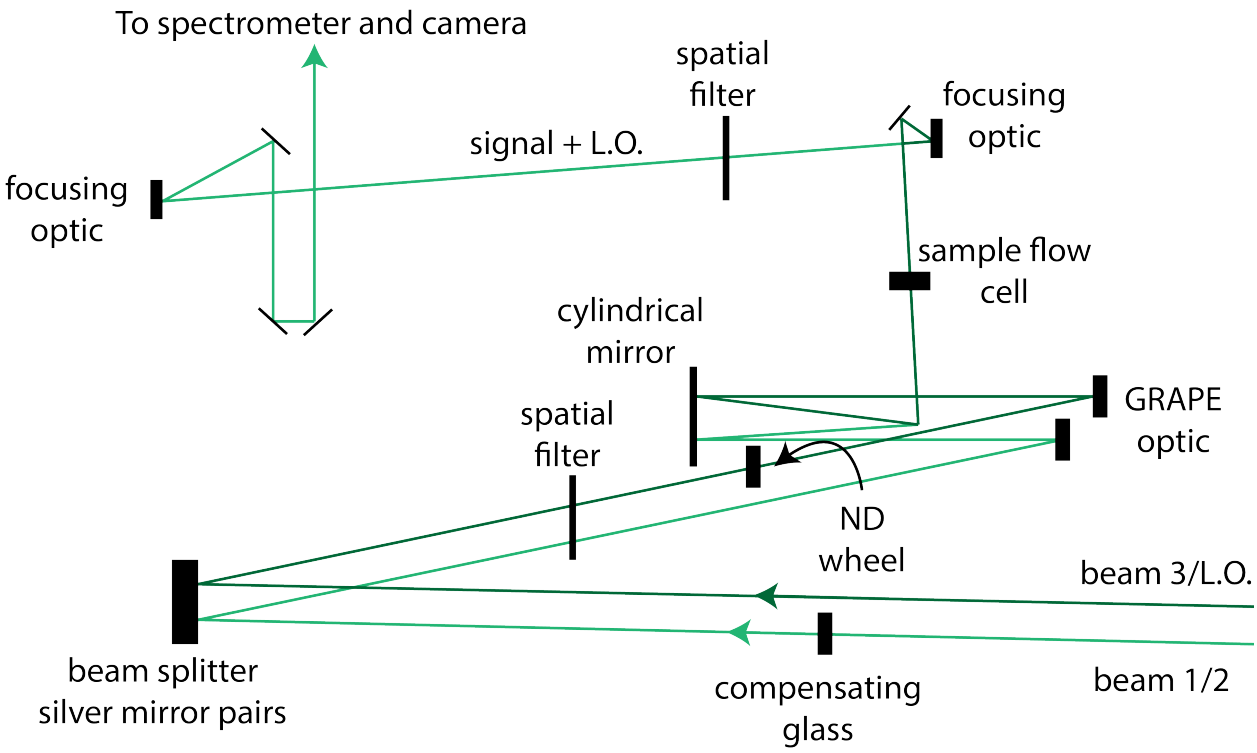

Figure 2.2: The beam path for the GRAPE spectrometer. For simplicity, only the beam 1 (light green) and L.O. (dark green) paths are represented.

amplifier using a divide-by circuit. This down-selected signal is synced to an optical chopper that blocks beam 1/2 before it is split. The chopper is run at half the speed of the camera such that every other collected frame contains the the signal. The other frames contain only heterodyned scatter from beam 3 and the L.O.. The divide-by circuit can be set to any integer and the chosen collection speed depends on the limits of the optical chopper and the camera. The output of the regenerative amplifier is 5 kHz, if the divide-by circuit is set to divide this TTL signal by 625, the camera will run at 8 Hz and the chopper will run at 4 Hz. This acquisition speed corresponds to averaging 625 laser shots of heterodyned signal for every signal-containing frame collected.

2.1.2 Pump-Probe Spectroscopy

Ultrafast pump-probe, or transient absorption, spectroscopy is another third-order nonlinear spectroscopy. Pump-probe differs from 2DES in that the first two light-matter interactions come from a single pump pulse and therefore τ, the coherence time, is always equal to zero and the excitation energy cannot be spectral resolved. After the MIIPS, the pulse is sent to a separate, movable breadboard that contains the pump-probe spectrometer. The pulse is split using a 90:10 wedged beam splitter. The weaker reflected portion becomes the probe and the stronger transmitted portion is the pump. The pump is sent to a motorized delay stage that controls the relative timing between the pump and probe pulses. After the beam splitter, the probe passes through compensating glass so that pulse compression is maintained between the pump and the probe. The pump beam is sent through an optical chopper running at 2.5 kHz. The pump beam has the repetition rate of the output from the regenerative amplifier, 5 kHz. Both beams are focused at the sample position, and the pump is blocked after the sample using a partially closed iris. The probe and the signal co-propagate and are focused onto the slit of the spectrometer (Andor Shamrock 303i) coupled to a line scan CCD camera (Teledyne Dalsa). The probe and the pump-probe signal are spectrally resolved on

the camera. The probe is then subtracted from the heterodyned pump-probe signal. Strong interference between scattered pump and probe beams and weaker interference between the scattered pump beam and the signal are contained to time delays near T = 0 because all wavelengths in the spectrum constructively interfere at this time delay. These scatter signals can be removed through windowing (apodization) in the waiting frequency domain. If the waiting time step size is not fine enough relative to the optical period to enable windowing, the detected signal plus scatter near T = 0 cannot be trusted and must be omitted. This is admissible when long time dynamics are of interest. Significant scatter from the pump is strongly present at negative waiting times and can be removed by averaging the collected intensity at negative waiting times and subtracting this from the collected signal plus scatter at positive waiting times. For this subtraction to be valid, enough negative time points should be collected to produce a representative average.

2.2 Technical Advances to GRAPES Instrumentation

2.2.1 Collecting Rephasing and Nonrephasing Third-Order Signals in a Single Phase-Matched Geometry

For details of how GRAPES has been adapted to collect both rephasing and nonrephasing signals without instrumental realignment see Section 3.3. [2]

2.2.2 Improving White Light Generation

A large technical advance in GRAPES was improving white light generation, or spectral broadening of the output pulse of the regenerative amplifier. Previously, the GRAPES instrumentation could only be used for samples that absorbed from 775 nm to 880 nm [2–5] because there was not much broadening of the fundamental regenerative amplifier output (800 nm). First, I will briefly discuss the technical background for white light filamentation

and then I will show how I have improved the spectrum accessible with GRAPES.

Supercontinuum generation from ultrafast laser pulses is enabled by nonlinearity in the index of refraction of the material through which the pulses pass. In our supercontinuum generation setup, we use argon gas held above atmospheric pressure and lab air as the nonlinear media. The refractive index of a medium with Kerr nonlinearity is given by

$$n = n_0 + n_2 I(t) \tag{2.1}$$

where n_0 is the nonpertubed index of refraction and n_2 is the nonlinear refractive index which is dependent on the third-order linear susceptibility of the medium, $\chi^{(3)}$, and $I(t)$ is the intensity of the laser pulses [6, 7]. The n_2 term in equation 2.1 results in a significant self-phase modulation of the laser field. The nonlinear phase acquired as a result of this self-phase modulation over a distance L is

$$\Phi(t) = \frac{\omega}{c} n_2 I(t) L \tag{2.2}$$

where ω is the frequency of the laser light. The self-phase modulation is dependent on the intensity of the laser pulse as it passes through the nonlinear medium and the resultant frequency shift due to the self-phase modulation is

$$\Delta\omega(t) = \frac{\omega}{c} n_2 L \frac{\partial I}{\partial t} \tag{2.3}$$

The maximum frequency shift attainable is limited by the peak intensity of the pulse and the pulse duration:

$$\Delta\omega = \frac{\omega}{c} n_2 L \frac{I_0}{\tau} \tag{2.4}$$

In the improvement of our supercontinuum generation setup for use with GRAPES, we focused on minimizing pulse duration and using a medium with a high third-order nonlinear

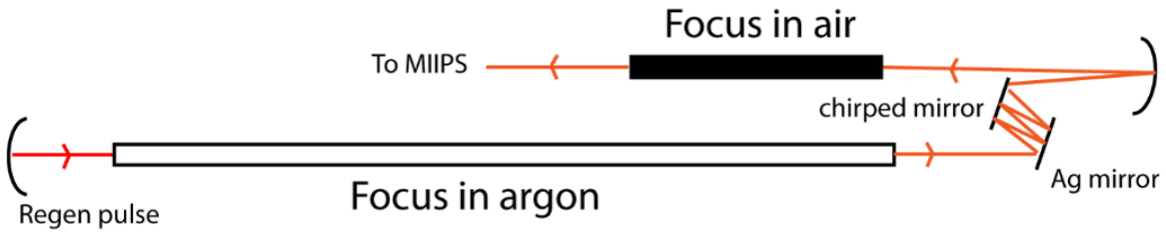

Figure 2.3: The compressed output pulse from the regenerative amplifier is focused in a tube of argon held at 15 psi. Self-phase modulation occurs in the argon resulting in a spectral frequency shift. The pulse is re-compressed using a negative GVD mirror (chirped mirror) before being focused in an open ended pipe (filled with lab air). The FWHM of the resultant spectrum spanned from 785 nm to 845 nm.

susceptibility as n_2 is proportional to this material property.

The original GRAPES supercontinuum generation setup is drawn in Figure 2.3. In this design, the output from the regenerative amplifier was focused into a pipe filled with Argon gas held at 15 psi. Self-phase modulation occurs at the focus within the pipe because the peak laser intensity is extremely high and the output of the regenerative amplifier is compressed to ∼37 fs. After exiting the pipe, the pulse is recompressed temporally using three bounces off a single negative group velocity delay (GVD). The pulse is then focused again, this time in an open tube of air.

The spectrum after the focus in argon and the focus in air is shown in Figure 2.4. The majority of spectral intensity is around 800 nm, the fundamental laser wavelength. The spectrum also exhibits modulations on the blue side. We attribute the modulation to the coating on the negative GVD mirror (Layertec, -65 fs^2 700-950 nm) which is not meant for wavelengths blue of 700 nm. This spectrum was used for the experiments in *Rba. sphaeroides* cells described in Chapter 3. [2]

In order to improve the accessed frequency shift according to equation 2.3, we replaced the focus in air with a second focus in argon gas at 15 psi. Argon has a higher third-order nonlinear susceptibility than air and therefore its Kerr-nonlinearity-induced intensity-

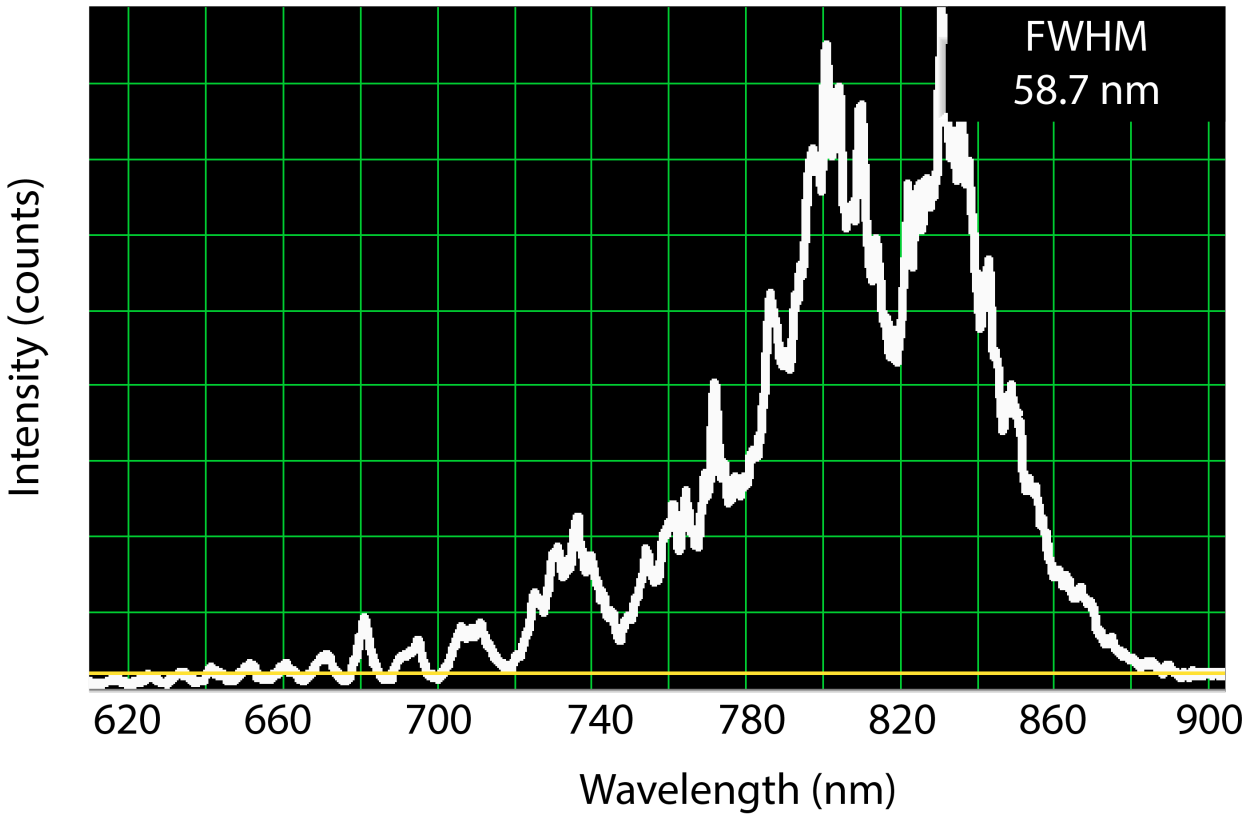

Figure 2.4: The laser spectrum after supercontinuum generation using one focus in argon at 15 psi and one focus in air. This laser spectrum limited experiments to samples that absorb near 800 nm.

dependent additive to the refractive index is greater. [6] In addition, we used a pair of negative group delay dispersion (GDD) mirrors (Layertec, -40fs^2 510-920 nm) to more adequately compensate for the temporal broadening incurred on the first pass through the argon tube. Adequate compression enables a larger frequency shift due to the self-phase modulation on the second focus in the argon tube. Additionally, we limited the spectral broadening on the first pass to ensure successful temporal compression of the pulse prior to the second pass. Figure 2.5 shows the spectrum after the first pass through the argon tube. The output spectrum from the regenerative amplifier is centered at 800 nm with a FWHM of 28 nm. The first focus through argon produces slight broadening of the original spectrum. After four bounces on each negative GDD mirror in the pair (for a total of eight bounces), the pulse is well-compressed and the second focus in argon results in significant spectral broadening (Figure 2.6). Figure 2.7 depicts the revised optical setup for broader-band supercontinuum generation.

The double pass in argon not only shows more broadening about the fundamental (800 nm), it also has significantly more intensity on the blue tail of the spectrum. With the large amount of light that remains near the fundamental it is difficult to observe this blue tail without saturating the spectrometer with the light near 800 nm. In order to dump the fundamental, we use a shortpass filter with a cutoff of 750 nm (Thorlabs). Light red of 750 nm is reflected by the filter and the bluer wavelengths are transmitted through it. It is important to note that the wavelengths needed for ultrafast experiments should not be reflected off dielectric filters as the coatings prohibit proper pulse compression. In the re-design of this setup, we ensured that all filters were used to reflect unwanted wavelengths. In order to compensate for dispersion incurred on the second focus through the argon tube, we used six bounces off another pair (three on each mirror in the pair) of negative GDD mirrors (Layertec, -40fs^2 510-920 nm). Using these negative GDD mirrors before compressing the pulse with the MIIPS, decreases the phase shift for which the SLM needs to correct. We

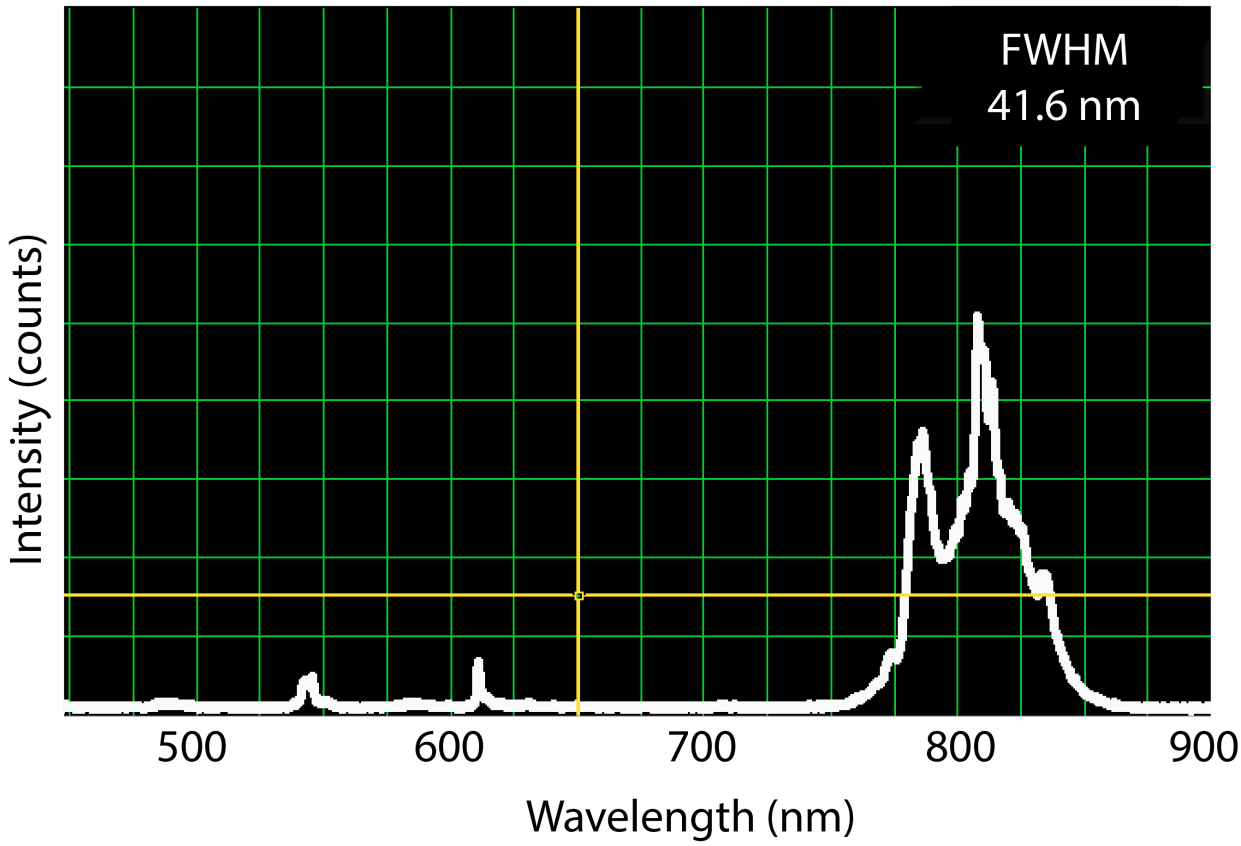

Figure 2.5: The laser spectrum after the first pass in argon gas in the newly designed broadband supercontinuum setup. Minimizing the spectral broadening on the first pass limits the temporal dispersion and enables us to correct for it using several bounces off a pair of negative GDD mirrors before re-focusing into the Argon tube for the second pass.

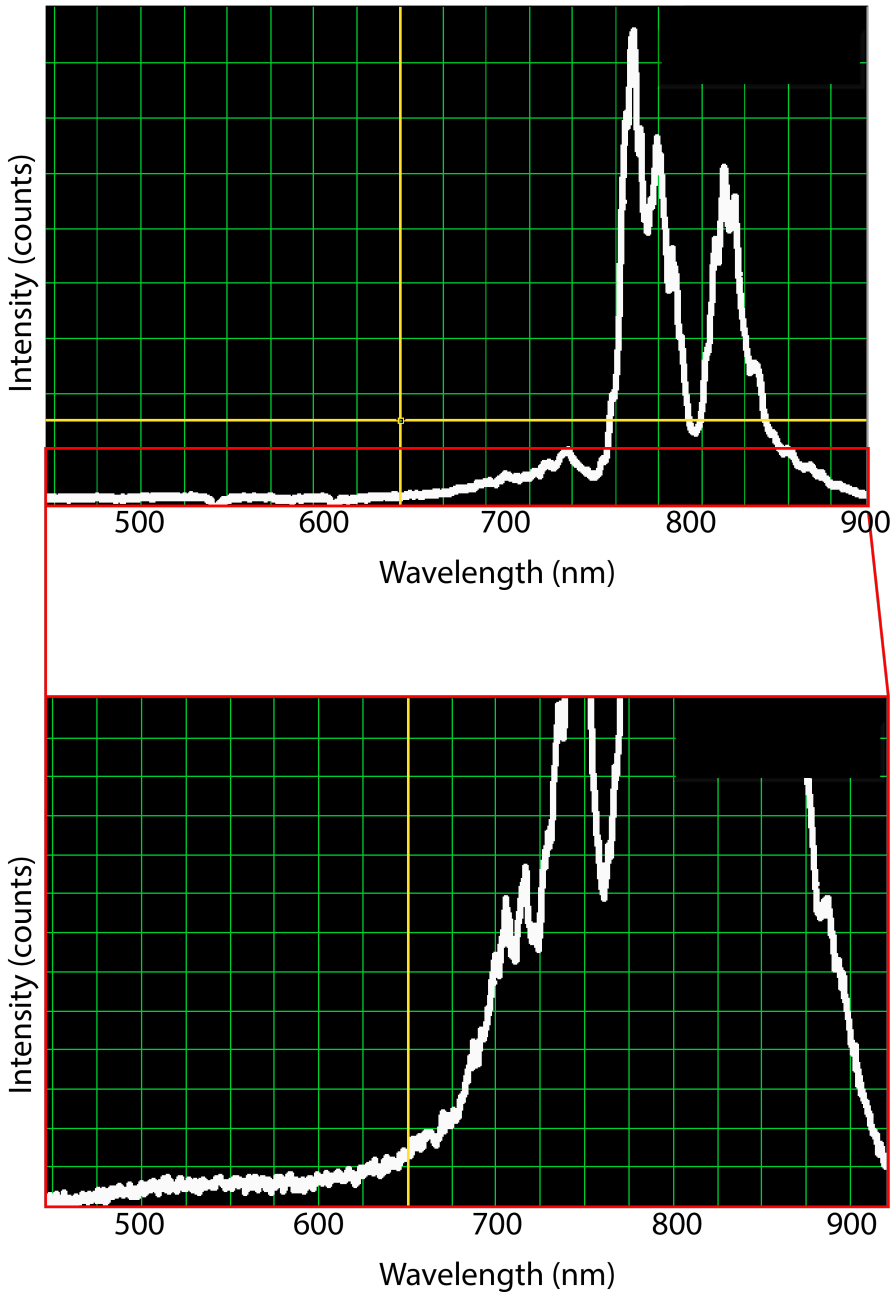

Figure 2.6: The laser spectrum after the second pass in argon gas. An adequately compressed pulse before the second pass allows a large frequency shift and broadening of the fundamental laser light. While most of the intensity of the broadened pulse still remains near 800 nm, there is a significant blue tail to the spectrum which we can use to perform GRAPES experiments on samples that absorb between 600 and 720 nm.

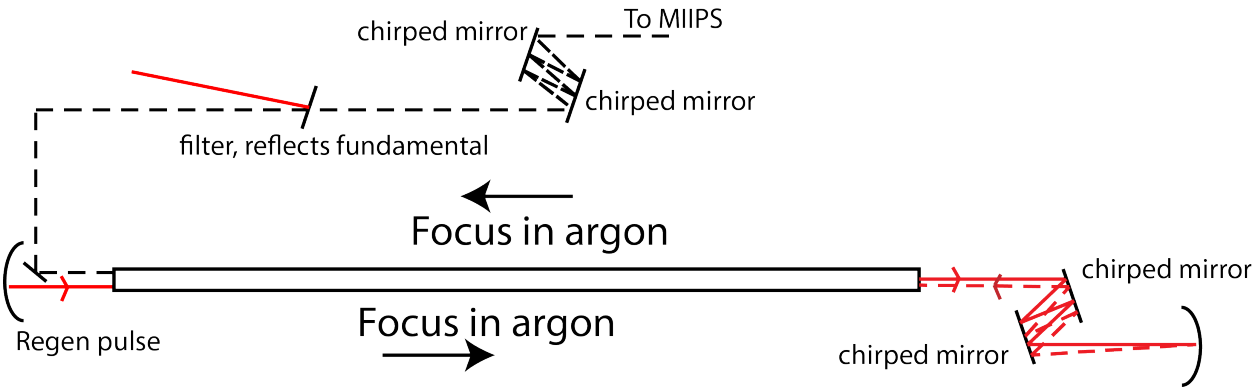

Figure 2.7: The compressed output pulse from the regenerative amplifier is focused in a tube of argon held at 15 psi. Self-phase modulation occurs in the argon resulting in a spectral frequency shift. The pulse is re-compressed using a 8 bounces off a pair of negative GDD mirror (chirped mirrors) before being focused back through the same argon pipe. The FWHM of the resultant spectrum spanned from 725 nm to 875 nm with a long tail on the blue side of the spectrum.

align the grating within the MIIPS (Newport, 900 grooves/mm, blazed for 550 nm) to cut off more of the red side of the spectrum, based on the goals of the experiment. Figure 2.8 shows the laser spectrum after the MIIPS. This is the spectrum used for experiments on samples that absorb between 600 nm and 720 nm.

2.2.3 Polarization in the GRAPES Optical Setup

In order to maximize the efficiency of the grating in the MIIPS and the grating in the spectrometer for detecting the ultimate GRAPES signal, the laser pulses dispersing off of these grating should have a polarization that is perpendicular to the grooves of the grating. This corresponds to an electric field vector parallel to the plane of incidence of the grating and we refer to this polarization as p-polarization. This polarization will always have higher efficiency off the grating than the perpendicular s-polarization. The output from the regenerative amplifier is p-polarized. In previous iterations of GRAPES, the polarization of the regenerative amplifier output was flipped using an off-axis periscope before the beam was aligned into the MIIPS. We changed this periscope to be on-axis in order to maintain

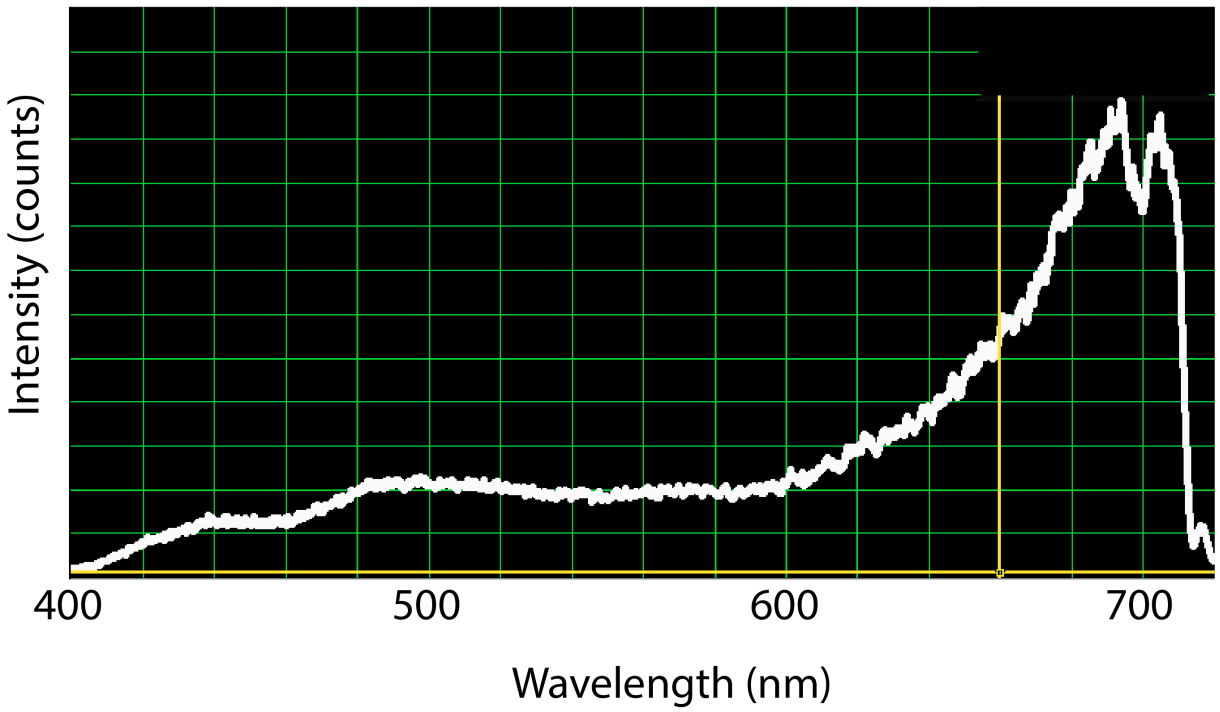

Figure 2.8: The broadband spectrum of the laser light used in GRAPES experiments with the re-designed supercontinuum generation setup. Wavelengths red of 750 nm have been reflected by a shortpass filter and light red of 720 nm has been cut off using the alignment of the grating in the MIIPS.

p-polarization and maximize the efficiency of the grating in the MIIPS, which disperses the beam onto the SLM. As a result of our improved supercontinuum generation setup (see Section 2.2.2), a new beam splitter was needed to split the output from the MIIPS into beams 1/2 and 3/L.O. that had broadband compatibility. The beam splitter implemented (Layertec) only acts as a true 50:50 beam splitter when the incident beam is s-polarized. As such, after the MIIPS we used an off-axis periscope to rotate the polarization of the beam. Before dividing beam 1/2 and 3/L.O. into the four beams used in the GRAPES pulse sequence, we used another off-axis periscope to rotate the polarization back to p-polarized. This maximizes the detected signal by ensuring it has the polarization that gives the highest efficiency for the grating in the spectrometer.

2.2.4 Adapting GRAPES for Broadband Visible Light

When GRAPES was used for applications in the near-IR (775 nm to 880 nm), wedged beam splitters were used in place of the silver mirror-beam splitter pairs discussed in Section 2.1.1. This pair of wedged optics split beam 1/2 and beam 3/L.O. into the four beams used in the GRAPES pulse sequence. These wedged beam splitters (30 arc minimum) were coated to be 100 percent reflective for wavelengths from 730 nm to 880 nm (TLM2-800 Coating, CVI Laser Optics) on one side and 40 percent reflective on the other (PR1 for 800 nm, CVI Laser Optics). As shown in Figure 2.9, beams 1 and 3 are reflections off the partially reflective front surface and beam 2 and the L.O. are reflections off the fully reflective back surface. Therefore, beam 2 and the L.O. traveled a round trip through the thickness of the wedge while beams 1 and 3 did not. The resulting disparity in temporal pulse compression had to be overcome using compensating glass. The alignment onto each of the wedges was set such that beams 2 and 3 were parallel to each other. If the two wedges were cut at the exact same angle by the manufacturer, this alignment would correspond to a perfectly distorted BoxCARS geometry. That is, the vertical separation between beams 1 and 2 and

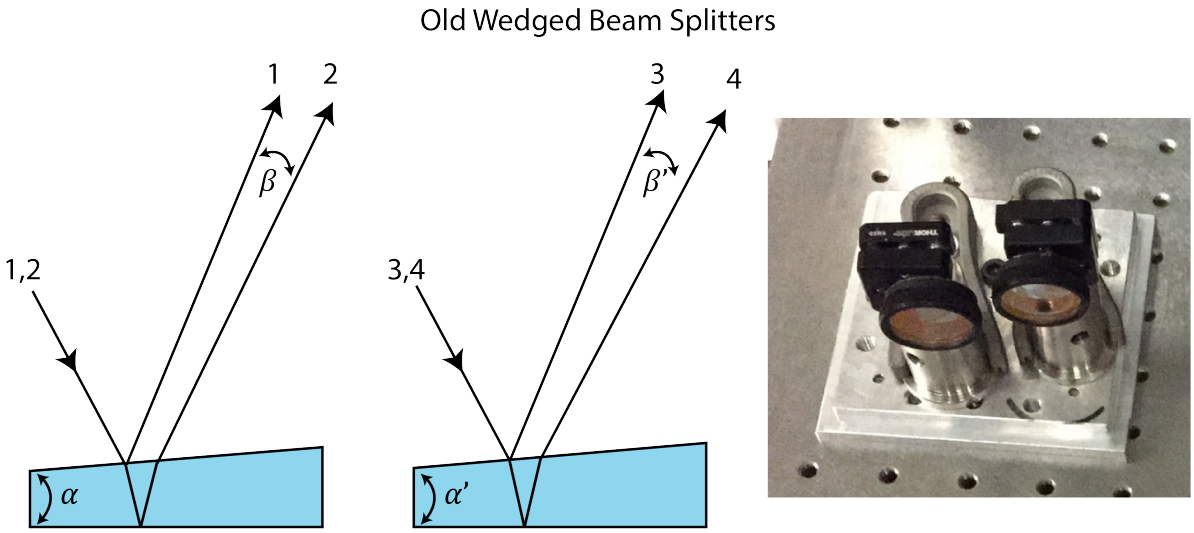

Figure 2.9: A pair of wedged beam splitters were used to to split beam 1/2 and beam 3/L.O. into four distinct beams. The alignment onto the wedge pair was set such that beams 2 and 3 would be parallel to each other as they were focused at the sample position. The front surface of the wedge is 40 percent reflective and the back surface is 100 percent reflective for 730 nm to 880 nm light.

the vertical separation between beam 3 and the L.O. were the same (Figure 2.10). But the wedges were not cut at the same angle during manufacturing. Since beams 1 and 2 share an optic and beam 3 and the L.O. share an optic, the wedged beam splitters did not allow for independent steering of all four beams. It was impossible to achieve a perfect distorted BoxCARS geometry using the wedged beam splitters.

In order to adapt GRAPES for samples that absorb in the visible range, the pair of wedged beam splitters needed to be exchanged for something compatible with wavelengths blue of 730 nm. While designing the updated beam splitter setup, we also strived for independent control over all four beams, such that we could align to a perfectly distorted BoxCARS geometry. We used beam splitter-silver mirror pairs to split beam 1/2 and beam 3/L.O. into four independently controllable beams. Photographs of the new beam splitter-silver mirror pairs and the old wedged beam splitter setup are provided in Figures 2.11 and Figure

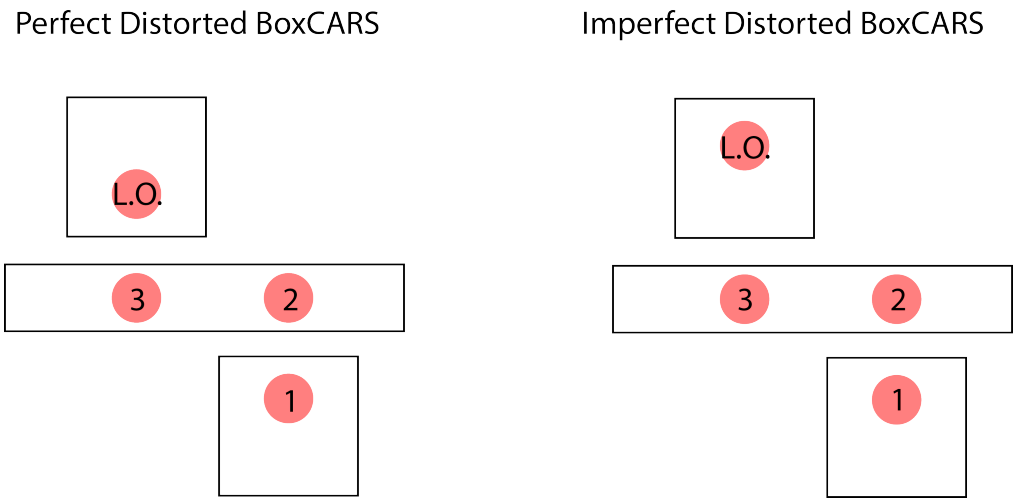

Figure 2.10: (Left) A cartoon of the relative beam positions at the GRAPE optic for a perfect distorted BoxCARS geometry. The vertical spacing between beams 1 and 2 and beam 3 and the L.O. are the same. (Right) A cartoon of the relative beam positions at the GRAPE optic for an imperfect distorted BoxCARS geometry. The vertical separation between beams 1 and 2 is smaller than the vertical separation between beam 3 and the L.O..

2.9, respectively. Beam 1 and the L.O. are reflections off of broadband 40:60 beam splitters (Chroma, 400-900 nm) which have been oriented in their mounts such that the partially reflective surface is the back surface. Silver mirrors are placed immediately behind the beam splitters. The light transmitted through the beam splitter is then reflected off the silver mirror back through the beam splitter (beams 2 and 3) resulting in four beams of roughly equal intensity. Additionally, all four beams have made one round trip through the 1 mm beam splitter making this design self-compensating. A schematic of the beam splitter-silver mirror pairs is shown in Figure 2.11. This setup can be used for experiments that span the entire visible and NIR ranges (400 nm to 900 nm).

2.2.5 Using Near-Rotating Frame Detection to Eliminate Scatter

In our design of the new beam splitter-silver mirror pairs described in Section 2.2.4, the ability to independently control the alignment of each of the four beams was extremely important. By using four separate optics for beams 1, 2, 3 and the L.O., we would be able to achieve

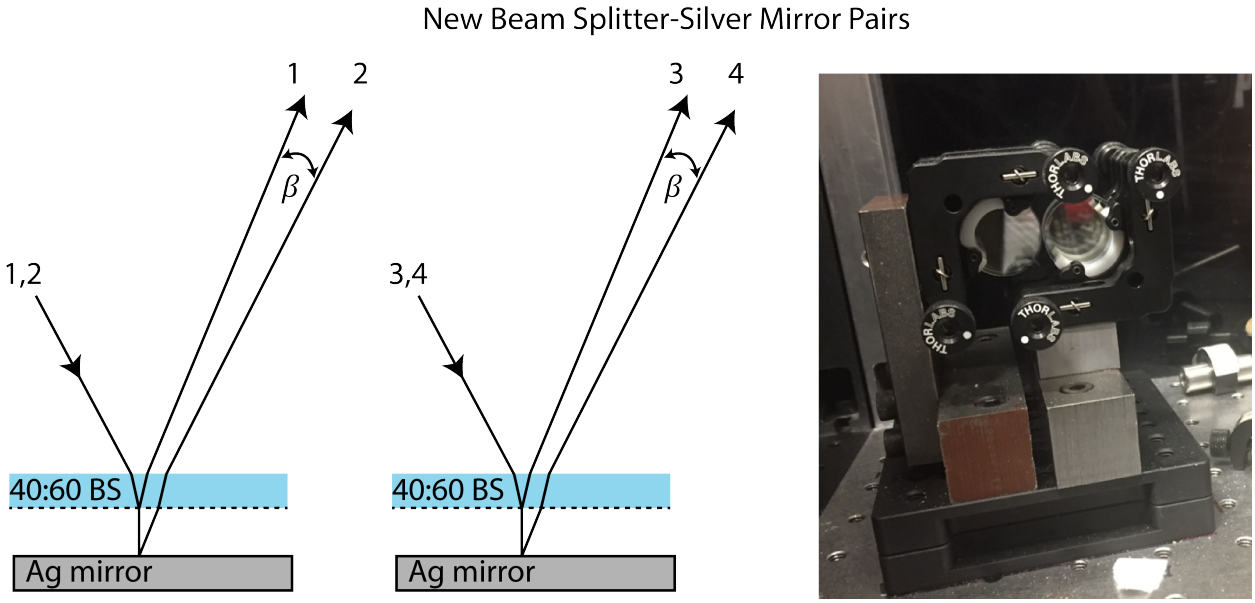

Figure 2.11: In the updated GRAPES setup for broadband (visible and NIR) experiments, beam splitter-silver mirror pairs are used to split beam 1/2 and beam 3/L.O. into four distinct beams. Because four separate optics are used to make each of the four beams needed for the experiment, each beam can be steered independently. The silver mirrors are used to set beams 2 and 3 parallel to each other. The beam splitters are adjusted to set the relative positions of beam 1 and the L.O.. This setup can be aligned to make a perfect distorted BoxCARS geometry or an imperfect distorted BoxCARS geometry.

a perfect distorted BoxCARS geometry by steering beam 1 and the L.O. such that their vertical displacements from beam 2 and 3, respectively, were the same. The perfect distorted BoxCARS geometry enables detection of the GRAPES signal in the rotating frame. [8] A signal is detected in the rotating frame when the relative phase between the pulses in the experiment change for every coherence time delay. [9] Rotating frame detection is intrinsic to nuclear magnetic resonance (NMR) spectroscopy, as the radio frequency pulses used in these experiments are given an arbitrary phase by the spectrometer. [10] In GRAPES, the phase evolved between the signal and beams 1 and 2 is not constant across the spatial height of the signal. Due to this non-uniformity in the phase, we do not detect the absolute frequency of the signal in ω_τ ($\omega_{excitation}$). Instead, we detect the envelope of the emitted signal with its fundamental frequency shifted to zero in the ω_τ domain. [11] Figure 2.12 shows that the experimental GRAPES signal of the laser dye IR144 shows up very close to zero frequency in the ω_τ domain.

As we started to use the broadband capabilities of GRAPES to measure living cyanobacteria, a highly scattering sample, the signal was partially obscured by prominent scatter that showed up at zero frequency in the rotating frame. This scatter will show up exactly on the diagonal in the final 2D spectrum if the signal is detected at precisely zero frequency in the rotating frame. If the signal is detected slightly displaced from zero frequency in the rotating frame, the scatter will show up offset from, but parallel to, the diagonal in the final 2D spectrum (Figure 2.13). [11]

In order to push this diagonal scatter away from the detected signal, the beam splitter-silver mirror pairs are used to make the vertical displacement between beam 3 and the L.O. greater than the vertical displacement between beams 1 and 2. This alignment (imperfect distorted BoxCARS in Figure 2.10) creates a gradient between the L.O. and the signal along their vertical dimension (τ). The vertical interferogram between the signal and the L.O. pushes the signal from zero frequency in the rotating frame (Figure 2.14). We have

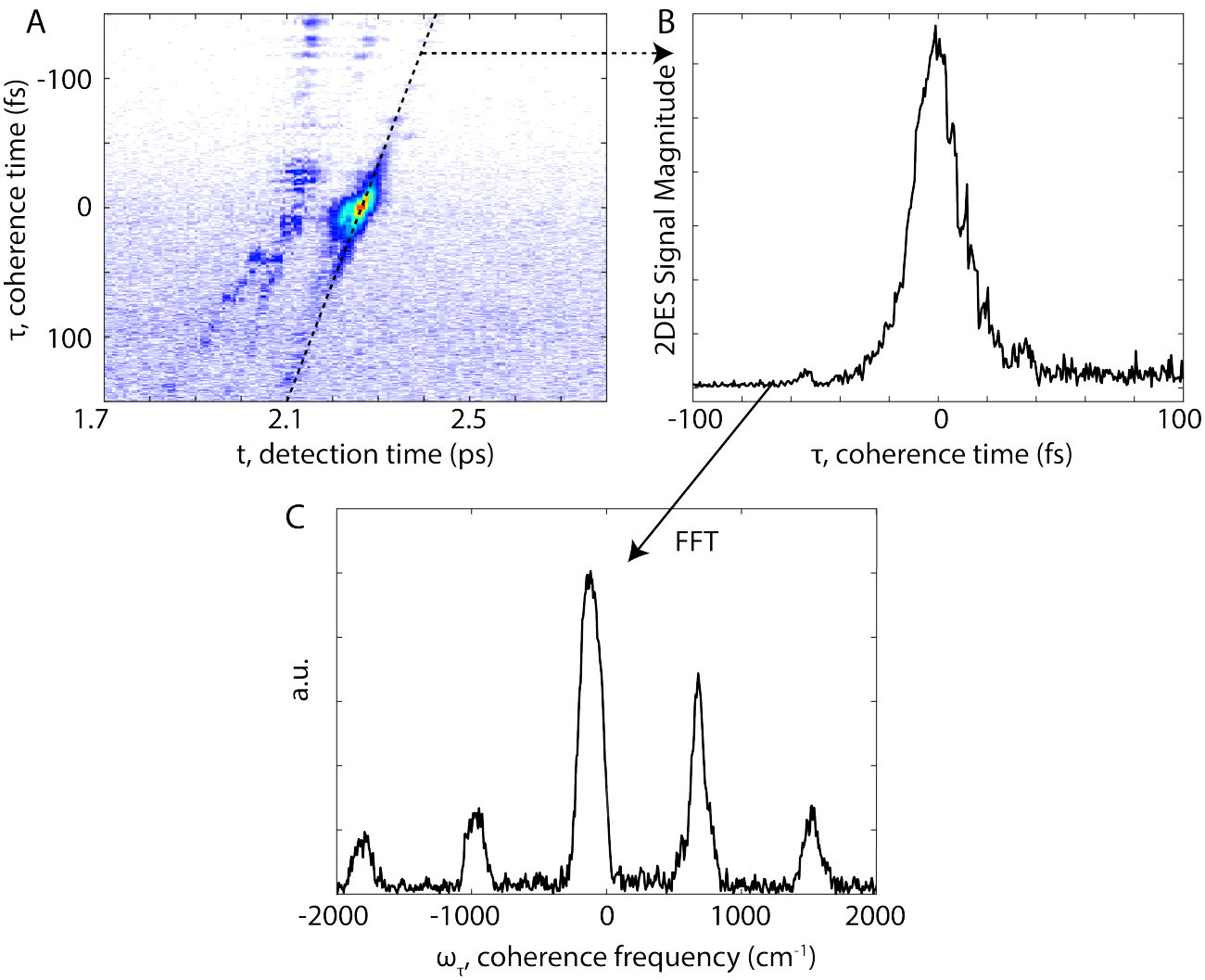

Figure 2.12: (A) GRAPES signal of the laser dye IR144 in the τ-t domain at T = 265 fs. Fourier transformation about ω_t of the scatter subtracted acquired signal. The signal appears $\sim$2.1 ps after the L.O.. (B) A cut through the dashed line in (A) shows the 2DES signal versus the coherence time. (C) Rotating frame detection. Fourier transform of a cut through the GRAPES signal shows that the signal is detected near zero frequency in ω_τ.

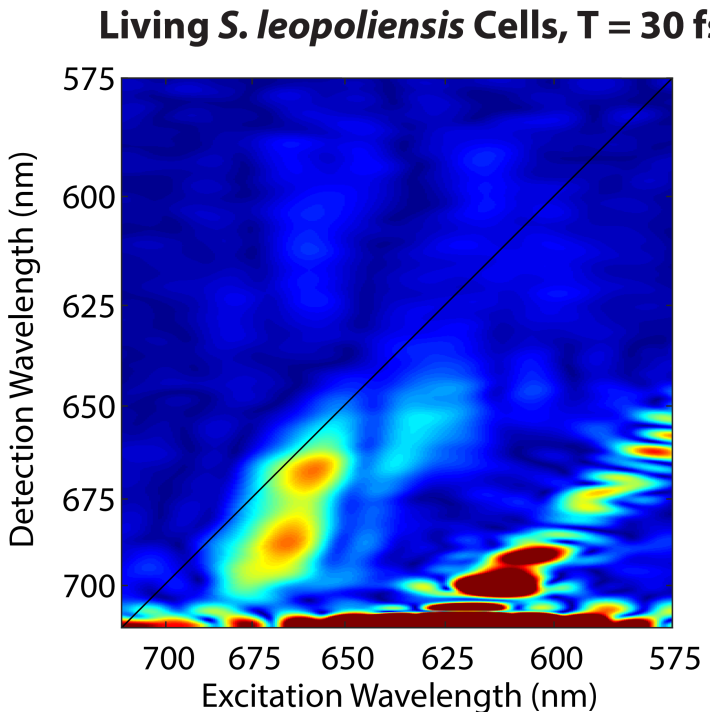

Figure 2.13: Scatter parallel to the diagonal interferes with weak signals from highly scattering *S. leopoliensis* cells when this signal is detected very close to zero frequency in the rotating frame.

now made this imperfect BoxCARS alignments the standard alignment for GRAPES. This ensures that, for highly scattering samples, the signal is not obscured by diagonal scatter. In this imperfect distorted BoxCARS alignment, the signal and the L.O. are no longer co-propagating. As such, the spatial filter used to block beams 1, 2, and 3 but allow the signal and the L.O. to pass through needed to be modified. Figure 2.15 shows the newly designed spatial filter. Using two separate pieces of aluminum with a single slot in each makes this filter extremely modular. The separation between the L.O. and the signal is controlled by how far the signal is pushed away from zero frequency in the rotating frame.

2.2.6 Using Spatial Masks to Reduce Scattered Light at the Spectrometer

In an effort to further reduce the scattered light getting to the detector while measuring highly scattering samples, such as living cyanobacteria, we use additional spatial filters. We use a spatial filter immediately following the sample cell to reduce the scatter from beams 1 and 2 that makes it to the detector. As seen in Figure 2.15, with a highly scattering live cell sample there is still a large amount of scattered light that passes through the filter. We have made the slot in the filter as narrow as it can be without clipping the signal and the L.O..

2.2.7 Using Slower Acquisition Speed to Increase Signal-to-Noise

GRAPES was originally designed as a single-shot spectrometer. [1, 8] Later, it was modified to be able to filter in the ω_T domain and became Ultrafast Video Acquisition (UVA) GRAPES. [12, 13] UVA GRAPES enabled acquisition of 8192 complete 2DES spectra in 3.5 seconds. Using a high-speed CMOS camera (Phantom Miro M310), the acquisition speed in GRAPES was only limited by the 5 kHz repetition rate of the regenerative amplifier. [12] Acquiring spectra with UVA GRAPES required less long-term laser and sample stability because the measurement time was so short. However, for extremely weak signals, the number

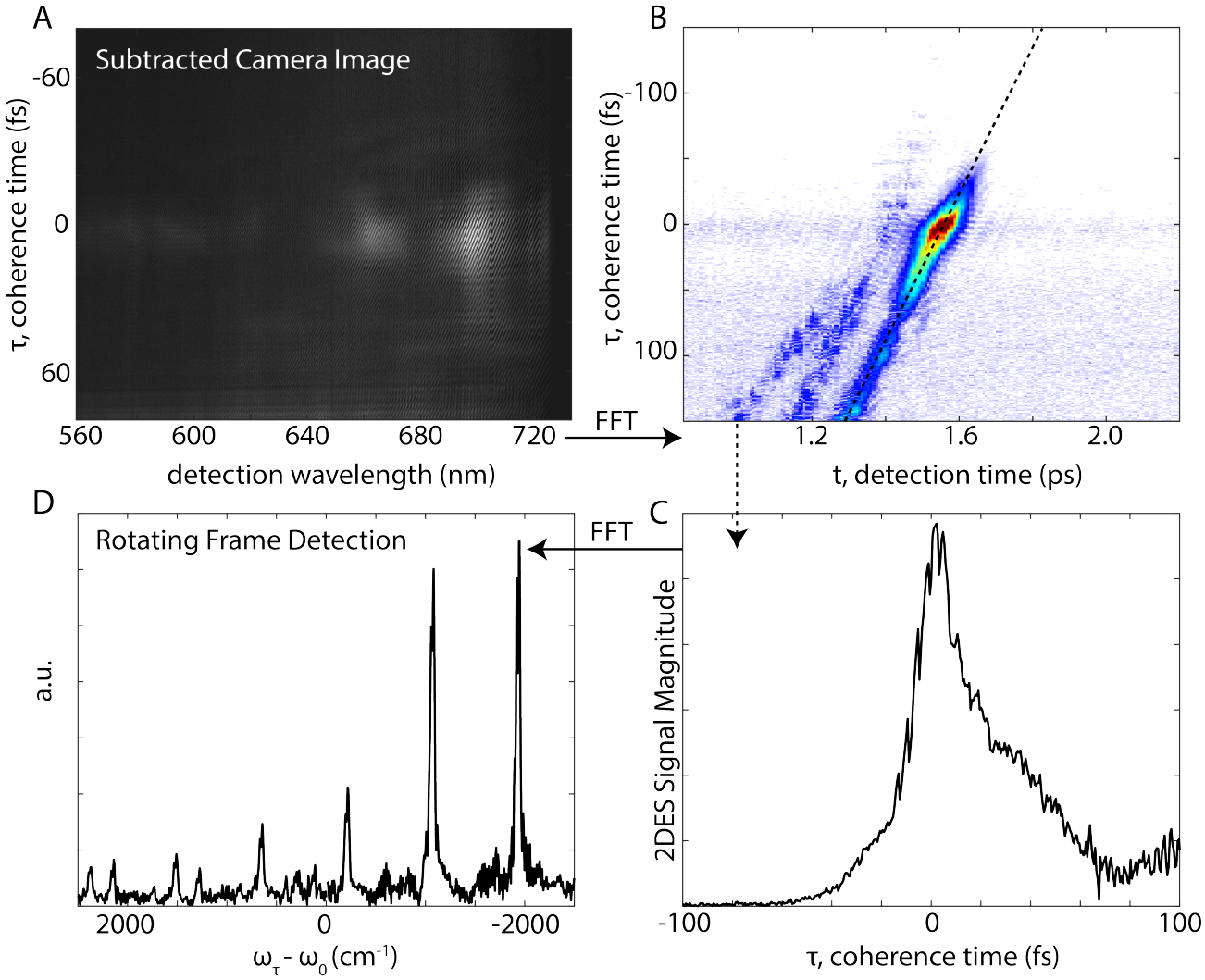

Figure 2.14: (A) A subtracted camera image for a single waiting time. The vertical gradient between the signal and the L.O. gives rise to a checkerboard pattern of the heterodyned signal on the camera. (B) A τ versus t plot after taking a Fourier transform over the detection axis from (A). (C) A cut through the dashed line in (B) shows the 2DES signal versus coherence time. Oscillations on top of the signal result from the vertical gradient between the signal and the L.O.. (D) Rotating frame detection. Fourier transform of a cut through the GRAPES signal (C) shows that the signal is not detected near zero frequency in this alignment of the optical setup (imperfect distorted BoxCARS.)

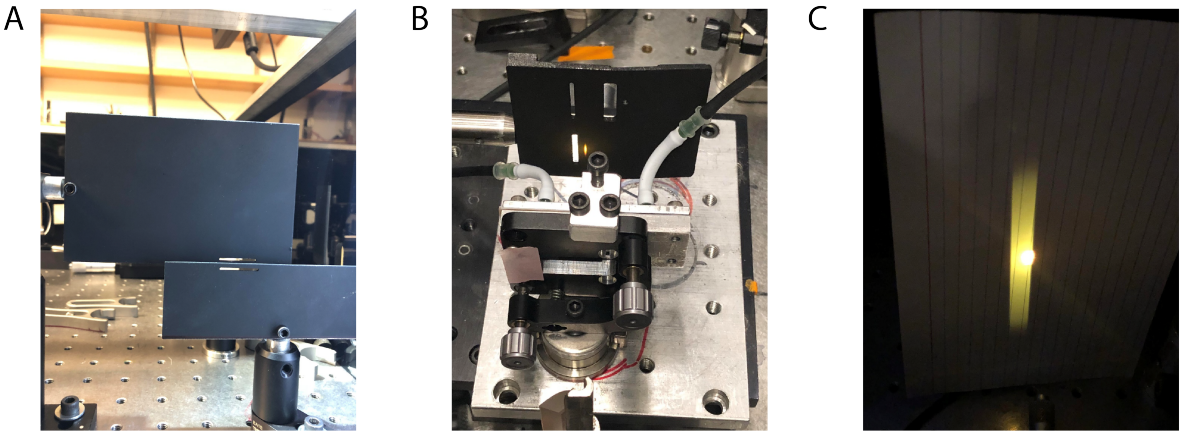

Figure 2.15: (A) In an imperfect distorted BoxCARS geometry, the signal and the L.O. do no co-propagate. Separate spatial filters are used to allow the L.O (bottom) and the signal (top) to be separated from scatter and beams 1, 2, and 3. (B) For highly scattering cyanobacterial cells, a second spatial filter that blocks beams 1 and 2 and scatter was added immediately behind the sample cell as a method to reduce the number of scattered photons that make it to the detector. (C) Signal, L.O., beam 3, and scatter caught on an index card immediately after the spatial filter in (C). This photograph is intended to illustrate just how highly scattering these cyanobacterial cells are.

of laser shots averaged to produce a single spectrum was limited by the minimum acquisition speed on the camera. The slowest possible frame rate on the Phantom Miro is 50 Hz, corresponding to averaging 100 laser shots to produce a single 2DES spectra. Running at a 50 Hz frame rate, data acquisition took around 8 minutes with 3 to 4 additional minutes after the data was collected to save the frames to a cine flash drive. The cine flash could hold 4 data runs before the data needed to be transferred to a hard drive and cleared from the cine flash. [3, 4] In order to average more laser shots to produce a single 2D spectrum, we opted for a new camera that could run at slower frame rates. The Andor Neo 5.5 sCMOS camera has a maximum frame rate of 30 Hz for the entire 2560 by 2160 sCMOS array detector. We can therefore average more laser shots for each 2DES spectrum collected. Now, our acquisition speed is limited by the optical chopper we use to block beam 1/2 for scatter subtraction. The optical chopper can only run reliably at 4 Hz. This rate for the optical chopper corresponds to running the camera at 8 Hz as every other frame contains signal plus L.O. plus scatter from all beams while the others contain only L.O. and beam 3 scatter. A frame rate of 8 Hz corresponds to averaging 625 laser shots to produce a single 2DES spectrum.

The Neo also offers additional advantages over the Miro. The pixel size on the Neo detector is 6.5 μm compared to a 20 μm pixel on the Miro. The angle of beam 1 relative to beam 2 defines the coherence time gradient along the vertical axis of the detector. For the Miro, the optical geometry corresponded to 0.9 fs/pixel. Due to the smaller pixels on the Neo detector, we can achieve 0.29 fs/pixel, enabling us to sample the coherence time much more finely. In order to improve signal-to-noise, keep measurement times reasonable, and save computing power, we have opted to bin in both dimensions on the Neo detector, making it an effective 1080 by 1280 detector with 13 μm square pixels. The binning results in a coherence time gradient along the vertical dimension of the detector of 0.58 fs/pixel. This resolution in coherence time is still better than what we was achievable with the Miro.

Unlike the Miro, the Neo is capable of writing the data to disk in real time. The data is saved to 1 TB solid state hard drive and no time is wasted saving or transferring data. The data is transferred from the acquisition computer to other hard drives for long-term storage and processing over a 1 GB/s wireless network.

2.3 Sample Preparation of Cyanobacterial Membrane Fragments and Living Cells

2.3.1 Culturing Synechocystis and Synechoccocus Cells

This thesis contains data from living *Synechoccocus leopoliensis* cells and *Synechocystis* sp. PCC 6803 thylakoid membranes. Both cyanobacterial cultures were grown in BG-11 media. A 50 X solution of BG-11 media was purchased (Sigma-Aldrich) and diluted accordingly with DI water to use for cyanobacterial cell growth. The diluted BG-11 was autoclaved in flasks with stir bars and foam stoppers. After autoclaving, media was left to cool in a sterile hood under UV lights. Cells were transferred to the media in the sterile hood to limit contamination risks. The culture flasks were placed on stir plates under the room lights (fluorescent) to grow (Figure 2.16B). Stir plates were set to maintain a medium to high level of agitation. For culturing *Synechocystis* sp. PCC 6803 cells, 1M TES/KOH solution should be added to the autoclaved media to a final concentration of 10 mM. Mutant cell strains, PSI-only and PSII-only, require the addition of glucose to the media to a final concentration of 5 mM. The PSII-only strain must be grown in the dark. These cultures were wrapped completely in aluminum foil to limit light exposure. [14] Cell media was refreshed once every month. Existing cell cultures were centrifuged for 10 minutes at 5,000 rpm (Sorvall RC-5B centrifuge, Sorvall SLA-3000 Super-Lite rotor). The supernatant was discarded and the pellets were re-suspended in the fresh media. Linear absorption spectra for living cultures of *S. leopoliensis* and *Synechocystis* sp. PCC 6803 are presented in Figure 2.16A.

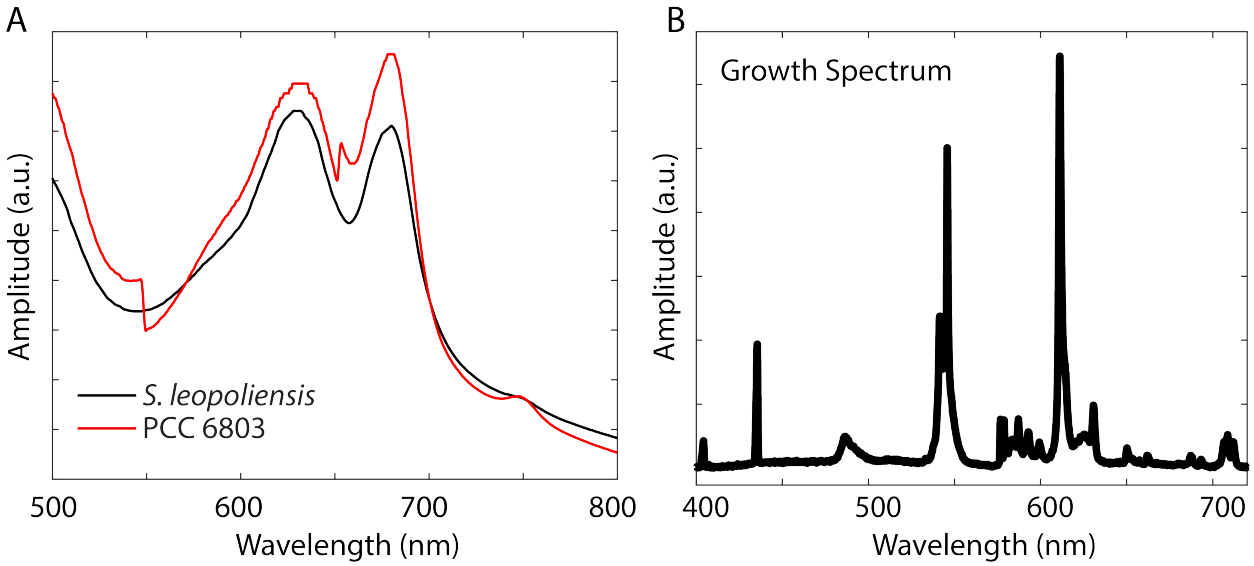

Figure 2.16: (A) Linear absorption spectra of *S. leopoliensis* and *Synechocystis* sp. PCC 6803 cells. Spectra presented here are of cell cultures that have been pelleted and re-suspended in a small volume of water/glycerol mixture for use in 2DES experiments. (B) Spectrum of fluorescent lights that were used to grow the cyanobacteria in (A) photosynthetically.

2.3.2 Protocol for Preparing Cyanobacterial Membrane Fragments

The procedure for preparation of intact thylakoid membranes from cyanobacteria was provided and executed by our collaborators in Prof. Neil Hunter's group at the University of Sheffield, Dr. Andrew Hitchcock and Dr. Craig MacGregor-Chatwin. Drs. Hitchcock and MacGregor-Chatwin grew wild-type (WT), PSI-only, and PSII-only *Synechocystis* sp. PCC 6803 cells and prepared the intact thylakoid membranes. They sent us the membranes on dry ice for use in 2DES and pump-probe experiments. The entire isolation process should be done under low light. Cell fragments should be kept on ice or in the fridge as much as possible to maintain the integrity of the samples. Cells are pelleted using centrifugation. The supernatant is discarded and the pellet is resuspended in a small volume of FLAG buffer (recipe found in Table 2.3.2). The re-suspended cells are homogenized using a bead homogenizer (Benchmark Scientific BeadBug™ Microtube Homogenizer). The re-suspended cells are mixed with an equal volume of 0.1 mm glass beads. The bead homogenizer is run for 8

x 55 s at maximum speed with 1 minute on ice in between each iteration of homogenization. After the cells are homogenized, the beads are removed using a slow spin at 4,000 rpm for 2 minutes. The cell debris can be pipetted off. The beads are washed with a small volume of FLAG buffer and spun again at 4,000 rpm. The supernatant is combined with the rest of the cell lysate to ensure maximal recover of the sample. Thylakoid membranes can be separated from dissociated phycobilisomes using ultracentrifugation (20 minutes at 23,000 rpm). The blue supernatant containing the phycobilisomes can be discarded (they do not remain intact once dissociated from the membrane in this protocol). The pellet contains large cell debris and intact thylakoids. A slow spin can separate these components. The pellet from the ultracentrifugation step is resuspended in FLAG buffer and spun slowly to pellet cell debris. The supernatant contains intact thylakoids. If needed, the membranes can be further purified using a 1-2 sucrose gradient. Prepared thylakoid membranes were diluted with DI water to an optical density of 0.6 to 0.8 in 1 mm for 2DES and pump-probe experiments.

Table 2.1: FLAG Buffer Recipe

Component	Concentration
Sodium phosphate	25 mM, pH 7.4
Magnesium chloride	10 mM
Sodium chloride	50 mM
Glycerol	10% w/v
EDTA-free protease inhibitor (Roche)	1 tablet/50 mL FLAG buffer

2.3.3 Live Cell Preparation for Ultrafast Measurements

2DES spectra of living cyanobacterial cells were successfully collected for *S. leopoliensis* cells. Cell samples of *S. leopoliensis* for 2DES experiments were prepared by centrifuging $\sim$ 300 ml of actively growing cells at 5,000 rpm for 10 mins. The supernatant was discarded and the pelleted cells were resuspended in 1 mL of DI water. Then 1 ml of glycerol was added to the cells. After pipeting up and down many times to ensure mixing, the cell sample was

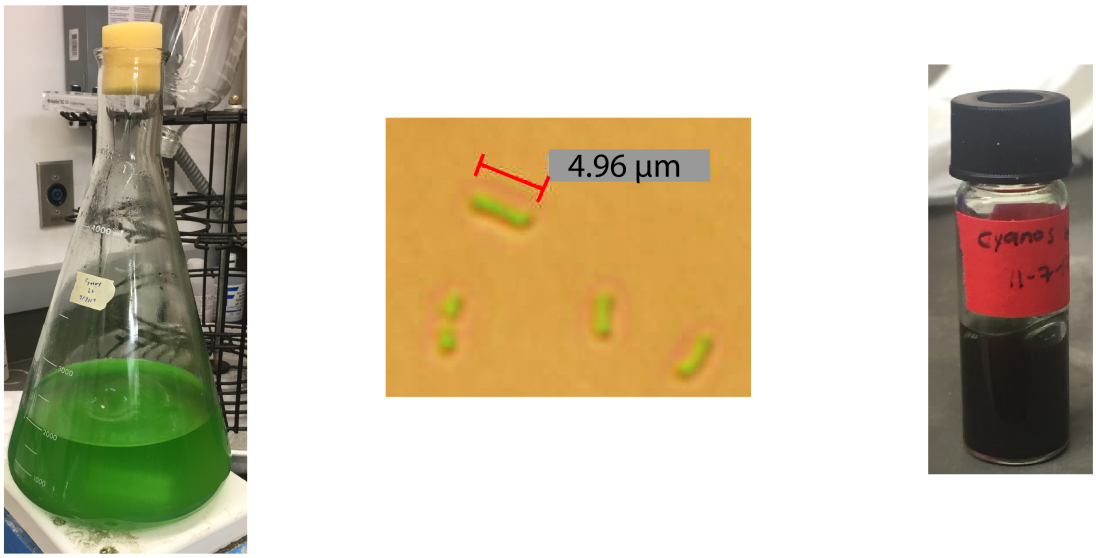

Figure 2.17: (Left) Culture flask containing *S. leopoliensis* cells. (Middle) Micrograph of *S. leopoliensis* cells. (Right) Sample vial of *S. leopoliensis* cells used for 2DES experiments.

characterized by UV-vis spectroscopy (Figure 2.16). The sample was further diluted with a solution of 50:50 water/glycerol to a final optical density of 0.5 to 0.6 above the scatter baseline in 1 mm. Figure 2.17 shows an *S. leopoliensis* culture flask, a micrograph of the cells, and the sample vial with the final prepared sample used for 2DES experiments.

REFERENCES

[1] Elad Harel, Andrew F. Fidler, and Gregory S. Engel. Real-time mapping of electronic structure with single-shot two-dimensional electronic spectroscopy. *Proceedings of the National Academy of Sciences*, 107(38):16444–16447, 2010.

[2] S. H. Sohail, P. D. Dahlberg, M. A. Allodi, S. C. Massey, P. C. Ting, E. C. Martin, C. N. Hunter, and G. S. Engel. Communication: Broad manifold of excitonic states in light-harvesting complex 1 promotes efficient unidirectional energy transfer *in vivo*. *J Chem Phys*, 147(13):131101, 2017.

[3] Sara C. Massey, Po-Chieh Ting, Shu-Hao Yeh, Peter D. Dahlberg, Sara H. Sohail, Marco A. Allodi, Elizabeth C. Martin, Sabre Kais, C. Neil Hunter, and Gregory S. Engel. Orientational dynamics of transition dipoles and exciton relaxation in LH2 from ultrafast two-dimensional anisotropy. *The Journal of Physical Chemistry Letters*, 10(2):270–277, 2019.

[4] Peter D. Dahlberg, Po-Chieh Ting, Sara C. Massey, Marco A. Allodi, Elizabeth C. Martin, C. Neil Hunter, and Gregory S. Engel. Mapping the ultrafast flow of harvested solar energy in living photosynthetic cells. *Nature Communications*, 8(1):988, 2017.

[5] Marco A. Allodi, John P. Otto, Sara H. Sohail, Rafael G. Saer, Ryan E. Wood, Brian S. Rolczynski, Sara C. Massey, Po-Chieh Ting, Robert E. Blankenship, and Gregory S. Engel. Redox conditions affect ultrafast exciton transport in photosynthetic pigment–protein complexes. *The Journal of Physical Chemistry Letters*, 9(1):89–95, 2018.

[6] Aleksei M. Zheltikov. Let there be white light: supercontinuum generation by ultrashort laser pulses. *Physics-Uspekhi*, 49(6):605, 2006.

[7] Y.R. Shen. The principles of nonlinear optics. 2003.

[8] Elad Harel, Andrew F. Fidler, and Gregory S. Engel. Single-shot gradient-assisted photon echo electronic spectroscopy. *The Journal of Physical Chemistry A*, 115(16):3787–3796, 2011.

[9] Patrick L. Kramer, Chiara H. Giammanco, Amr Tamimi, David J. Hoffman, Kathleen P. Sokolowsky, and Michael D. Fayer. Quasi-rotating frame: accurate line shape determination with increased efficiency in noncollinear 2D optical spectroscopy. *Journal of the Optical Society of America B*, 33(6):1143–1156, 2016.

[10] Allison W. Albrecht, John D. Hybl, Sarah M. Gallagher Faeder, and David M. Jonas. Experimental distinction between phase shifts and time delays: Implications for femtosecond spectroscopy and coherent control of chemical reactions. *The Journal of Chemical Physics*, 111(24):10934–10956, 1999.

[11] Peter Hamm and Martin Zanni. Concepts and methods of 2D infrared spectroscopy. 2011.

[12] Peter D. Dahlberg, Andrew F. Fidler, Justin R. Caram, Phillip D. Long, and Gregory S. Engel. Energy transfer observed in live cells using two-dimensional electronic spectroscopy. *The Journal of Physical Chemistry Letters*, 4(21):3636–3640, 2013.

[13] Peter D. Dahlberg, Graham J. Norris, Cheng Wang, Subha Viswanathan, Ved P. Singh, and Gregory S. Engel. Communication: Coherences observed *in vivo* in photosynthetic bacteria using two-dimensional electronic spectroscopy. *The Journal of Chemical Physics*, 143(10):101101, 2015.

[14] Sara C. Massey. Ultrafast energy transfer and orientational dynamics in photosynthetic bacterial membranes. *ProQuest Dissertations and Theses*, page 132, 2019.

CHAPTER 3

BROAD MANIFOLD OF EXCITONIC STATES IN LIGHT-HARVESTING COMPLEX 1 PROMOTES EFFICIENT UNIDIRECTIONAL ENERGY TRANSFER *IN VIVO*

[Adapted with permission from Reference [1]]

In photosynthetic organisms, the pigment-protein complexes that comprise the light-harvesting antenna exhibit complex electronic structures and ultrafast dynamics due to the coupling among the chromophores. Here, we present absorptive two-dimensional (2D) electronic spectra from living cultures of the purple bacterium, *Rhodobacter sphaeroides*, acquired using GRadient Assisted Photon Echo Spectroscopy (GRAPES). Diagonal slices through the 2D lineshape of the LH1 stimulated emission/ground state bleach feature reveal that a higher energy state within the B875 manifold of LH1 is populated at early waiting times. The waiting time evolution of diagonal, horizontal, and vertical slices through the 2D lineshape show a sub-100 fs intra-complex relaxation through which the higher energy population relaxes into a lower energy state in the B875 manifold. The 855 nm absorption of the higher energy excitonic state occupied at early waiting times optimizes spectral overlap between the LH1 B875 band and the B850 band of LH2. Access to an energetically broad distribution of excitonic states within B875 offers a mechanism for efficient energy transfer from LH2 to LH1 during photosynthesis while limiting back transfer. Two-dimensional lineshapes reveal a rapid decay in the ground-state bleach/stimulated emission of B875. This signal, identified as a decrease in dipole strength of a strong transition in LH1 on the red side of the B875 band, is assigned to the rapid localization of an initially delocalized exciton state, a dephasing process that frustrates back transfer from LH1 to LH2.

3.1 Background on Ultrafast Spectroscopies of Living Cells

Photosynthetic light harvesting machinery has evolved highly efficient energy transfer processes to power an organism's metabolism using solar photons [2–4]. Light-harvesting complexes funnel excitations to the reaction center where charge separation is initiated; the dynamics of this photosynthetic excitonic energy transfer occur on the femtosecond to picosecond timescale [5]. Two-dimensional electronic spectroscopy (2DES) probes this energy transfer process using a sequence of ultrafast laser pulses. [6–10] 2DES correlates excitations at specific frequencies to the ground state bleach, stimulated emission, and excited state absorption signals they generate with femtosecond time resolution. The position, lineshape, and dynamics of 2DES spectral features are determined by the underlying electronic and vibrational structure of the system. [11–14]

Recent advances in GRadient Assisted Photon Echo Spectroscopy (GRAPES) have enabled 2DES spectra of highly scattering samples, including intact cells. [15, 16] However, to date, only measurement of the rephasing photon echo signal was feasible without alteration of the experimental geometry, [17] precluding direct acquisition of fully absorptive 2DES spectra, which offer the highest degree of spectral resolution. In complex systems, analysis of the fully absorptive 2DES spectra is critical to properly quantify and assign spectral dynamics and determine homogeneous and inhomogeneous contributions from a diverse ensemble. [18] Here, we present absorptive 2D spectra of the photosynthetic antenna complexes, light-harvesting complex 1 (LH1) and light-harvesting complex 2 (LH2), in living cells of the purple bacterium *Rhodobacter (Rba.) sphaeroides*. We observe ultrafast relaxation of an inhomogeneous distribution of chromophores on a sub-100 fs timescale in wild type (WT) cells, LH2-only cells, and LH1-only cells. In LH1-only cells, we also observe ultrafast intra-complex energy relaxation within a manifold of higher lying excitonic states. Acquisition of these spectra requires an experimental advance in GRAPES methodology that enables the simultaneous acquisition of both the rephasing photon echo and nonrephasing free induction

decay signals.

3.2 Ultrafast Energy Transfer Dynamics in *Rhodobacter sphaeroides*

In WT *Rba. sphaeroides*, LH1, the core pigment-protein antenna complex, forms a dimeric complex around the reaction center while LH2 is a peripheral pigment-protein antenna complex. [19] LH2 transfers energy to LH1 on a 5-7 ps timescale. [20, 21] LH1 then transfers the excitation to the reaction center special pair on a 35 ps timescale. [22] LH2 contains B800 and B850 rings of bacteriochlorophyll *a* (BChl *a*). [23] The B850 ring consists of 18 strongly coupled BChl *a* molecules ($\sim$300 cm^{-1}), while the 9 BChl *a* in B800 are weakly coupled ($\sim$20 cm^{-1}). [22] Each LH1 dimer contains an S-shaped arrangement of strongly coupled ($\sim$300 cm^{-1}) BChl *a* molecules denoted as B875. [24, 25]

3.3 Recovering Absorptive Lineshapes using GRadient Assisted Photon Echo Spectroscopy (GRAPES)

2DES is a third-order nonlinear optical spectroscopy that provides information similar to transient absorption but with spectral resolution in both the excitation and detection axes. In a 2DES experiment, three incident electric fields generate an oscillating polarization which gives rise to a nonlinear signal in a unique phase-matched direction. The signal is heterodyne detected through interference with a reference pulse. A 2D scan of the time between pulses 1 and 2 (coherence time, τ) and the time between pulses 2 and 3 (waiting time, T) generates a 2D spectrum that correlates excitation energy with detection energy for each T. [27]

Interactions with pulses 1 and 3 generate oscillating polarizations that acquire phase with either the same or opposite sign, corresponding to nonrephasing and rephasing signals, respectively. These signals are generated in distinct phase-matched directions. The rephasing

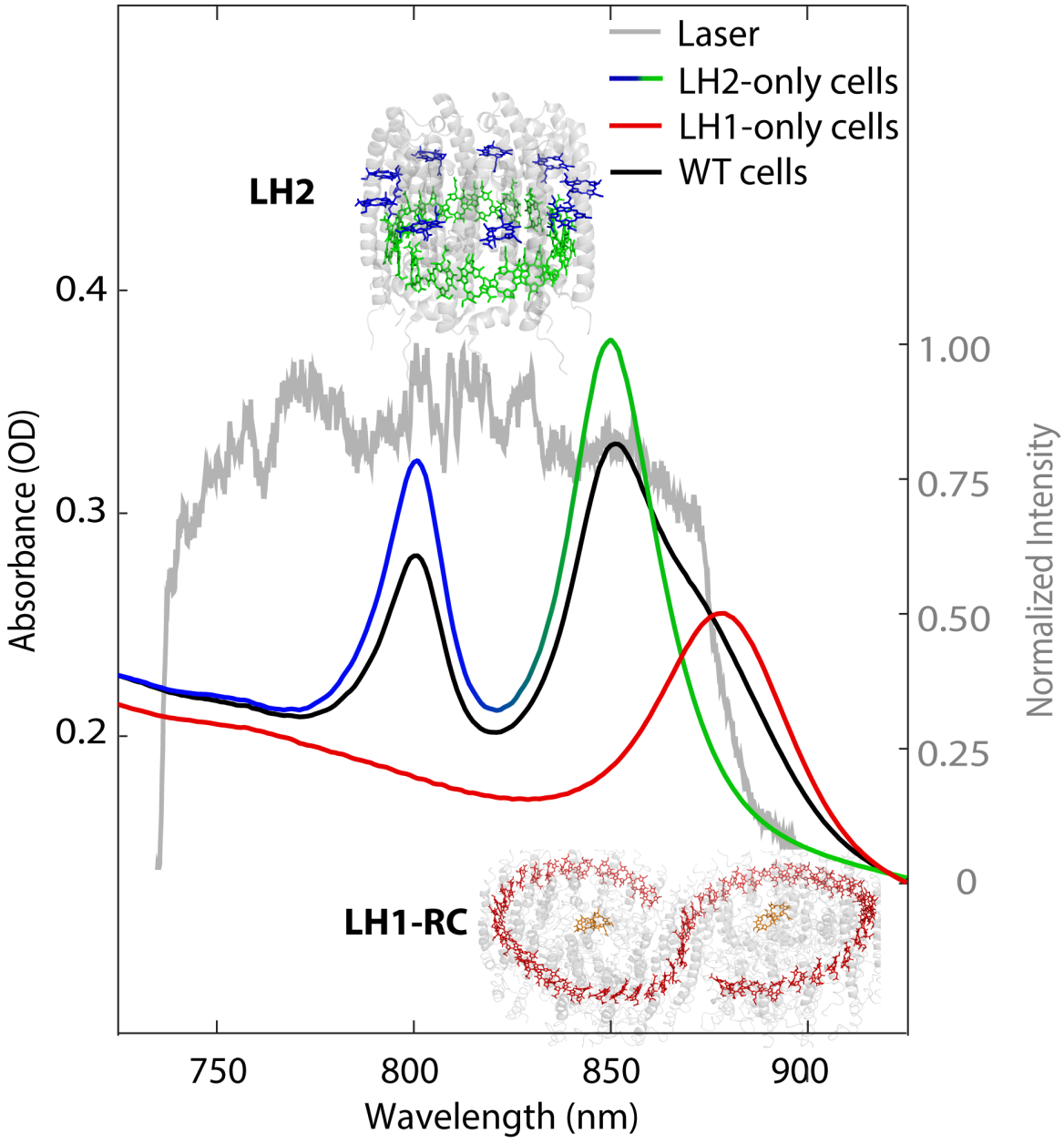

Figure 3.1: Excitation spectrum in gray and absorption spectra of LH2-only cells (blue-green), LH1-only cells (red), and wild-type (WT) cells (black). The crystal structures of LH2 (PDB ID: 1NKZ) [26] and LH1-RC dimer (PDB ID: 4V9G) [24] are shown in colors corresponding to their linear absorption traces.

or nonrephasing spectra separately contain phase-twisted lineshapes with both absorptive and dispersive components (Figure 3.7). Absorptive spectra are obtained by summing the nonrephasing and rephasing signals. Often, the time order of the first two pulses in a 2DES sequence is switched to enable detection of both the rephasing and nonrephasing signals in a single phase-matched direction. [28] However, changing the pulse time-ordering requires two sequential measurements to calculate the fully absorptive 2DES spectra. Laser drift and sample degradation during the measurement may alter the conditions under which the rephasing or the nonrephasing signals are collected; thus, summation may not preserve the true dynamics or lineshape.

GRAPES spectra are acquired by focusing the pulses to lines, rather than points, and geometrically tilting the wavevector of pulse 1 relative to pulse 2, thereby spatially encoding the range of coherence time delays (Figure 3.2). [29, 30] As a result, all coherence times are encoded in each laser shot. Consequently, we collect a complete 2D spectrum with each laser shot, meaning we only need to scan over T, the time between pulses 2 and 3. The technical details of the GRAPES instrument are described in Section 3.7. In short, the temporal tilt imparted on pulse 1 relative to pulse 2 spatially encodes both positive and negative coherence times for each T; however, this tilt results in a gradient of waiting times for negative coherence times in a single laser shot, which restricts the acquisition of both the rephasing and nonrephasing signals.

Here, by integrating over 100 laser shots in each signal frame, we rapidly acquire (25 Hz) a series of GRAPES spectra while continuously scanning the waiting time delay stage (stage speed 25 fs/s) which yields 1 fs waiting time steps. We make use of our fine waiting time sampling to reconstruct a uniform waiting time for negative coherence times. By selecting signals generated from different frames (Figure 3.2, top), we can linearly interpolate the signals to reconstruct negative coherence time data with a uniform waiting time (Figure 3.2, bottom). This interpolation rectifies the temporal gradient between pulses 1 and 3, which

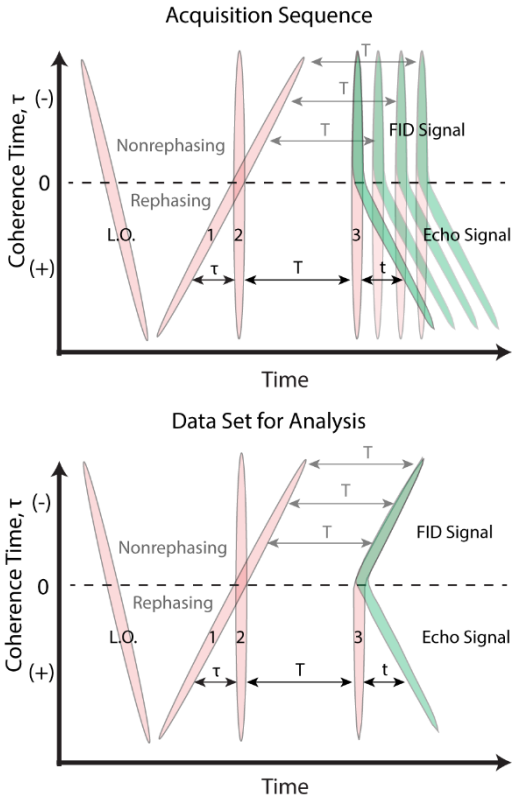

Figure 3.2: (Top) The pulse sequence used in GRAPES that generates both third-order nonlinear rephasing photon echo and nonrephasing free induction decay (FID) signals in the same phase-matched direction. (Bottom) The finely sampled time delay between pulses 1 and 3, generates, for the purpose of analysis, a dataset that permits nonrephasing signal at a constant waiting time (T) to be reconstructed from the raw data.

previously prohibited the measurement of nonrephasing signals from GRAPES without also changing the experimental geometry or acquisition sequence. The interpolation is simplified by GRAPES data being acquired in the rotating frame, which eliminates fast oscillatory behavior. [29] In this way, we collect both the rephasing photon echo and the nonrephasing free induction decay signals in a single dataset.

3.4 Absorptive 2DES Spectra of Living *Rba. sphaeroides cells*

We use the absorptive 2D spectra to probe ultrafast events in living Rba. sphaeroides cells, using WT, LH2-only, and LH1-only strains (Figure 3.3). The growth and isolation protocols are detailed in the SI. The 2DES data from the three cell types were phased to pump-probe spectra of membrane fragments (Figure 3.7). [17, 31] Both the WT and LH2-only spectra show diagonal excited state absorption (negative) and stimulated emission and ground state bleach (positive) features at 850 nm and 800 nm, corresponding to the B850 and B800 bands of LH2, respectively. Waiting time traces showing the dynamics of B850, B800, and energy transfer from B800 to B850 (Figure 3.8) agree with prior measurements of LH2. [32] The spectra of LH1-only and WT cells show a diagonal peak around 870 nm corresponding to the B875 chromophores in LH1. [31] The diagonal features in Figure 3.3 all exhibit diagonal elongation at early waiting times, indicating inhomogeneous broadening of the B800, B850, and B875 bands. This elongation disappears by 100 fs, reflecting relaxation within each spectral band. The degree of inhomogeneity in the 2DES absorptive spectra is quantified using nodal line slope (NLS) analysis, which measures the tilt of the slope between the positive and negative features (Figure 3.4). [11, 33, 34]

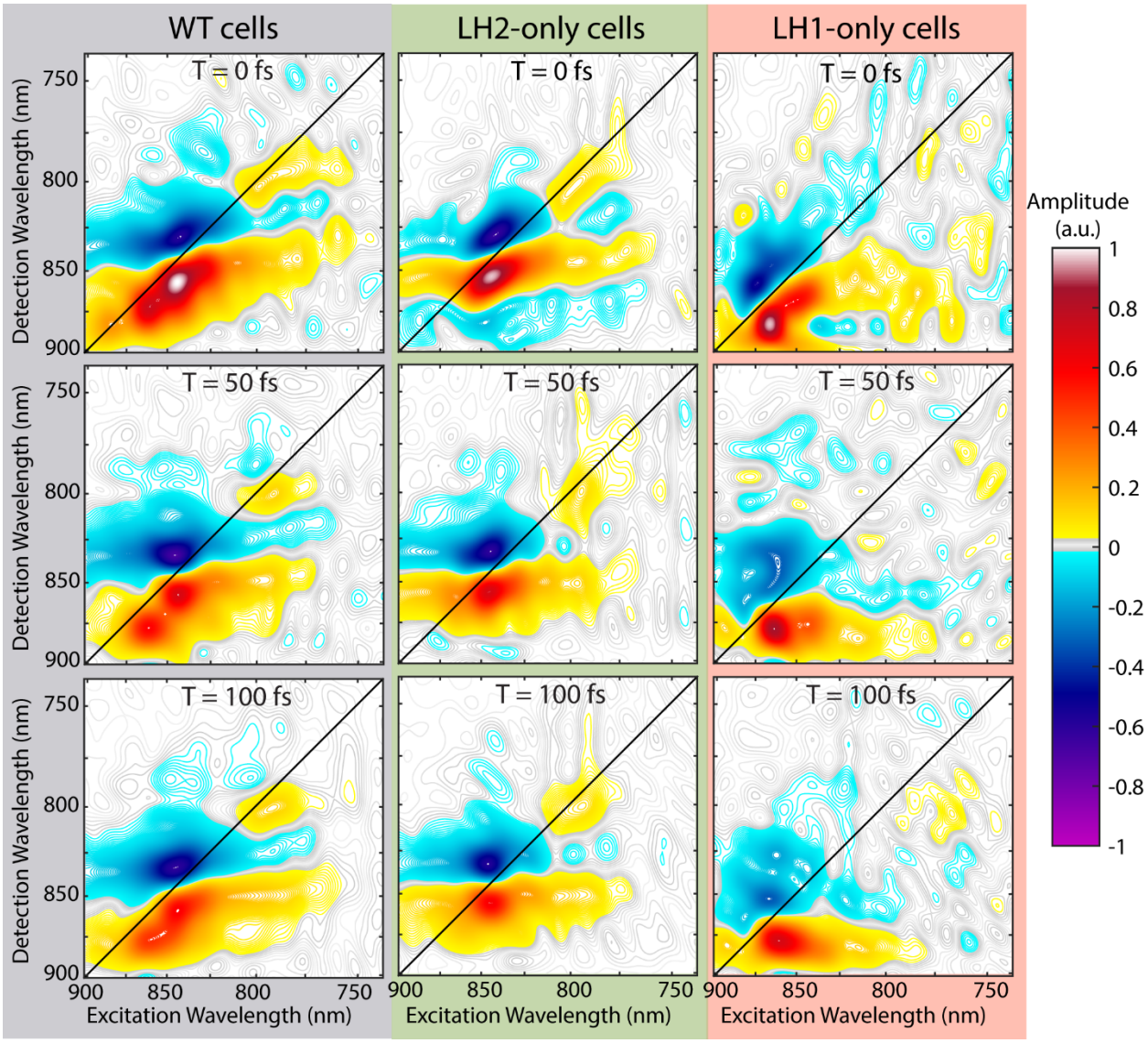

Figure 3.3: Fully absorptive 2DES spectra for WT cells (left), LH2-only cells (center), and LH1-only cells (right); T = 0 fs (top), 50 fs (middle), and 100 fs (bottom). Spectral diffusion from the elongated, inhomogeneous lineshape to a round homogeneous lineshape can be seen as a function of T. The relaxation of the diagonal elongation of the spectral features indicates a loss of correlation between pump and probe energies as the system has had time to relax. The axis labels excitation and detection wavelength refer to the wavelengths resulting from a Fourier transform over the coherence time (τ) and the direct detection of the rephasing wavelength (λ_t), respectively. Axes are plotted as linear in frequency, but labeled by wavelength for ready comparison with linear spectra.

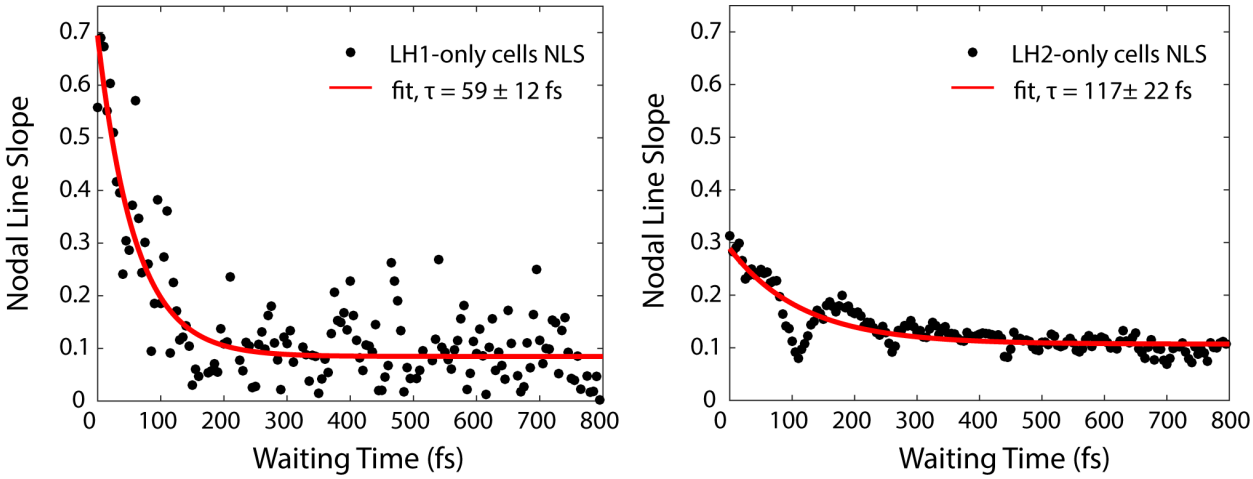

Figure 3.4: Nodal line slope analysis of fully absorptive 2DES spectra for LH1-only (left) and LH2-only (right) cells. The black points show the slope of the nodal line between the positive and negative diagonal spectral features at 850 nm (LH2-only) and 870 nm (LH1-only) as a function of waiting time. The red curves are single exponential fits to the NLS decays.

3.5 Nodal Line Slope Analysis

In the inhomogeneous limit, the timescale of fluctuation is slow compared to the inverse linewidth, leading to diagonally elongated lineshapes and a positive valued NLS at early times when the distribution of chromophores generating a single spectral feature can be captured. As a function of waiting time, the NLS relaxes towards zero as spectral diffusion results in a collection of states which exchange on the timescale of the measurement. [11, 35] After the system has relaxed, round, homogeneously broadened lineshapes result. [11] For LH1- and LH2-only cells spectra, NLS as a function of waiting time (Figure 3.4) indicates that ultrafast lineshape relaxation occurs with time constants of 59 ± 12 fs and 117 ± 22 fs, respectively. The overlap of B850 and B875 features in the WT cell spectra make it challenging to fit the NLS in these spectra; however, qualitatively the nodal line relaxation is consistent with that seen in the LH2- and LH1-only cells (Figure 3.3).

Comparison of the LH1 and LH2 features in the whole cell linear absorption spectra (Figure 3.1) reveals that the spectral signature of LH1's B875 ring is much broader than

that of LH2's B850 ring. The NLS (Figure 3.4) at T = 0 fs in the LH1-only cells 2D spectrum (NLS = ∼0.7) is significantly steeper than that in the LH2-only cells spectrum (NLS = ∼0.3), indicating that the B875 states in LH1 are more inhomogeneously broadened than the B850 states in LH2. The greater degree of inhomogeneity in LH1 compared to LH2 reflects not only an increased number of excitonic states, but also the greater degree of delocalization in LH1 which has been previously reported. [36]

3.6 Two-Dimensional Lineshape Analysis of LH1-only Cells Spectra

Previous 2DES studies of *Rba. sphaeroides in vivo* only presented the rephasing spectra. [15, 16] Here, we present 2D absorptive spectra, which eliminate phase-twist in the lineshapes.10 Access to the 2D absorptive lineshapes of light harvesting complexes in vivo makes characterization of finer spectral features, even at early waiting times, possible. Fitting every point in the LH1-only cells spectra to an independent monoexponential function, $A\exp(-T/\tau) + B$, with no constraints on amplitude or lifetime, shows that the decay lifetimes within B875 are non-uniform. The lifetimes from the monoexponential fits show that the red edge of B875, in both excitation and detection wavelengths, decays faster than the rest of the feature (Figure 3.5B). When implementing a 1D analysis by taking slices through features in the 2D spectra (Figure 3.5C-E), similar to the projection along the detection wavelength axis that would be obtained from a pump-probe experiment, this rapid decay on the red edge of B875 would not be as easily identified. The trends over waiting time in Figure 3.5C-E could look like a loss of intensity on the red edge of B875 or a dynamic blue shift in the central wavelength of the ground state bleach/stimulated emission feature. The observed trend in the dynamics presented in Figure 3.5B gives a clearer picture of the dynamics. The 2D analysis demonstrates a loss on the red edge of B875 which is consistent with ultrafast exciton localization resulting in a decrease in the transition dipole strength on

the red side of the B875 band. This localization is similar to what has been reported for the B850 band of LH2. [37] We do not observe an analogous spectral pattern of decay times in the B850 feature of the LH2-only cells, though we see an ultrafast decay in the amplitude of the B850 feature (Figure 3.6), consistent with B850 being more homogeneous than B875 and previous reports on exciton localization in LH2. [15, 37] The exciton localization on the red edge of B875 in LH1 would limit back transfer to LH2, but exactly how this rapid relaxation would impact transfer from LH1 to the reaction center and the role of the local environment in this process are the subjects of ongoing research. The collapse of the B875 transition dipole was previously observed in 2DES rephasing spectra of LH1 membranes [31] and in 3PEPS spectra of isolated LH1 [38]; however, without absorptive lineshapes it is difficult to interpret shifting spectral features.

The spectrum of decay times in Figure 3.5B also shows the rapid decay of a higher energy B875 population at excitation wavelength = 850 nm, detection wavelength = 870 nm. The diagonal slices through B875 (Figure 3.5C) reveal a bimodal distribution consisting of a lower energy population at excitation wavelength = 865 nm, detection wavelength = 880 nm and a higher energy population at excitation wavelength = 850 nm, detection wavelength = 870 nm. The higher energy population relaxes within 100 fs, as seen by the loss of the high energy distribution in the diagonal slices and the growth of intensity at excitation wavelength = 850 nm in the horizontal slices through detection wavelength = 880 nm (Figure 3.5E). This redistribution reflects an ultrafast intra-complex relaxation with a time constant < 50 fs.

Relaxation within the LH1 manifold occurs on the same timescale as spectral diffusion, as indicated by NLS analysis (Figure 3.4). We suggest that the occupation of higher lying B875 states at early times heavily contributes to the inhomogeneity measured using NLS. Previous work on LH1 using transient absorption spectroscopy showed a dynamic red shift of the B875 spectral feature on the 130-150 fs timescale, though these measurements were limited by an instrument response function of 150 fs. [39] This dynamic red shift was more pronounced

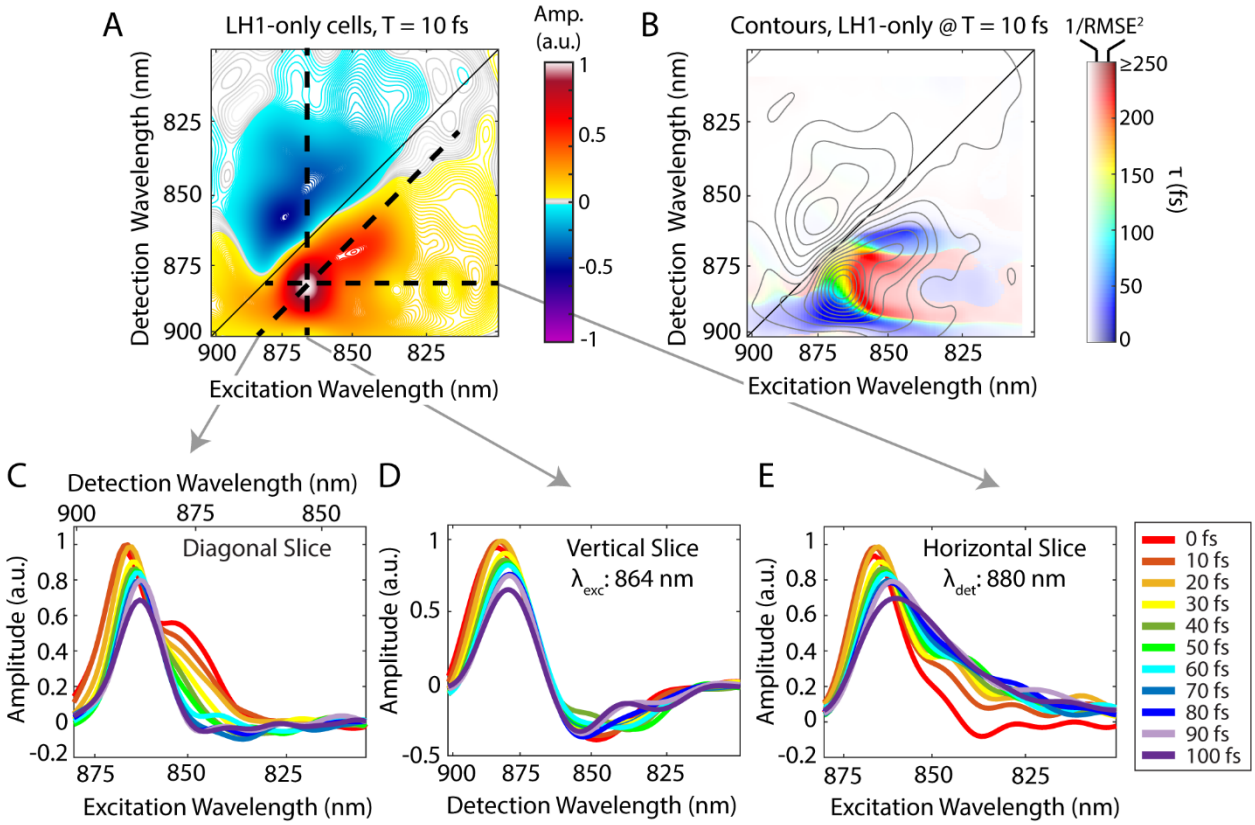

Figure 3.5: (A) T = 10 fs spectrum of LH1-only cells. Black dashed lines indicate the locations of diagonal, vertical, and horizontal slices represented in C-E, respectively. (B) The decay time at each point in the LH1-only cells spectra from a monoexponential fit ($A\exp(-T/\tau) + B$) at each point in the 2D spectrum. The color saturation is based on the root-mean-squared-error for the fit at each point. The gray contour depicts the 2DES spectrum at T = 10 fs. The (C) diagonal, (D) vertical, and (E) horizontal slices through the B875 stimulated emission/ground state bleach feature as a function of waiting time.

upon blue side excitation of B875 [39] and was attributed to downhill ultrafast excitonic relaxation in complementary Redfield theory calculations. [40] Our 2DES spectra indicate that, while the average absolute maximum of the stimulated emission/ground state bleach feature shifts slightly to a lower energy (red shifts), the population originally occupying the higher energy excitonic states within B875 selectively relaxes into a lower energy state at 880 nm. In a transient absorption measurement such as those reported by Monshouwer et al. [39], this intra-complex relaxation would look like a dynamic red shift of the spectral feature. In our 2D spectra, we see this relaxation as the movement of the blue side of the B875 feature from its diagonal position at T = 0 fs to a lower diagonal position by T = 100 fs (Figure 3.3, right). Energy distributed through the broad manifold of LH1 states [31] is rapidly funneled into the lowest energy state, as exciton relaxation occurs.

Access to higher energy states within B875 offers an advantage for *Rba. sphaeroides* during light harvesting. The efficiency of this process depends on how well excitation energy can hop between LH2 complexes and then to LH1 and on to the reaction center for charge separation. The higher lying excitonic states observed in LH1 help to maximize spectral overlap with LH2, allowing for optimal energy transfer between the two antennae, while relaxation within LH1 from the higher lying states to the lower energy states minimizes back transfer into LH2. The spectral overlap that permits rapid transfer into the complex disappears as the higher-energy states relax, frustrating back transfer. The WT spectral dynamics are dominated by contributions from LH2 because the LH2 signal is stronger given our excitation spectrum and the high LH2:LH1 ratio in the WT strain (Figure 3.1). Due to the separation of timescales between intra- and inter-complex dynamics [41], we attribute the ultrafast dynamics observed in the LH1-only cells to the native behavior of this complex.

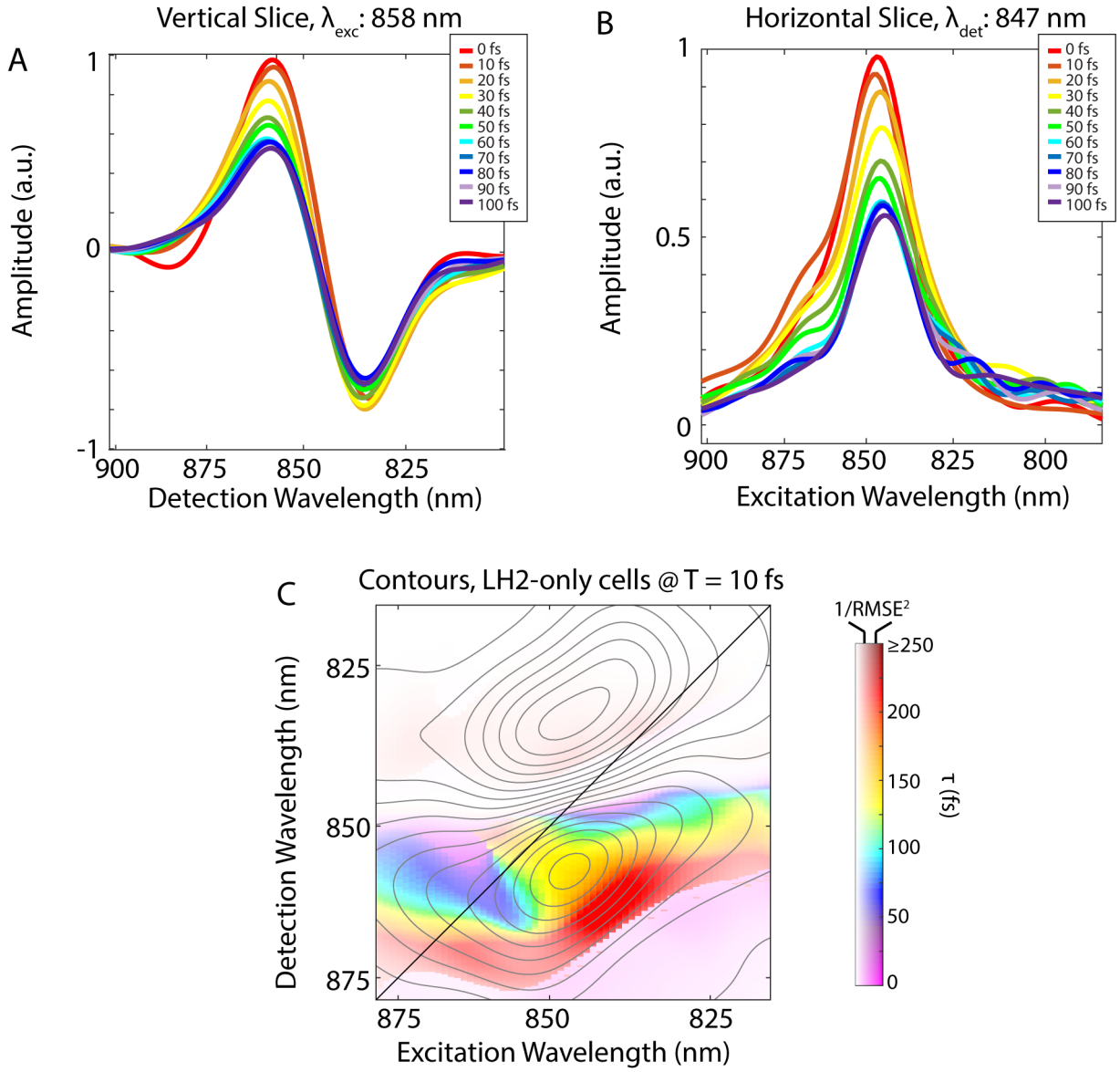

Figure 3.6: (A) The vertical slices through the B850 stimulated emission/ground state bleach feature in the LH2-only cells spectra. (B) The horizontal slice through the B850 stimulated emission/ground state bleach feature in the LH2-only cells spectra. (C) The decay time of a global fit of the LH2-only cells spectra to a single exponential (fit $= A\exp(-T/\tau) + B$) at each point in the 2D spectrum. Contrary to what we saw in the global fit the LH1-only cells data (Figure 3.5B), there is no loss of transition dipole strength on the red edge of B850 in the LH2-only cells data.

3.7 Experimental Methods

3.7.1 Growth and Isolation Protocols

The genomic deletions for the LH1-only and LH2-only cells were performed as described in Ref. [9]. LH1-only cells have the genotype Δ*puc1BA*/Δ*pufLMX* and, thus, lack LH2, the PufX membrane protein, and the reaction center. In WT cells, LH1 forms a dimeric complex around the RC which is facilitated by the PufX protein. In LH1-only cells, LH1 adopts a monomeric form. LH2-only cells have the genotype Δ*puc1BA*/Δ*2BA* and lack the entire LH1-RC-PufX complex. Wild-type and mutant cell strains were grown in the dark semi-aerobically at 30 °C. For 2DES measurements, cell cultures were centrifuged (Eppendorf 5810 R) at 4,000 rpm and the pellet was resuspended in a 50:50 (v:v%) mixture of glycerol and water. A 200 μm path length quartz flow cell (Starna Cells Inc.) was used during measurements. Living cultures were continually replenished from a 5 mL reservoir. For pump-probe spectroscopy measurements, membrane fragments of the LH1-only, LH2-only, and WT cells were used. Membranes were fragmented by disrupting them with a French press at 14,000 psi. After the disruption, the cells were centrifuged at 12,000 rpm (JA 30.STI) for 20 minutes in order to separate larger debris. The fragments were diluted to an optical density of $\sim$0.3 in the 200 μm pathlength flow cell using the absorption of B850 (for LH2-only and WT fragments) or B875 (for LH1-only fragments).

3.7.2 GRadient Assisted Photon Echo Spectroscopy (GRAPES) Experimental Details

The supercontinuum pulse used in these experiments was generated using the output of a 5 kHz Coherent Legend Elite USP regenerative amplifier seeded by a Coherent Micra Ti:Sapph oscillator focused into 2.25 m of argon gas held 4 psi above atmospheric pressure. The white-light resulting from filamentation in argon was then shaped and compressed to

15 fs FWHM, centered at 815 nm with 150 nm of bandwidth using a multiphoton intrapulse interference phase scan compressor (Biophotonics Solutions, Inc.). After compression, the pulse was divided into the four pulses needed to acquire the 2DES heterodyne signal. Pulses 1-3 were attenuated to 17.6 μJ/cm^2 (7.2×10^{13} photons/cm^2) at the sample, and pulse 4, the L.O., was attenuated by an additional two orders of magnitude and set to arrive 3 ps before the other pulses. The pulses were focused to a vertical line ($\sim$6 mm by $\sim$60 μm) at the sample and the GRAPES apparatus spatially encoded all coherence times between pulses 1 and 2 by tilting pulse 1 1.56° with respect to pulse 2. This led to a τ spacing of 0.91 fs/pixel (pixel size is 0.01 mm). A high-speed CMOS camera (Phantom Miro M, Vision Research) running at 50 Hz as a detector enabled collection of an entire 2DES spectrum with every laser shot every few seconds. A chopper is used so the camera collects signal + L.O. every second frame and otherwise collects L.O. and pulse 3 scatter (used for subtraction in data processing). Signal is thus collected at 25 Hz. High-speed collection permits extremely fine sampling of the waiting time domain, every 1 fs. The fine waiting time domain sampling allows for a significant reduction in contamination from scattered light. [29, 30] Live cells were flowed continuously through a 200 μm thick sample cell during measurement. For further details on the GRAPES instrument and methods for scatter removal during analysis, see Ref. [15].

3.8 Supplementary Figures

As a function of waiting time, the intensity of the 850 nm diagonal feature decays on a 100 fs timescale, which has been attributed to the relaxation to the lower lying B850 excited states and exciton migration around the LH2 B850 ring. [38, 42–44] The B800 feature decays on a $\sim$700 fs timescale, transferring energy to the B850 ring (Figure 3.8). The energy transfer from B800 to B850 results in the growth of an excited state absorption feature and a stimulated emission/ground state bleach feature that mirror the diagonal B850 features, but are centered

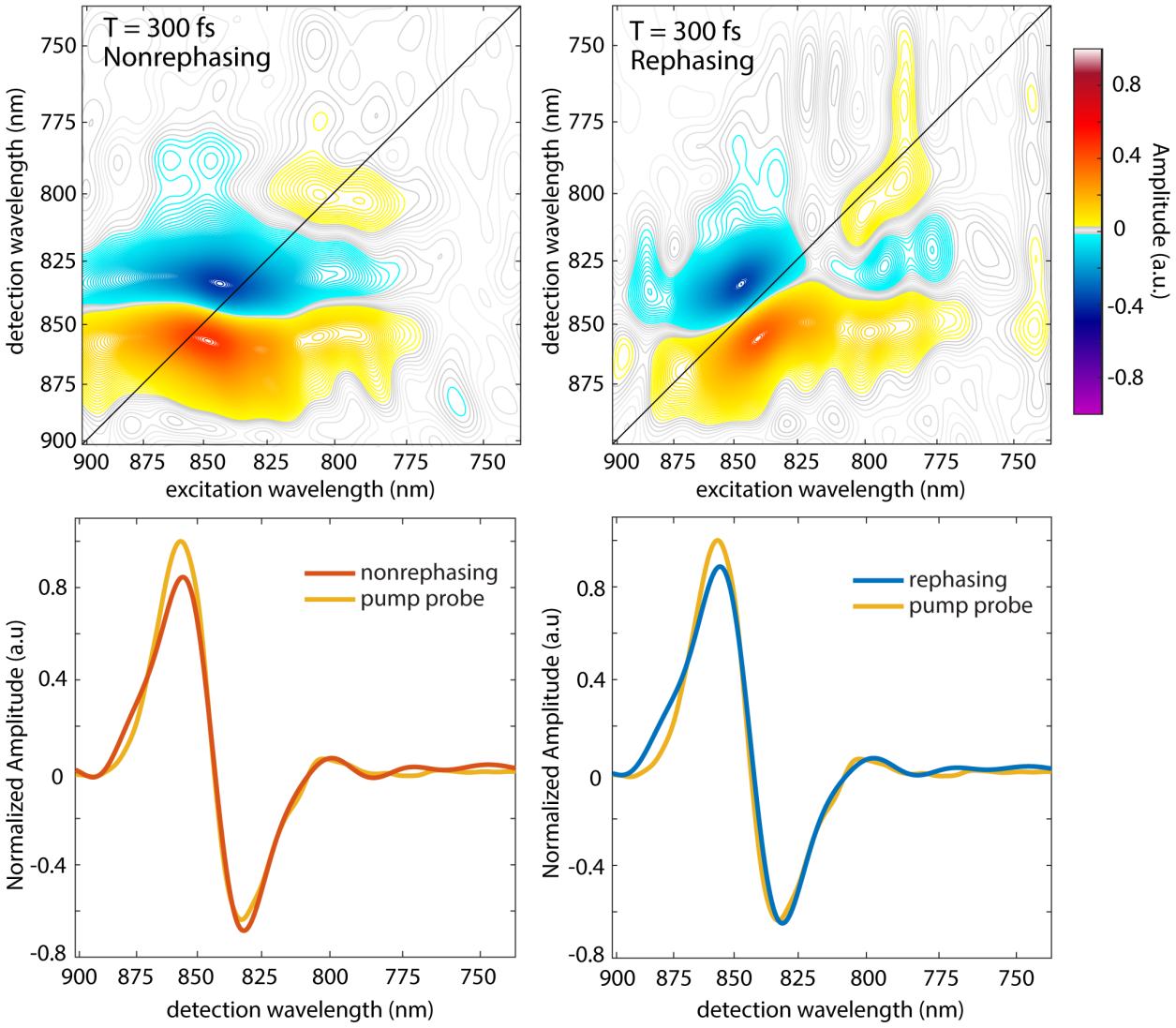

Figure 3.7: The phase of the 2DES signal is recovered according to the projection slice theorem, [17] which states that the projection of the real valued 2DES data across excitation wavelength should match the pump probe spectrum at the same waiting time. The nonrephasing (top left) and rephasing (top right) 2DES data are phased separately to the pump-probe data (bottom) by applying a constant, linear, and quadratic phase across both excitation and detection frequency domains. The sum of phased rephasing and nonrephasing data results in the absorptive lineshapes shown in Figure 3.3. The spectral lineshapes are artificially elongated in the diagonal or antidiagonal directions for rephasing and nonrephasing spectra, respectively. The rephasing and nonrephasing spectra alone are phase-twisted as a result of improper separation of absorptive and dispersive spectral components.

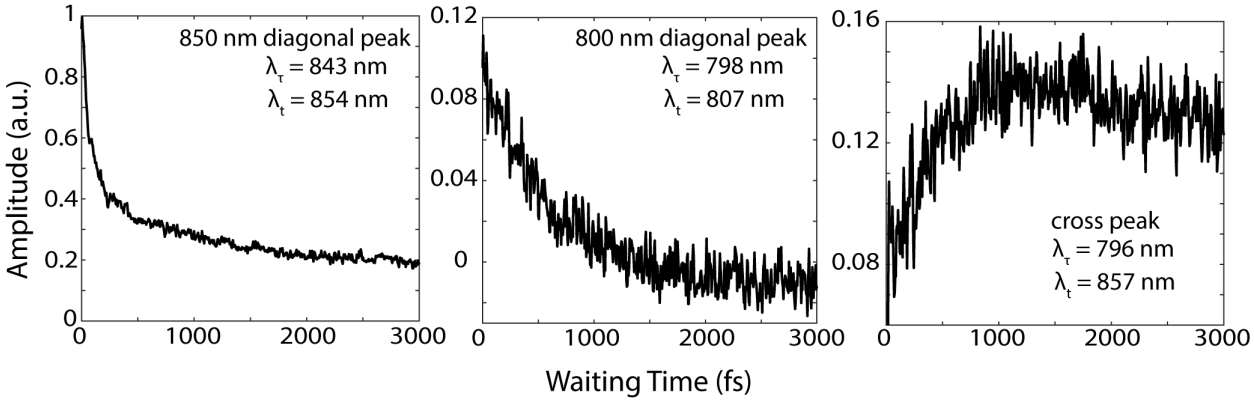

Figure 3.8: (Left) The decay of the B850 diagonal feature shows clear bi-exponential dynamics. The rapid decay is attributed to the relaxation to the lower lying B850 excited states and exciton hopping around the LH2 B850 ring. The slower decay is likely due to some amount of singlet-singlet annihilation present at these excitation powers. (Middle) The monoexponential decay of the B800 ring on the 700 fs timescale has been definitively assigned to energy transfer from B800 to B850. (Right) The growth of the cross peak associated with energy transfer from B800 to B850. The locations in the 2D spectra corresponding to the above waiting time traces are identified by their λ_τ (excitation wavelength) and λ_t (detection wavelength) coordinates.

on excitation wavelength (λ_τ) = 800 nm (Figure 3.3).

3.9 Conclusion

Our fully absorptive 2DES spectra of living *Rba. sphaeroides* cells reveal ultrafast exciton relaxation through a manifold of higher lying excited states in LH1. The intra-complex relaxation in our spectra is supported by previous reports of a dynamic red shift in LH1. This ultrafast relaxation and the rapid localization within LH1 indicate that the electronic structure of LH1 is effectively tuned for unidirectional energy transfer from LH2 to LH1. The ability to resolve ultrafast spectral dynamics within a broad manifold of excitonic states will enable the study of more complex energy transfer pathways in higher photosynthetic organisms.

REFERENCES

[1] S. H. Sohail, P. D. Dahlberg, M. A. Allodi, S. C. Massey, P. C. Ting, E. C. Martin, C. N. Hunter, and G. S. Engel. Communication: Broad manifold of excitonic states in light-harvesting complex 1 promotes efficient unidirectional energy transfer *in vivo*. *J Chem Phys*, 147(13):131101, 2017.

[2] Graham R. Fleming and Rienk van Grondelle. Femtosecond spectroscopy of photosynthetic light-harvesting systems. *Current Opinion in Structural Biology*, 7(5):738–748, 1997.

[3] Robert E. Blankenship. *Molecular Mechanisms of Photosynthesis*. John Wiley& Sons, Ltd, Chinchester, West Sussex, 2nd edition, 2014.

[4] M. Sener, J. Strumpfer, J. Hsin, D. Chandler, S. Scheuring, C. N. Hunter, and K. Schulten. Förster energy transfer theory as reflected in the structures of photosynthetic light-harvesting systems. *Chemphyschem*, 12(3):518–31, 2011.

[5] Herbert van Amerongen, Leonas Valkūnas, and Rienk van Grondelle. Photosynthetic excitons. 2000.

[6] Tobias Brixner, Jens Stenger, Harsha M. Vaswani, Minhaeng Cho, Robert E. Blankenship, and Graham R. Fleming. Two-dimensional spectroscopy of electronic couplings in photosynthesis. *Nature*, 434(7033):625–628, 2005.

[7] Gabriela S. Schlau-Cohen, Akihito Ishizaki, and Graham R. Fleming. Two-dimensional electronic spectroscopy and photosynthesis: Fundamentals and applications to photosynthetic light-harvesting. *Chemical Physics*, 386(1-3):1–22, 2011.

[8] J. Dostal, T. Mančal, R. Augulis, F. Vacha, J. Psencik, and D. Zigmantas. Two-dimensional electronic spectroscopy reveals ultrafast energy diffusion in chlorosomes. *J Am Chem Soc*, 134(28):11611–7, 2012.

[9] J. Dostal, J. Psencik, and D. Zigmantas. *In situ* mapping of the energy flow through the entire photosynthetic apparatus. *Nat Chem*, 8(7):705–10, 2016.

[10] Franklin D. Fuller, Jie Pan, Andrius Gelzinis, Vytautas Butkus, S. Seckin Senlik, Daniel E. Wilcox, Charles F. Yocum, Leonas Valkunas, Darius Abramavicius, and Jennifer P. Ogilvie. Vibronic coherence in oxygenic photosynthesis. *Nat Chem*, 6(8):706–711, 2014.

[11] Peter Hamm Zanni and Martin. *Concepts and methods of 2D infrared spectroscopy*. Cambridge University Press, New York, 2011.

[12] David M. Jonas. Two-dimensional femtosecond spectroscopy. *Annual Review of Physical Chemistry*, 54(1):425–463, 2003.

[13] Minhaeng Cho. Coherent two-dimensional optical spectroscopy. *Chemical Reviews*, 108(4):1331–1418, 2008.

[14] Franklin D. Fuller and Jennifer P. Ogilvie. Experimental implementations of two-dimensional fourier transform electronic spectroscopy. *Annual Review of Physical Chemistry*, 66(1):667–690, 2015.

[15] Peter D. Dahlberg, Andrew F. Fidler, Justin R. Caram, Phillip D. Long, and Gregory S. Engel. Energy transfer observed in live cells using two-dimensional electronic spectroscopy. *The Journal of Physical Chemistry Letters*, 4(21):3636–3640, 2013.

[16] Peter D. Dahlberg, Graham J. Norris, Cheng Wang, Subha Viswanathan, Ved P. Singh, and Gregory S. Engel. Communication: Coherences observed *in vivo* in photosynthetic bacteria using two-dimensional electronic spectroscopy. *The Journal of Chemical Physics*, 143(10):101101, 2015.

[17] V. P. Singh, A. F. Fidler, B. S. Rolczynski, and G. S. Engel. Independent phasing of rephasing and non-rephasing 2D electronic spectra. *The Journal of Chemical Physics*, 139(8):084201, 2013.

[18] Andrei Tokmakoff. Two-dimensional line shapes derived from coherent third-order nonlinear spectroscopy. *The Journal of Physical Chemistry A*, 104(18):4247–4255, 2000.

[19] Michaël L. Cartron, John D. Olsen, Melih Sener, Philip J. Jackson, Amanda A. Brindley, Pu Qian, Mark J. Dickman, Graham J. Leggett, Klaus Schulten, and C. Neil Hunter. Integration of energy and electron transfer processes in the photosynthetic membrane of *Rhodobacter sphaeroides*. *Biochimica et biophysica acta*, 1837(10):1769–1780, 2014.

[20] Peter D. Dahlberg, Po-Chieh Ting, Sara C. Massey, Marco A. Allodi, Elizabeth C. Martin, C. Neil Hunter, and Gregory S. Engel. Mapping the ultrafast flow of harvested solar energy in living photosynthetic cells. *Nature Communications*, 8(1):988, 2017.

[21] S Hess, M Chachisvilis, K Timpmann, M R Jones, G J Fowler, C N Hunter, and V Sundström. Temporally and spectrally resolved subpicosecond energy transfer within the peripheral antenna complex (LH2) and from LH2 to the core antenna complex in photosynthetic purple bacteria. *Proceedings of the National Academy of Sciences*, 92(26):12333–12337, 1995.

[22] Villy Sundström, Tõnu Pullerits, and Rienk van Grondelle. Photosynthetic light-harvesting: Reconciling dynamics and structure of purple bacterial LH2 reveals function of photosynthetic unit. *The Journal of Physical Chemistry B*, 103(13):2327–2346, 1999.

[23] Andy Freer, Steve Prince, Ken Sauer, Miroslav Papiz, Anna Hawthornthwaite Lawless, Gerry McDermott, Richard Cogdell, and Neil W. Isaacs. Pigment-pigment interactions and energy transfer in the antenna complex of the photosynthetic bacterium *Rhodopseudomonas acidophila*. *Structure*, 4(4):449–462, 1996.

[24] P. Qian, M. Z. Papiz, P. J. Jackson, A. A. Brindley, I. W. Ng, J. D. Olsen, M. J. Dickman, P. A. Bullough, and C. N. Hunter. Three-dimensional structure of the *Rhodobacter sphaeroides* RC-LH1-PufX complex: dimerization and quinone channels promoted by PufX. *Biochemistry*, 52(43):7575–85, 2013.

[25] M. Sener, J. Hsin, L. G. Trabuco, E. Villa, P. Qian, C. N. Hunter, and K. Schulten. Structural model and excitonic properties of the dimeric RC-LH1-PufX complex from *Rhodobacter sphaeroides*. *Chem Phys*, 357(1-3):188–197, 2009.

[26] Miroslav Z. Papiz, Steve M. Prince, Tina Howard, Richard J. Cogdell, and Neil W. Isaacs. The structure and thermal motion of the B800–850 LH2 complex from *Rps. acidophila* at 2.0 Å resolution and 100K: New structural features and functionally relevant motions. *Journal of Molecular Biology*, 326(5):1523–1538, 2003.

[27] John D. Hybl, Allison Albrecht Ferro, and David M. Jonas. Two-dimensional fourier transform electronic spectroscopy. *The Journal of Chemical Physics*, 115(14):6606–6622, 2001.

[28] M. L. Cowan, J. P. Ogilvie, and R. J. D. Miller. Two-dimensional spectroscopy using diffractive optics based phased-locked photon echoes. *Chemical Physics Letters*, 386(1–3):184–189, 2004.

[29] Elad Harel, Andrew F. Fidler, and Gregory S. Engel. Single-shot gradient-assisted photon echo electronic spectroscopy. *The Journal of Physical Chemistry A*, 115(16):3787–3796, 2011.

[30] Elad Harel, Andrew F. Fidler, and Gregory S. Engel. Real-time mapping of electronic structure with single-shot two-dimensional electronic spectroscopy. *Proceedings of the National Academy of Sciences*, 107(38):16444–16447, 2010.

[31] Peter D. Dahlberg, Po-Chieh Ting, Sara C. Massey, Elizabeth C. Martin, C. Neil Hunter, and Gregory S. Engel. Electronic structure and dynamics of higher-lying excited states in light harvesting complex 1 from *Rhodobacter sphaeroides*. *The Journal of Physical Chemistry A*, 120(24):4124–4130, 2016.

[32] Vladimir Novoderezhkin, Markus Wendling, and Rienk van Grondelle. Intra- and interband transfers in the B800-B850 antenna of *Rhodospirillum molischianum*: Redfield theory modeling of polarized pump-probe kinetics. *The Journal of Physical Chemistry B*, 107(41):11534–11548, 2003.

[33] J. D. Eaves, J. J. Loparo, C. J. Fecko, S. T. Roberts, A. Tokmakoff, and P. L. Geissler. Hydrogen bonds in liquid water are broken only fleetingly. *Proceedings of the National Academy of Sciences of the United States of America*, 102(37):13019–13022, 2005.

[34] Sean T. Roberts, Joseph J. Loparo, and Andrei Tokmakoff. Characterization of spectral diffusion from two-dimensional line shapes. *The Journal of Chemical Physics*, 125(8):084502, 2006.

[35] Randy D. Mehlenbacher, Jialiang Wang, Nicholas M. Kearns, Matthew J. Shea, Jessica T. Flach, Thomas J. McDonough, Meng-Yin Wu, Michael S. Arnold, and Martin T. Zanni. Ultrafast exciton hopping observed in bare semiconducting carbon nanotube thin films with two-dimensional white-light spectroscopy. *The Journal of Physical Chemistry Letters*, 7(11):2024–2031, 2016.

[36] René Monshouwer, Malin Abrahamsson, Frank van Mourik, and Rienk van Grondelle. Superradiance and exciton delocalization in bacterial photosynthetic light-harvesting systems. *The Journal of Physical Chemistry B*, 101(37):7241–7248, 1997.

[37] L. D. Book, A. E. Ostafin, N. Ponomarenko, J. R. Norris, and N. F. Scherer. Exciton delocalization and initial dephasing dynamics of purple bacterial LH2. *The Journal of Physical Chemistry B*, 104(34):8295–8307, 2000.

[38] Ralph Jimenez, Frank van Mourik, Jae Young Yu, and Graham R. Fleming. Three-pulse photon echo measurements on LH1 and LH2 complexes of *Rhodobacter sphaeroides*: A nonlinear spectroscopic probe of energy transfer. *The Journal of Physical Chemistry B*, 101(37):7350–7359, 1997.

[39] René Monshouwer, Andrius Baltuška, Frank van Mourik, and Rienk van Grondelle. Time-resolved absorption difference spectroscopy of the LH-1 antenna of *Rhodopseudomonas viridis*. *The Journal of Physical Chemistry A*, 102(23):4360–4371, 1998.

[40] Rienk van Grondelle and Vladimir I. Novoderezhkin. Energy transfer in photosynthesis: experimental insights and quantitative models. *Physical Chemistry Chemical Physics*, 8(7):793–807, 2006.

[41] V. Nagarajan and W. W. Parson. Excitation energy transfer between the B850 and B875 antenna complexes of *Rhodobacter sphaeroides*. *Biochemistry*, 36(8):2300–2306, 1997.

[42] V. I. Novoderezhkin, J. P. Dekker, and R. van Grondelle. Mixing of exciton and charge-transfer states in Photosystem II reaction centers: modeling of Stark spectra with modified Redfield theory. *Biophys J*, 93(4):1293–311, 2007.

[43] Andrew F. Fidler, Ved P. Singh, Phillip D. Long, Peter D. Dahlberg, and Gregory S. Engel. Dynamic localization of electronic excitation in photosynthetic complexes revealed with chiral two-dimensional spectroscopy. *Nature Communications*, 5:3286, 2014.

[44] A. F. Fidler, V. P. Singh, P. D. Long, P. D. Dahlberg, and G. S. Engel. Timescales of coherent dynamics in the light harvesting complex 2 (LH2) of *Rhodobacter sphaeroides*. *J Phys Chem Lett*, 4(9):1404–1409, 2013.

CHAPTER 4

DNA SCAFFOLD SUPPORTS LONG-LIVED VIBRONIC COHERENCE IN AN INDODICARBOCYANINE (CY5) DIMER

Vibronic coupling between pigment molecules is believed prolong coherences in photosynthetic pigment-protein complexes. Reproducing long-lived coherences using vibronically coupled chromophores in synthetic DNA constructs presents a biomimetic route to efficient artificial light harvesting. Here, we present two-dimensional (2D) electronic spectra of one monomeric Cy5 construct and two dimeric Cy5 constructs (0 bp and 1 bp between dyes) on a DNA scaffold and perform beating frequency analysis to interpret observed coherences. Power spectra of quantum beating signals of the dimers reveal high frequency oscillations that correspond to coherences between vibronic exciton states. Beating frequency maps confirm that these oscillations, 1270 cm^{-1} and 1545 cm^{-1} for the 0 bp dimer and 1100 cm^{-1} for the 1 bp dimer, are coherences between vibronic exciton states. We use a vibronic exciton model to determine the excitonic coupling between the dyes in the dimers and calculate the linear absorption spectra of the dye-DNA constructs. Energy spacing between the states calculated by the model corresponds to the beating frequencies observed in the 2D spectra. These coherences persist on the timescale of hundreds of femtoseconds and establish DNA as an attractive scaffold for synthetic light harvesting applications.

4.1 Background on Vibronic Coherence in Biological and Synthetic Systems

Prolonged quantum coherences of vibronic (mixed electronic and vibrational) origin have been observed in pigment-protein complexes from multiple photosynthetic organisms [1–8], suggesting that these long-lived coherences may be a universal design principle for effective

photosynthesis. Vibronic coupling, coupling between an underdamped vibrational mode and the electronic excited state, is believed to be responsible not only for this longer coherence lifetime [1, 9–11], but also for the high fidelity energy transfer seen in natural light harvesting systems [9, 11]. The mechanisms through which molecular systems sustain vibronic coherences could offer synthetic strategies for light harvesting.

In photosynthetic pigment-protein complexes, the decay, or dephasing, of quantum coherences is dependent on the coupling between the chromophores and on the surrounding protein scaffold. [12] This chromophore-protein relationship is also integral to exciton energy transfer. [13] When designing biomimetic molecular systems with light harvesting abilities, developing long-range molecular architecture that can mimic the role of the protein in native systems is of utmost importance. Molecular systems may exhibit steady-state spectroscopic signatures of mixing between vibrational and electronic states, but quantum superposition between these states may dephase within 10s of femtoseconds. Dephasing on this timescale would not promote energy transfer occurring on the hundreds of femtosecond to picosecond timescale. In previous studies on vibronic coherences in molecular systems, prolonged vibronic coherences were only observed when strict order was imposed on the chromophores, either through molecular design [14] or an external scaffold [15]. These studies point to the importance of macroscopic structure in sustaining coherences.

From a synthetic standpoint, DNA is an attractive scaffold for biomimetic light harvesting. Unlike the complex folding mechanisms exhibited by proteins, DNA assembly is predictable and programmable. Organic dyes constrained by DNA scaffolds in multiple geometries have been used to create controllable energy transfer pathways [16–20] but designing vibronic coherence into these structures has not yet been explored. To excite quantum superpositions of states with the potential for slow dephasing, exciton delocalization (observable in spectroscopic signatures) is required. A recent study [21] reported that the absorption spectra of organic dyes at single digit base pair separations along a DNA scaffold show

marked differences compared with the spectra of the constituent monomer due to exciton delocalization, indicating that the multiple-dye constructs are molecular aggregates [22]. Aggregate constructs in different geometries have been shown to support long-lived vibronic coherence. [14, 23] Conversely, covalent dimers of organic dyes in which there is no analog to the protein scaffold have only been able to support vibronic coherences on timescales much faster than the timescale of energy transfer for light harvesting. [10] If a DNA scaffold can sustain vibronic coherence, DNA-dye constructs may provide a path to highly efficient artificial light harvesting.

To investigate if DNA scaffolds can prolong vibronic coherence, we use ultrafast two-dimensional electronic spectroscopy (2DES). 2DES can elucidate energy transfer pathways and dynamics and couplings between chromophores [2, 8, 24–27]. The femtosecond resolution of this technique enables the visualization of excited superpositions of quantum states as time-dependent spectral oscillations. These quantum coherences can arise from any pair of non-degenerate electronic, vibrational, or vibronic states, and pinpointing the precise physical origin of the coherence is non-trivial [28–30]. Careful design of molecular constructs and knowledge of their electronic, vibrational, and vibronic structure can facilitate identification of the origin of observed spectral oscillations.

In the current study, we use three DNA-dye constructs to determine whether DNA can support long-lived coherence between the vibronic states of indodicarbocyanine (Cy5) dimers. We explore the role of excitonic coupling between the dyes in supporting coherence by varying their relative spacing along the DNA scaffold. We use 2DES to examine how quantum beating signals (vibrational and vibronic coherences) change with excitonic coupling strength and how long they persist before dephasing. We pair our ultrafast spectroscopic studies with a vibronic exciton model to better assign the origin of the observed coherences.

4.2 Design of DNA-Dye Consructs and their Linear Spectral Signatures

Our DNA-dye constructs were designed such that the only difference between our monomer control sample and two dimer samples is the excitonic coupling strength between the dyes (Figure 4.2). The organic cyanine5 (Cy5) dye is used for all constructs; therefore, the vibrational and electronic states are universal. By varying the excitonic coupling strength between the dyes, the mixing between the electronic and vibrational states changes and gives rise to different vibronic states and different degrees of vibronic exciton delocalization. Unlike proteins in photosynthetic pigment-protein complexes which hold chromophores in a fixed spatial configuration non-covalently, the coupled Cy5 dyes were covalently attached to the DNA scaffold through a double phosphate attachment. This attachment chemistry, achieved during DNA synthesis, promotes dye localization and greater certainty of absolute dye position. [17, 31]. The monomer construct consists of a Cy5 dye replacing a single adenine in the middle of an 18 base pair double-stranded DNA (dsDNA) segment. The dimeric constructs consist of the same dsDNA segment but with two base pairs replaced with Cy5 dyes on opposite backbones of the double helix. The 1 bp dimer has the Cy5 dyes attached to each backbone chain at a vertical separation of one base pair. The 0 bp dimer has the Cy5 dyes attached to each backbone chain replacing a complete pair of nucleotides. This zero base pair separation represents the closest dye proximity, and therefore the strongest excitonic coupling, for the chosen attachment chemistry. A molecular representation of the Cy5 dyes attached to the DNA scaffold for the 0 bp construct is shown in Figure 4.1.

All Cy5 dyes are flanked by either an adenine of thymine on one side and by a guanine or cytosine on the other. Hydrogen bonding strength of the flanking base pairs affects the nature of the molecular dimer formed (relative weighting of H- and J-like components) [21]. Keeping the DNA sequence as conserved as possible across the constructs mitigates the influence of the flanking base pairs on our results. The role of the DNA sequence in vibronic

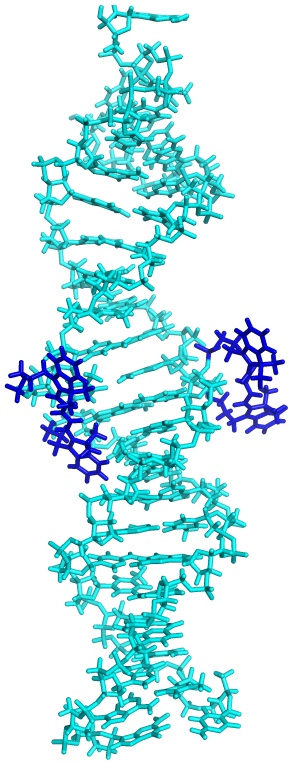

Figure 4.1: A molecular representation of the 0 bp dimeric construct. The DNA scaffold is shown in cyan and the two Cy5 dyes are shown in blue.

coherence is another interesting area to explore but is outside the scope of this work.

The UV/vis absorption spectra for the monomer, 1 bp dimer, and 0 bp dimer constructs are presented in Figure 4.2 (red curves) and provide insight into the vibronic structures. As expected for molecular aggregates, the spectra of the dimeric constructs show large deviations from the monomeric spectral signature. The linear absorption spectrum for the Cy5 monomer construct exhibits a prominent absorption feature around 15,300 cm^{-1}, which we will refer to as the 0-0 transition. The higher energy absorption band, around 16,500 cm^{-1}, which will be referred to as the 0-1 transition, is a vibronic sub-band typical of cyanine dyes [32]. The higher energy vibronic sub-band arises due to an active 1200 cm^{-1} vibrational mode on the electronic excited state which has been previously assigned to a C-C stretch of the polymethine backbone of the Cy5 dye. [32]

The 1 bp dimer absorption spectrum shows little shift in the 0-0 peak maximum compared with the monomer spectrum, though the lineshape is considerably broadened and there is a significant enhancement in the oscillator strength of the 0-1 feature. The 0-1 feature is also slightly blue shifted in the 1 bp dimer spectrum, with a central frequency near 16,700 cm^{-1}. The 0 bp dimer absorption spectrum shows further deviation from the monomer spectral signature. The maximum absorption of the 0-0 transition feature is red shifted considerably compared to the monomer and 1 bp dimer spectra. Additionally, the 0-0 feature in the 0 bp dimer spectrum is bi-modal with a slightly more intense peak centered around 15,000 cm^{-1} and a slightly less intense peak around 15,500 cm^{-1}. The 0-1 feature in the 0-bp dimer spectrum is more blue shifted and more intense than that in the 1 bp dimer spectrum.

This red shift of the 0-0 transition in the 0 bp dimer spectrum and coincident blue shift and intensity enhancement in 0-1 absorption has been reported previously in homo- and hetero-dimers of cyanine dyes [10, 17, 33, 34]. Neither H- nor J-like coupling can fully explain these spectral changes as a function of dye separation. H-type coupling occurs when the transition dipoles of the dyes are oriented parallel to each other while J-type coupling

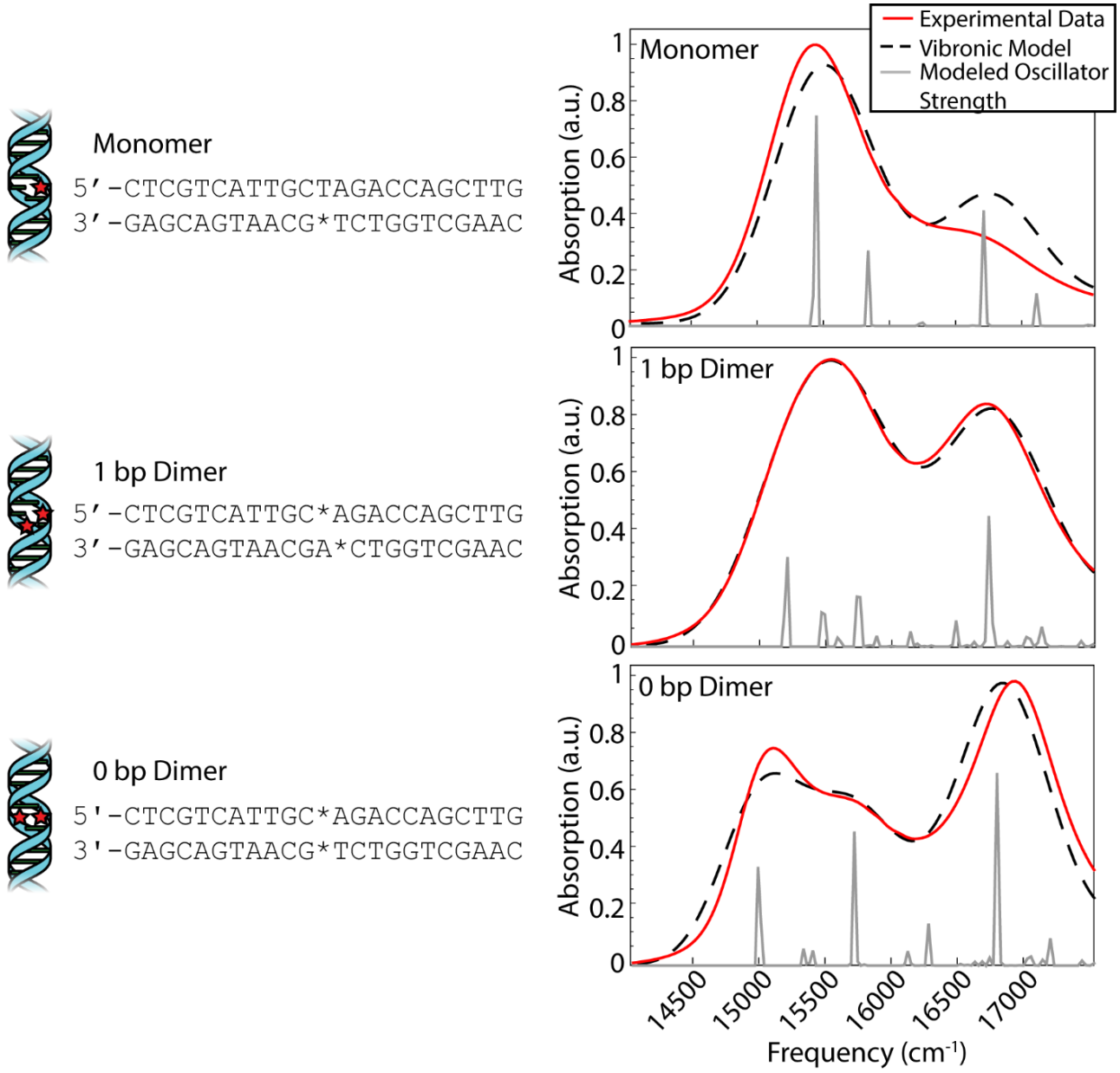

Figure 4.2: The dsDNA sequence of the three constructs studied. In both the cartoon representations of the constructs and the sequences Cy5 positions are denoted with stars. To the right of each sequence is a comparison of the modeled linear absorption spectra (black dashed) calculated using the vibronic exciton model and the experimental linear absorption spectra (red) for monomer (top), 1bp dimer (middle), and 0bp dimer (bottom). The gray lines show the modeled oscillator strength of vibronic states calculated by diagonalizing the vibronic exciton Hamiltonian.

occurs when the transition dipoles of the dyes are oriented head-to-tail. [35] The splitting seen in the 0-0 peak of the 0 bp dimer spectrum is due to Davydov splitting, a mixing of H- and J-like optical properties. Similar to H- and J-like spectral signatures, Davydov splitting is another optical manifestation of exciton delocalization. [36] We observe increased Davydov splitting when the dyes are held in closest proximity, indicative of significant delocalization between the dyes. The higher energy feature in the 0 bp dimer 0-0 transition is due to H-like coupling between the dyes and the lower energy 0-0 feature is due to J-like coupling. These steady-state spectral deviations from the monomeric spectral signature are a result of strong excitonic interactions between vibronic states.

4.3 Vibronic Exciton Model

Vibronic-exciton theory can explain the Davydov splitting of the 0-0 feature and the enhanced intensity of the 0-1 feature seen in the linear absorption spectra of the 1 bp and 0 bp dimers. [22, 37] Calculating the vibronic states in our DNA-dye constructs will enable interpretation of the physical origin of any observed spectral oscillations in our upcoming 2DES experiments. If observed spectral oscillations do not match the energetic gap between vibronic states, they are more likely of vibrational origin.

4.3.1 Theoretical Details of the Vibronic Exciton Model

We use the theoretical framework set forth by K$'$uhn, Renger, and May [22, 37, 38] and previously applied to a Cy3 dimers on a DNA scaffold [21] to reproduce the linear absorption spectra of the Cy5 monomer, 1bp Cy5 dimer, and 0 bp Cy5 dimer. Based on the Born-Oppenheimer approximation, the electronic and vibrational contributions to the vibronic wavefunctions are separable. We define a local vibronic basis which consists of monomer A in an electronic excited state and monomer B in the electronic ground state with an additional harmonic oscillator vibrational basis defined for the electronic ground state for

each relevant vibrational mode. The diagonal elements of the Hamiltonian matrix are given by,

$$E^A_{j,k} = \langle e_A, j|\langle g_B, k|H|e_A, j\rangle|g_B, k\rangle \tag{4.1}$$

where the superscript A denotes that monomer A is in the electronic excited state (e), j is the vibrational level in the electronic excited state of monomer A, and k is the vibrational level of monomer B in its electronic ground state (g). The off-diagonal elements of the Hamiltonian are given by,

$$V^{AB}_{ij,kl} = \langle e_A, j|\langle g_B, k|H|e_B, l\rangle|g_A, i\rangle \tag{4.2}$$

where i and j are the vibrational levels of monomer A in its ground (g) and excited (e) states, respectively and k and l are the vibrational levels of monomer B in its ground (g) and excites (e) states, respectively. If one vibrational quantum for a single vibrational mode is considered for each monomer on both the ground and excited electronic states, the Hamiltonian is

$$H = \begin{bmatrix} E^A_{0,0} & 0 & 0 & 0 & V^{AB}_{00,00} & V^{AB}_{10,00} & V^{AB}_{00,01} & V^{AB}_{10,01} \\ 0 & E^A_{0,1} & 0 & 0 & V^{AB}_{00,10} & V^{AB}_{10,10} & V^{AB}_{00,11} & V^{AB}_{10,11} \\ 0 & 0 & E^A_{1,0} & 0 & V^{AB}_{01,00} & V^{AB}_{11,00} & V^{AB}_{01,01} & V^{AB}_{11,01} \\ 0 & 0 & 0 & E^A_{1,1} & V^{AB}_{01,10} & V^{AB}_{11,10} & V^{AB}_{01,11} & V^{AB}_{11,11} \\ V^{BA}_{00,00} & V^{BA}_{10,00} & V^{BA}_{00,01} & V^{BA}_{10,01} & E^B_{0,0} & 0 & 0 & 0 \\ V^{BA}_{00,10} & V^{BA}_{10,10} & V^{BA}_{10,11} & V^{BA}_{01,11} & 0 & E^B_{0,1} & 0 & 0 \\ V^{BA}_{01,00} & V^{BA}_{11,00} & V^{BA}_{01,01} & V^{BA}_{11,01} & 0 & 0 & E^B_{1,0} & 0 \\ V^{BA}_{01,10} & V^{BA}_{11,10} & V^{BA}_{01,11} & V^{BA}_{11,11} & 0 & 0 & 0 & E^B_{1,1} \end{bmatrix} \tag{4.3}$$

Vibronic exciton theory, as applied in this case, will be equivalent to multimode theory of Franck-Condon progressions for the case of the monomer. [37] Vibronic exciton theory will

yield different Franck-Condon progression for the dimers due to Coulomb interactions. The theory requires accounting for vibrationally excited states on the monomer in its electronic ground state though the population of these states are negligible at room temperature. [37] Thus in equation 3, columns two, four, six, and eight of the Hamiltonian matrix carry no oscillator strength.

This theoretical framework can be easily extended to incorporate more than one vibrational mode each having multiple accessible vibrational quanta. In the present work, to reproduce the linear absorption spectra, two vibrational modes were used with two vibrational quanta considered for the higher frequency mode and three vibrational quanta considered for the lower frequency mode. The number of vibrational quanta were chosen to ensure coverage of the bandwidth of absorption for these constructs. Equation 4.8 was used to simulate the absorption spectra for the monomer, 1 bp dimer, and 0 bp dimer constructs. The resulting Hamiltonian was a 288 x 288 matrix. The energies of the vibronic states are

$$E^{A}_{j,k} = E_0 + (j+k) * h\nu_{vib_1} + (m+n) * h\nu_{vib_2} \tag{4.4}$$

where E_0 is the 0-0 tranistion energy, h is Planck's constant, and ν_{vib_1} and $\nu_{vib_2)}$ are the frequencies of the two vibrational modes incorporated into the model. The off-diagonal Hamiltonian matrix elements are given by,

$$V^{AB}_{ij,k} = J\langle g_A, i|e_A, j\rangle\langle g_B, k|e_B, l\rangle e^{\pm i\phi} \tag{4.5}$$

where J is the electronic coupling strength and ϕ is a phase factor carrying information on the relative orientation between the transition dipoles within a dimer. The Franck-Condon factors are incorporated into these off-diagonal elements and are defined in terms of the Huang-Rhys factors, S, as

$$\langle g_A, i|e_A, j\rangle = e^{-S/2}\sum_{k=0}^{i}\sum_{l=0}^{j}\frac{-1^l\sqrt{S}^{k+l}}{k!l!}\sqrt{\frac{i!j!}{(i-k)!(j-l)!}}\delta(i-k, j-l) \tag{4.6}$$

The Huang-Rhys factor is a dimensionless parameter related to the mean square displacement of a displaced harmonic oscillator. Physically, it represents the coupling strength between the electronic states and the nuclear degrees of freedom.

Numerical diagonalization of the Hamiltonian allows us to write the one-exciton wavefunctions, ψ_κ, where there are κ eigenvalues. The oscillator strengths of the vibronic transitions are given by,

$$O_{\psi_\kappa} = |\langle\psi_\kappa|\mu|\psi_0\rangle|^2 \tag{4.7}$$

where μ is the dipole operator. The linear absorbance spectrum is reproduced by weighting each transition energy by its calculated oscillator strength and applying a Gaussian linewidth to the transition:

$$A(\nu) = A\sum_k \frac{|\langle\psi_\kappa|\mu|\psi_0\rangle|^2}{\sqrt{2\pi\gamma}}\exp(-\frac{(\nu - E_\kappa^2)}{2\gamma^2}) \tag{4.8}$$

In Equation 4.8, A is an amplitude factor and γ is the Gaussian linewidth.

4.3.2 Calculation of Linear Absorption Spectra for DNA-Dye Constructs Using Vibronic Exciton Model

Spectra were calculated by optimizing the fit produced by the model to the experimental linear absorption spectra. Figure 4.2 (dashed black) shows the resultant calculated linear absorption spectra. The 0-0 transition energy, the frequencies of the two incorporated vibrational modes and their corresponding Huang-Ryhs factors are parameters that should be shared across the monomer and dimer constructs and as such were applied to all three

constructs. One of the included vibrational modes (1270 cm^{-1}) was held as a fixed variable during our modeling. This frequency was chosen based on the energy gap between the 0-0 and 0-1 features in the monomer construct as seen in the linear absorption spectra. The frequency of the second vibrational mode, the Huang-Rhys factors for both modes and the 0-0 transition energy were minimized by our fitting procedure. This global minimization assures values that simultaneously best reproduce the absorption spectra for all three constructs. The electronic coupling strength, J, and orientational factor, ϕ, were set to zero for the monomer but were optimized independently for each of the dimers.

Each vibronic state carrying oscillator strength for a given construct was fit with the same Gaussian linewidth. While the linewidths of these states are likely different from each other, using a single linewidth prevents our optimization algorithm from using widely varying linewidths to produce slightly better fits to the experimental absorption data, which can result in unphysical linewidth values. It is physical to have different linewidths for each of the three samples because increased delocalization leads to line narrowing due to environmental interactions [39]. All parameters were optimized simultaneously for all three constructs to produce the best overall fit to three experimental linear absorption spectra. Table 4.3.2 contains the values of all the parameters calculated using the vibronic exciton model.

The calculated stick spectra (gray lines in Figure 4.2) show the energies of the mixed electronic-vibrational states in the dye-DNA constructs. The vibronic states calculated for the constructs result from mixing between their electronic and vibrational energy levels. We calculate multiple vibronic states under the 0-0 transition features for both dimeric constructs, indicating that the model captures the splitting of the 0-0 feature as a result of the coupling between the dyes in the 0 bp dimer spectrum.

	E_{0-0} (cm^{-1})	E_{ω_1} (cm^{-1})	E_{ω_2} (cm^{-1})	S_1	S_2	J (cm^{-1})	γ (cm^{-1})	A	ϕ
Monomer	15401	1270	397	0.447	0.251	0	350	0.046	N/A
1 bp Dimer	15401	1270	397	0.447	0.251	356	357	0.068	0.58
0 bp Dimer	15401	1270	397	0.447	0.251	611	301	0.064	0.62

Table 4.1: Fit Parameters from Vibronic Exciton Model
Parameters calculated from the vibronic exciton model used to reproduce the linear absorption spectra (Figure 1) for the monomer and dimer samples. E_{0-0} (0-0 transition energy), E_{ω_2}(energy of second vibrational mode), S_1 (Huang-Rhys factor for first vibrational mode), S_2 (Huang-Rhys factor for second vibrational mode) were minimized in order to find the best values to fit the experimental data for all three constructs simultaneously. E_{ω_1} (energy of first vibrational mode) was held fixed at 1270 cm^{-1}. All other parameters, J (electronic coupling), γ (Gaussian linewidth), A (amplitude factor), and ϕ (phase factor) were minimized for each sample.

4.4 Two-Dimensional Electronic Spectroscopy of DNA-dye Constructs

We use 2DES to interrogate whether the DNA scaffold can support coherent superposition between the vibronic states calculated by the vibronic exciton model. 2DES is a four wave mixing technique that probes frequency-frequency correlations as a function time and in doing so can report on electronic coupling between chromophores, energy transfer pathways, and ultrafast coherent dynamics (see Experimental Methods). [25, 40, 41] An absorptive 2D spectra for each of the three DNA-dye constructs at T = 250 fs is presented in Figure 4.3. The spectra for all three constructs show a prominent positive diagonal feature near 15,000 cm^{-1} and above and below diagonal cross peaks (both positive) corresponding to coupling between the 0-0 ($\sim$15,000 cm^{-1}) and 0-1 ($\sim$16,600 cm^{-1}) transitions. Positive features in our 2DES spectra correspond to ground state bleach (GSB) or stimulated emission (SE) signals. An upper diagonal feature near 16,700 cm^{-1} from the 0-1 transition appears in the spectra for the dimeric constructs but is absent in the monomer spectra. The 0-1 transition carries less oscillator strength than the 0-0 and is excited and detected by significantly less intense light (Figure 4.10) which explains the absence of an upper diagonal feature in the monomer spectra.

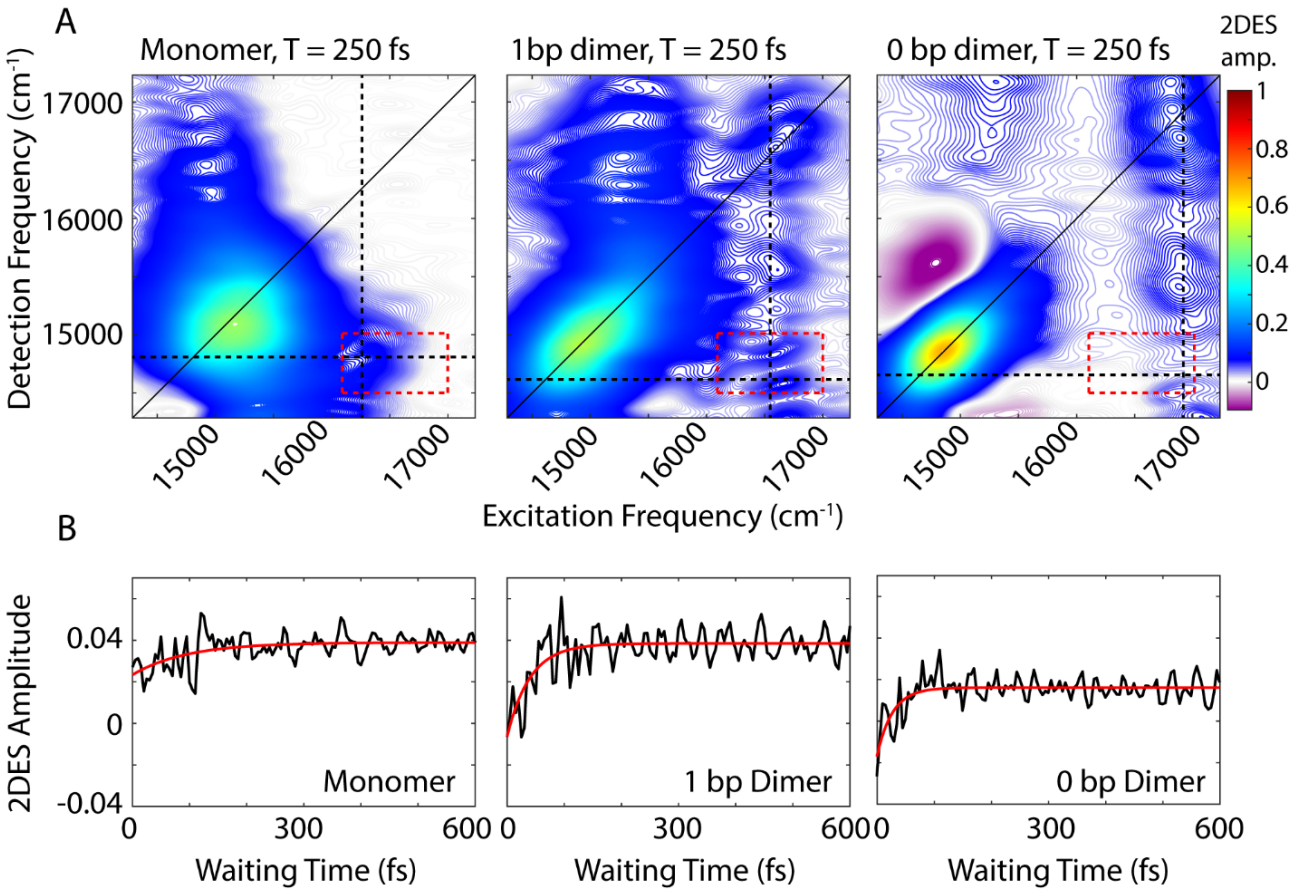

Figure 4.3: (A) Absorptive 2DES spectra of monomer (left), 1 bp dimer (center), and 0 bp dimer (right) constructs at a waiting time of 250 fs. The black dashed lines indicate the approximate spectral location of the 0-0 transition in detection frequency and 0-1 transition in excitation frequency. All points contained within the dashed red box are used to generate the power spectra in Figure 4. (B) 2DES signal as a function of waiting time (T) from the below diagonal cross peak location at the intersection of the dashed lines in A. Monoexponential fits to the time traces are shown in red.

The 0 bp dimer spectrum has an intense negative feature slightly above the diagonal at excitation frequency 14,900 cm^{-1}, detection frequency 15,500 cm^{-1}, corresponding to an excited state absorption (ESA) signal. There is likely an ESA signal at this above diagonal location in the monomer and 1 bp dimer spectra, but due to cancellation with stronger positive signals, it is obscured. With increasing excitonic coupling strength in the 0 bp dimer, the ESA pathway at this spectral location dominates because the change in electronic coupling alters the oscillator strength of different transitions.

The dynamics of the below diagonal cross peak provides insight into the nature of the coupling and energy transfer between the higher and lower energy states in the three constructs. We fit the growth of the below diagonal cross peak signal to monoexponential decays (Figure 4.3B). In all three constructs, the below diagonal cross peak grows in on a sub-100 fs timescale ($\tau_{monomer}$ = 95 fs, τ_{1bp} = 40 fs, τ_{0bp} = 26 fs). The fast time constants associated with these signals suggest an ultrafast delocalization of an initially more localized excitation. The correlation between delocalization dynamics and excitonic coupling strength follows from the degree of Davydov splitting in the linear absorption spectra. That is, we see the fastest delocalization (growth of the below diagonal cross peak) in the 0 bp dimer spectra which shows the most Davydov splitting.

The location of the below diagonal cross peak for all three constructs appears at a lower detection frequency ($<$ 15,000 cm^{-1}) than would be expected based on the linear absorption. We attribute the location of this feature to our laser spectrum (which is much more intense at redder wavelengths, see Figure 4.10) and relaxation to a Stokes-shifted fluorescence state. Previous 2DES experiments on cyanine dimers show this below diagonal cross peak in a similarly red-shifted spectral location. [10]

In addition to the population dynamics contained in the time traces in Figure 4.3B, the time traces all show significant oscillations. We use the oscillations to report on coherence evolution during the waiting time and assign observed frequencies to physical mechanisms.

Differences in observed coherent oscillations at this spectral location may contribute to the increasingly fast growth of the cross peak as a function of excitonic coupling between the dyes.

4.5 Beating Frequency Analysis of DNA-Dye Constructs

The coherences in our 2D spectra are either superpositions between vibrational levels or vibronic exciton states. Our constructs do not possess any purely electronic coherences since the electronic excited states are all non-trivially mixed with vibrational modes. Fourier transforming over the waiting time tells us the frequencies and intensities of the oscillations. In photosynthetic systems, conservation of vibronic coherences is optimized when the vibrational quantum mixed with the electronic excited state is resonant with the splitting between electronic energies. [1] This resonance criterion complicates the distinction between vibrational and vibronic coherences as there can be intense quantum beating signals from vibrational wavepackets on the ground electronic state. These oscillations may be widespread in the 2D spectrum. [10] By breaking down our absorptive 2DES spectra into their rephasing and nonrephasing components, we can more easily distinguish between ground state vibrational and vibronic beating signals. [30, 41–43] Rephasing and nonrephasing 2D spectra are shown in Figure 4.11. The nonrephasing spectra for all three constructs contain a strong ESA feature (negative) at the below diagonal cross peak location. Because the nonrephasing signal is dominated by ESA, it is most likely that observed coherences are on the excited state, though they may be vibrational or vibronic in origin. Previous calculations performed for a molecular biscyanine dimer [10] determined that nonrephasing pathways predominantly support ground state coherences on or near the diagonal for a similar construct, indicating that nonrephasing coherences at cross peak locations likely involve vibronic exciton (excited) states.

Figure 4.5A shows the below diagonal cross peak dynamics of the rephasing and non-

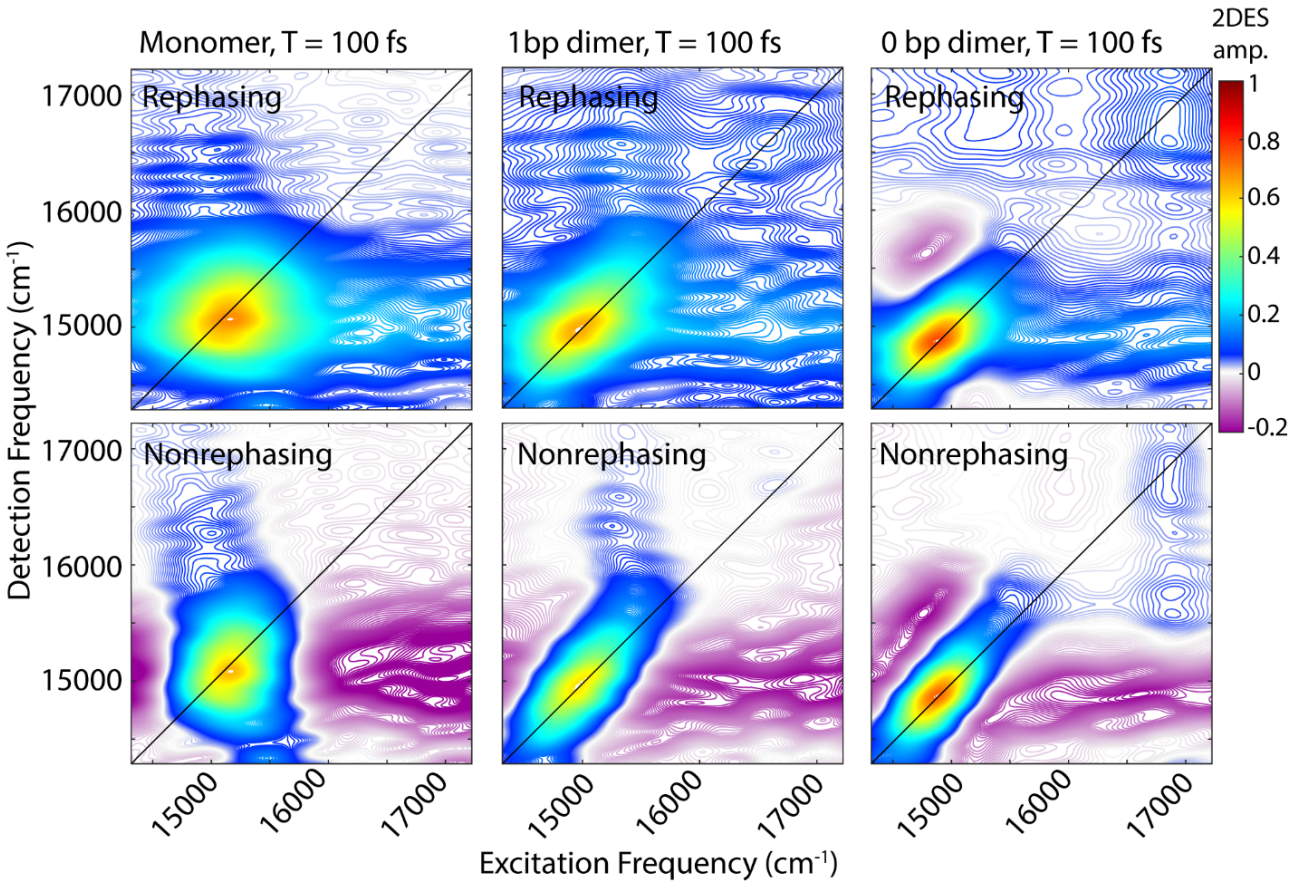

Figure 4.4: Rephasing (top row) and nonrephasing (bottom) row 2DES spectra for the monomer (left), 1 bp dimer (center), and 0 bp dimer (right) constructs. All three constructs show strong excited state absorption (negative) signal at the below diagonal cross peak location.

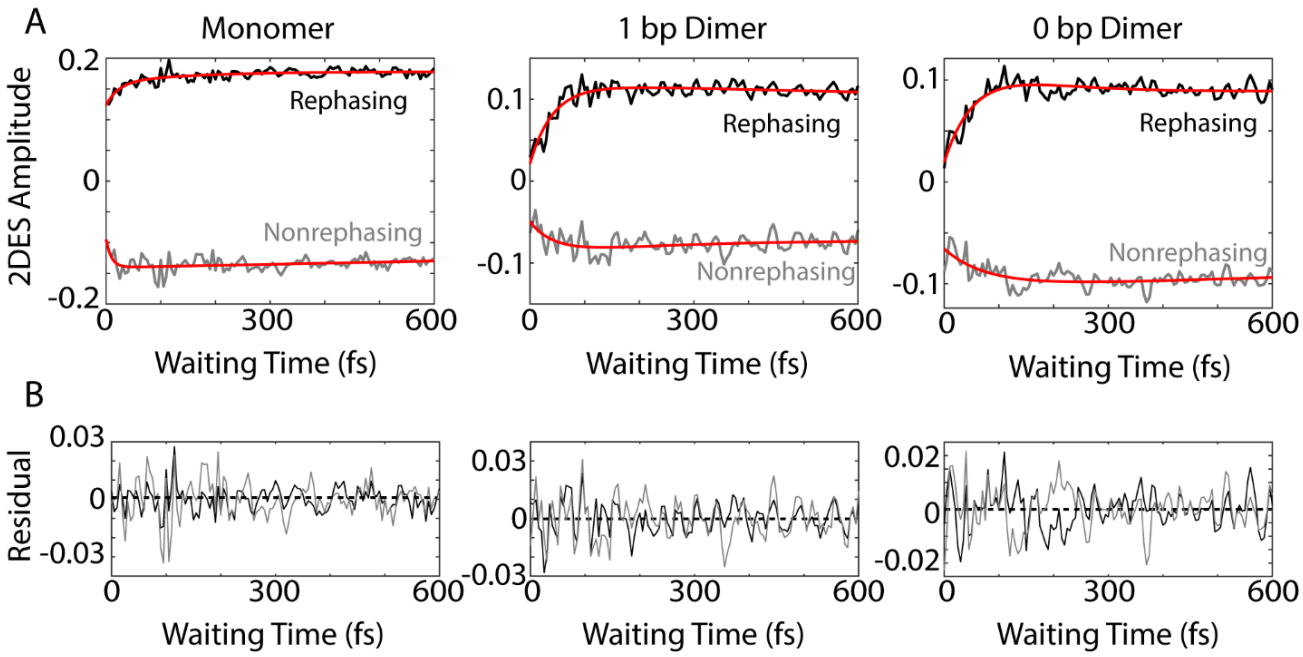

Figure 4.5: (A) Rephasing (black) and nonrephasing (gray) waiting time dynamics for the monomer (left), 1 bp dimer (center), and 0 bp dimer (right) at the below diagonal cross peak location. Red curves are bi-exponential fits to the dynamics. (B) The residual oscillations as a function of waiting time after subtracted the bi-exponential fits from the rephasing (black) and nonrephasing (gray) signals. Rephasing and nonrephasing signals have been normalized independently.

rephasing signals for the three constructs. Figure 4.5B shows the residual beating as a function of waiting time after subtraction of bi-exponential fits. Bi-exponential fits were used to ensure complete removal of population dynamics before beating frequency analysis. Nonrephasing power spectra (Figure 4.6) of observed beating are generated by Fourier transforming over the waiting time at each point in the 2D spectrum corresponding to the feature and the below diagonal cross peak and summing the results. The power spectra were generated by summing the nonrephasing signal across the region denoted by the dashed red box in Figure 4.3. Summing over this region, as opposed to looking at the Fourier transform of the signal at a single point in the spectrum, increases the signal-to-noise of the power spectrum.

Comparing the nonrephasing power spectra for the three constructs provides insight into

how increasing excitonic coupling modulates the frequency of observed coherences. The power spectra in Figure 4 show the frequency and power of spectral beating. All three constructs show beating signals at ± 165 cm^{-1}, ± 330 cm^{-1}, and ± 550 cm^{-1}. In the monomer nonrephasing signal, these are the only detectable beating signals. We can determine that they arise from ground or excited states vibrational coherences because they do not match the energy gap between the 0-0 and 0-1 vibronic exciton states ($\sim$1270 cm^{-1}). The presence of positive and negative beating signals at the same three frequencies in the 1 bp dimer and 0 bp dimer indicate that the excitonic coupling between the dyes does not disrupt the underlying vibrational structure of the monomeric Cy5. We had made this assumption when executing the vibronic exciton model by using the same Huang-Rhys factors for all three constructs. Our 2D data now confirms this assumption was valid.

Zooming in on a region of the power spectra (Figure 4.6, lower panel), we see that both of the dimeric constructs have high frequency quantum beating signals that are not observed in the monomer. The 1 bp dimer has oscillations at ± 940 and 1100 cm^{-1}. The 0 bp dimer has oscillations at -990 cm^{-1}, 880 cm^{-1}, 1270 cm^{-1}, and 1545 cm^{-1}. These higher frequency beating signals are either coherent superpositions between vibronic exciton states or vibrational coherences that are enhanced relative to the monomer due to resonance with vibronic transitions. Placing these beating signals in the greater context of the 2D spectrum can point to the most likely origin of the observed coherences. We generate 2D frequency beating maps by taking the Fourier transform over the residual waiting time traces after subtraction of bi-exponential fits at every point in the 2D spectrum. A single beating map is generated for each waiting frequency. The nonrephasing 1270 cm^{-1} and 1545 cm^{-1} beating maps for the 0 bp dimer and the 1100 cm^{-1} beating map for the 1 bp dimer are shown in Figure 4.7.

The localization of beating power for these frequencies at the below diagonal cross peak, with little intensity on the diagonal, indicates that these quantum beats are coherences

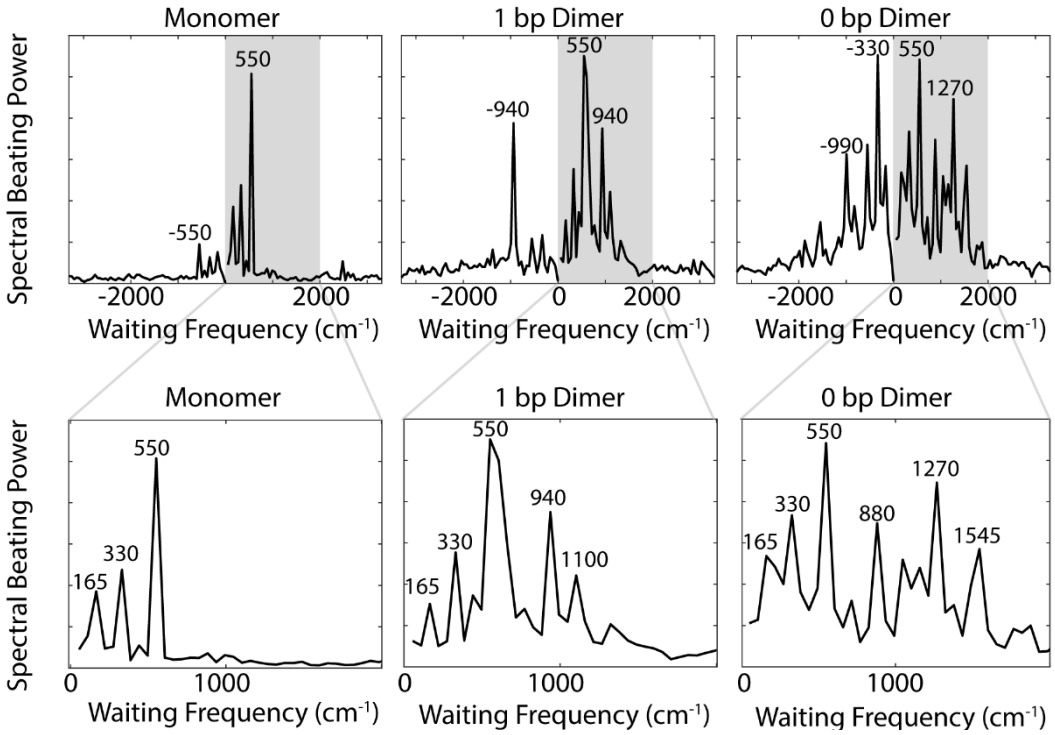

Figure 4.6: (Top) Integrated power spectra of the quantum beating signals at the below diagonal cross peak region generated by Fourier transforming over the residual beating of the nonrephasing signals for the monomer (left), 1 bp dimer (center), and 0 bp dimer (right) constructs. (Bottom) Enlarged view of gray shaded region (0 to 2000 cm^{-1}) from Top. Prominent beating frequencies are labeled for clarity.

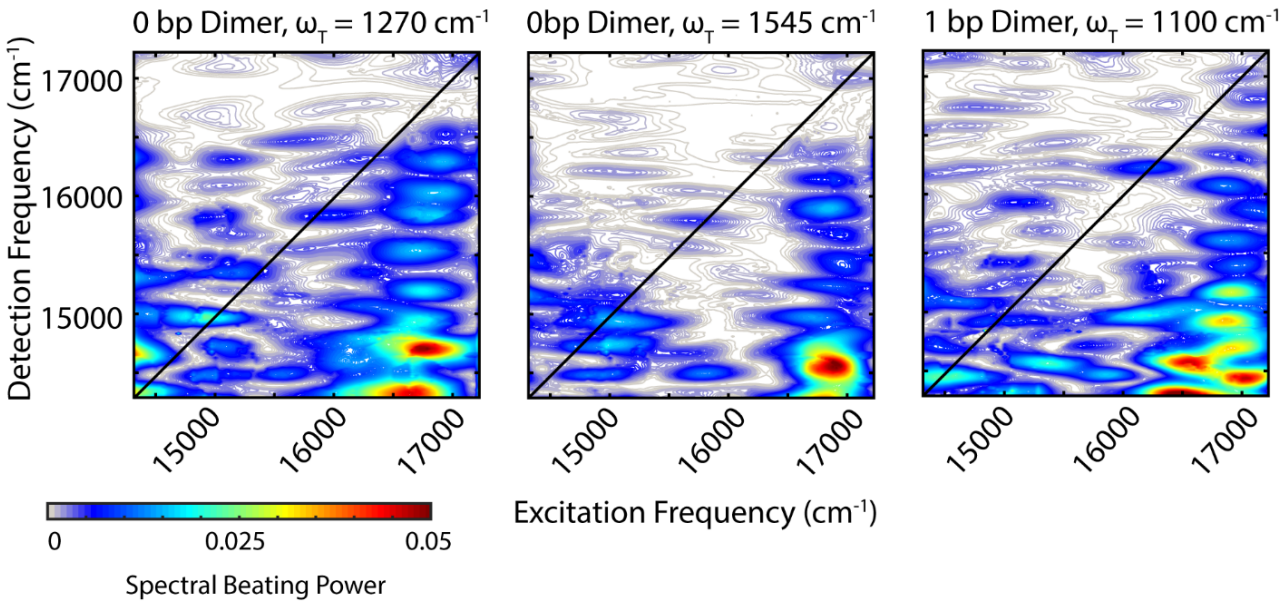

Figure 4.7: The beating frequency maps from the 0 bp dimer nonrephasing 2D data for 1270 cm^{-1} (Left) and 1545 cm^{-1} (Center). Beating frequency map for the 1 bp dimer for 1100 cm^{-1} (Right). These beating signals are likely from coherences between vibronic states.

between the 0-0 and 0-1 vibronic states. The frequencies, 1270 cm^{-1} and 1545 cm^{-1}, roughly match the separations between the vibronic states calculated by our vibronic exciton model (Figure 4.2, bottom) for the 0 bp dimer. The 1100 cm^{-1} mode observed in the nonrephasing power spectrum for the 1 bp dimer also matches the energy gap between vibronic exciton states for that construct (Figure 4.2, middle). The spectral location and frequency of these coherences support that these are superpositions between the 0-0 and 0-1 vibronic exciton states. Beating frequency maps for the 940 cm^{-1} oscillation (Figure 4.11) shows that the beating signals are widespread throughout the 2D spectrum. The mirrored beating at positive and negative frequency for the 940 cm^{-1} oscillation suggests a vibrational origin for this coherence. The beating frequency map for the -940 cm^{-1} mode also show beating signals that are not predominantly localized to the below diagonal cross peak location (Figure 4.11). For the 880 cm^{-1} and -990 cm^{-1} modes in the 0-bp dimer power spectra, beating frequency maps show that the beating signals are not localized to the

below diagonal cross peak region, therefore we attribute these oscillations to be vibrational coherences (Figure 4.11). Beating frequency maps for all prominent beating modes observed in Figure 4.6 are presented in the ESI (Figures 4.11-4.14).

Analyzing possible Feynman pathways supports the conclusion that there is vibronic coherence between the 0-0 and 0-1 states. Double-sided Feynman diagrams depicting possible pathways with oscillations of >1000 cm^{-1} are presented in Figure 4.8. The three nonrephasing Feynman pathways corresponding to oscillatory ESA, SE, and GSB signals all contain one light-matter interaction that induces a transition that is slightly red of our laser bandwidth. The peak energy of this transition may be just outside our experimental bandwidth; however, if the transition from the 0-1 vibronic state (represented as e_2 in Figure 4.8) to a higher-lying excited state f we see in the nonrephasing ESA pathway is broad and carries a large transition dipole moment, it could be accessed with our laser spectrum. In addition, the vertical structure of the beating we see in the 1270 cm^{-1} and 1545 cm^{-1} beating frequency map for the 0 bp dimer at excitation frequency ~16,700 cm^{-1} suggests that the higher lying excited state f contains a vibrational progression through which we see relaxation to a lower energy state. This vibrational structure can both explain the observed vertical pattern of beating and would indicate that the e_2 to f transition is not necessarily out of our bandwidth.

There are competing explanations as to the microscopic origins of observed coherences in the presence of vibronic coupling. Jonas and co-workers [8] proposed that observed coherences are ground-state vibrational coherences that are enhanced due to vibronic coupling and thus report on the electronic excited state. Mančal and co-workers [1] propose that vibronic coupling induces beating on both the ground and excited states when the electronic transition on one monomer is resonant with a vibrational mode on the excited state of the other monomer. We believe that the latter more fully explains our observations as we see beating localized to a region of the nonrephasing spectrum where ESA signal dominates.

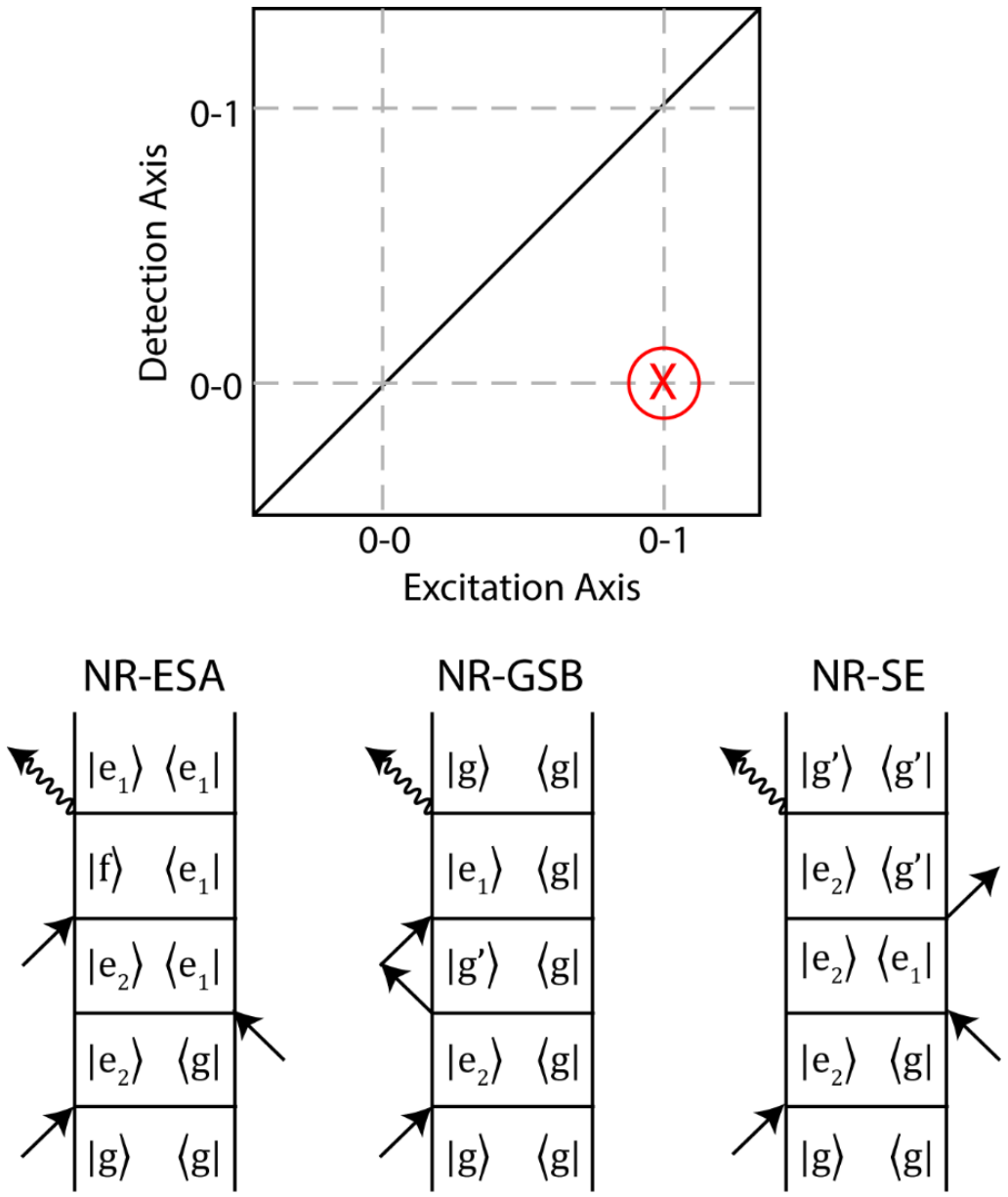

Figure 4.8: Double-sided Feynman diagrams depicting nonrephasing ESA (left), GSB (center), and SE (right) pathways that beat during the waiting time at a frequency of resonant with the separation of the 0-0 and 0-1 vibronic states (<1000 cm^{-1}). The diagrams correspond to pathways at the spectral location marked by the red "X" in the sketch of the 2D spectrum (below diagonal cross peak). In the Feynman pathways, g denotes the electronic ground state, e_2 denotes states under the 0-1 transition, and e_1 denotes states under the 0-0 transition. The state f represents a higher lying excited state and the apostrophes are used to indicate a vibrational excitation (in this case on the electronic ground state, g').

4.6 DNA Scaffold Supports Long-Lived Vibronic Coherence at Small Base Pair Separations

To assess whether using a DNA scaffold to hold the dyes in close proximity more successfully replicates the vibronic coherences seen in photosynthetic pigment-protein complexes, we examined how long our observed coherences persist. By eliminating the first 100 fs of waiting time dynamics and then remaking the beating frequency maps, we can conclude whether or not our beating signals persist beyond 100 fs. Our observed coherence persists for hundreds of femtoseconds. Figure 4.9 shows that 1270 cm^{-1} and 1545 cm^{-1} beating frequency maps still show strong beating at the below diagonal cross peak position even if we omit the first 100 fs of waiting time from the Fourier transform. This finding indicates that DNA, like the protein scaffold in photosynthetic pigment-protein complexes can support vibronic coherence. Halpin et al [10] have previously reported on the effect of strong vibronic coupling on coherence between vibronic excitons in a molecular biscyanine dimer in a combined experimental and numerical study. In their work, the authors reported oscillations in the waiting time of the nonrephasing ESA signal with a beat frequency consistent with the energy gap between the two strongest absorbing excitons; however the chosen molecular construct in those experiments could only sustain the vibronic coherence for 80 fs ($1/e$ decay time). [10] Our results indicate that the DNA scaffold can prolong this vibronic coherence relative to covalent linkage between the dyes [10].

4.7 Conclusions

Strong excitonic coupling between closely spaced dyes on DNA induces exciton delocalization. Increased Davydov splitting and redistribution of oscillator strength into higher energy vibronic bands have been reported at separations under 2 base pairs in vibronically coupled dyes. [21] Our 2DES beating frequency analysis shows that the large changes in linear

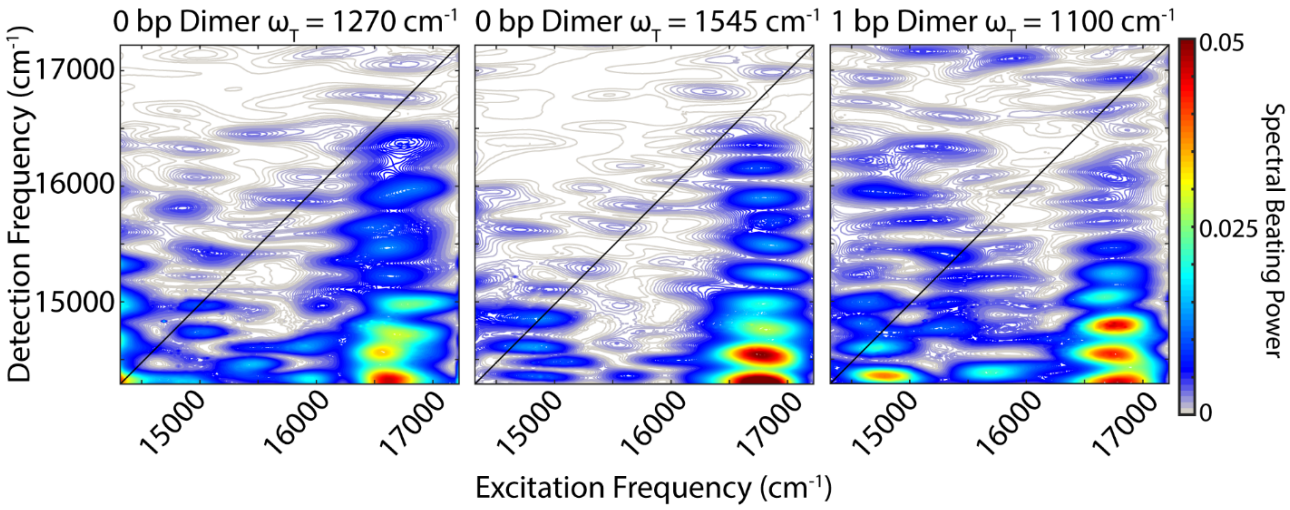

Figure 4.9: Nonrephasing beating frequency maps for a beat frequencies of 1270 cm^{-1} and 1545 cm^{-1} for the 0bp dimer and 1100 cm^{-1} for the 1 bp dimer. These beating frequencies maps were created by Fourier transforming over 100-600 fs of waiting time. A total of 600 fs of positive waiting times were taken in our experiments. That the beating signatures still remain after omission of the first 100 fs of signal, indicate that these coherences are long-lived compared to a purely electronic coherence, persisting for >100 fs.

spectral signatures at small dye separations correspond to detectable coherences between vibronic exciton states delocalized across the dyes. The stronger excitonic coupling between the Cy5 dyes in the 0 bp dimer leads to more pronounced delocalization and stronger coherences resonant with the energetic splitting between the vibronic exciton states of the 0-0 and 0-1 transitions. Like the vibronic coherences observed in photosynthetic pigment-protein complexes [30, 41], our observed coherences in the DNA-dye constructs persist for hundreds of femtoseconds. Our results indicate that organic dyes on a DNA scaffold offer an avenue for building tunable excitonic networks that can support coherent phenomena, an important design principle for building biomimetic light harvesting networks.

4.8 Experimental Methods

4.8.1 Sample Preparation

DNA oligomers were purchased from Integrated DNA Technologies. Complementary unlabeled or Cy5-labeled single strands were combined by thermal cycling to 90 °C and then slowly cooling the sample to 4 °C over an hour. All samples were prepared in 1x TAE buffer.

4.8.2 UV/vis Absorption Spectroscopy

UV/vis spectra were acquired using a Shimadzu UV-1700 spectrometer. Spectra were measured using a 1 mm quartz cuvette (Starna).

4.8.3 GRadient Assisted Photon Echo Spectroscopy (GRAPES)

2DES is a four wave mixing technique that probes frequency-frequency correlations as a function time and in doing so can report on electronic coupling between chromophores, energy transfer pathways, and ultrafast coherent dynamics. [25, 40, 41] In a 2DES experiment, three ultrafast laser pulses interact with the sample to generate a macroscopic oscillating polarization which generates a signal in a defined, phase-matched direction. The first two pulses are separated by coherence time, τ, and produce either a population or a coherence between excited electronic states, vibronic states, or vibrational states. During the waiting time (T), the time delay between the second and third pulses, the system undergoes a combination of coherent oscillation and incoherent relaxation. The arrival of the third pulse initiates the emission of the third-order signal which is a function of the detection time, t. The emitted signal is captured and resolved by a spectrometer and sCMOS camera. Fourier transforms over the coherence time and the detection time give a two-dimensional frequency-frequency correlation map for every waiting time that contain positive signals from stimulated emission (SE) and ground state bleach (GSB) pathways and negative signals from

excited state absorption (ESA) pathways.

The pulses used in these 2DES experiments were produced by focusing the output of a 5 kHz Coherent Legend Elite USP regenerative amplifier seeded by a coherent Micra Ti:Sapph oscillator through 2.25 m argon gas held 4 psi above atmospheric pressure. The broadened output was recompressed via a pair of negative GVD mirrors (Layertec) and then refocused through the argon tube. The resulting supercontinuum white light pulse was compressed using another pair of negative GVD mirrors (Layertec) and a multiphoton intrapulse interference phase scan compressor (Biophotonics Solutions, Inc.). The compressed pulse was 15 fs FWHM, with a spectrum spanning 580-720 nm. The compressed pulse was divided into two using a 50:50 beam splitter (Layertec), with one pulse sent to a retroflecting delay line (Aerotech) to control the waiting time, T. Each pulse was directed to a 40 percent reflective beam splitter (Chroma) in front of a silver mirror angled at $\sim$1.5 degrees, replacing the wedged glass beam splitters used in a previous iteration of GRAPES. The beam splitter-silver mirror pairs create a set of four pulses in a modified BoxCARS geometry, which are overlapped vertically using flat mirrors and focused to vertical lines (1 cm by 60 μm) with a cylindrical mirror. The angle with which pulses 1 and 2 pass through the sample creates a gradient of coherence times (τ), which include negative and positive coherence times. For details on using both negative and positive coherence times in GRAPES to obtain fully absorptive spectra see [44].

The resulting third-order signal co-propagates with pulse 4 (local oscillator, L.O.) which has been attenuated by two orders of magnitude before passing through the sample and is set to arrive 2 ps before the other pulses. Both the sample and the L.O. are focused through an imaging spectrometer (Andor Shamrock 303i) onto a 2D CMOS array (Andor Neo 5.5) running at 20 Hz. Neighboring pixels were binned in both dimensions of the detector such that a 2560 x 2160 array acts as 1280 x 1080 array with four times the pixel area. After binning, the τ spacing on the vertical dimension of the detector was 0.53 fs/pixel

(original pixel size 6.5 μm). Acquired frames were streamed to a solid-state hard drive via Labview (National Instruments) control software using a producer/consumer design. A chopper is used such that the camera collects the heterodyned signal (signal plus L.O.) every second frame. The chopped frames contain only L.O. and pulse 3 scatter which is used for subtraction in the data processing. After chopping, signal acquisition speed is 10 Hz. Fast acquisition enables fine sampling of the waiting time, every 0.5 fs. The use of fine waiting time sampling to remove contamination from scattered light has been described in detail elsewhere [45, 46]. During the measurement, solutions of DNA-dye constructs were contained within a 500 μm flow cell (Starna). The samples were not flowing during the measurement but were flowed in and out of the sample cell using a peristaltic pump in between each of the 16 independent runs to minimize photobleaching.

4.9 Supplementary Figures

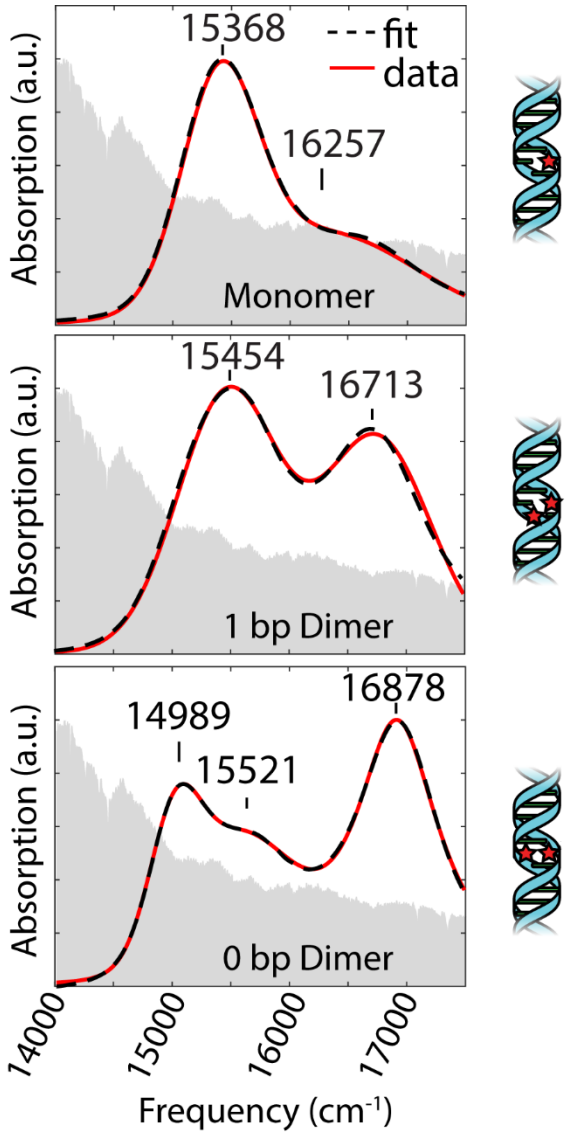

Figure 4.10: Experimental linear absorption spectra of the monomer (top), 1 bp dimer (middle), 0 bp dimer (bottom) shown in red. The dashed black lines are Gaussian fits to the experimental data. The monomer and 1 bp dimer spectra were fit to two Gaussians. The 0 bp dimer spectrum as fit to three Gaussians. Marked peak positions indicate center frequency of the fit Gaussians. Gaussians fits were used to obtain peak locations, not as a physically meaningful fit to the experimental data. Shaded gray region is the laser spectrum used for 2DES experiments. Cartoons to the right of each spectra are a depiction of the corresponding construct.

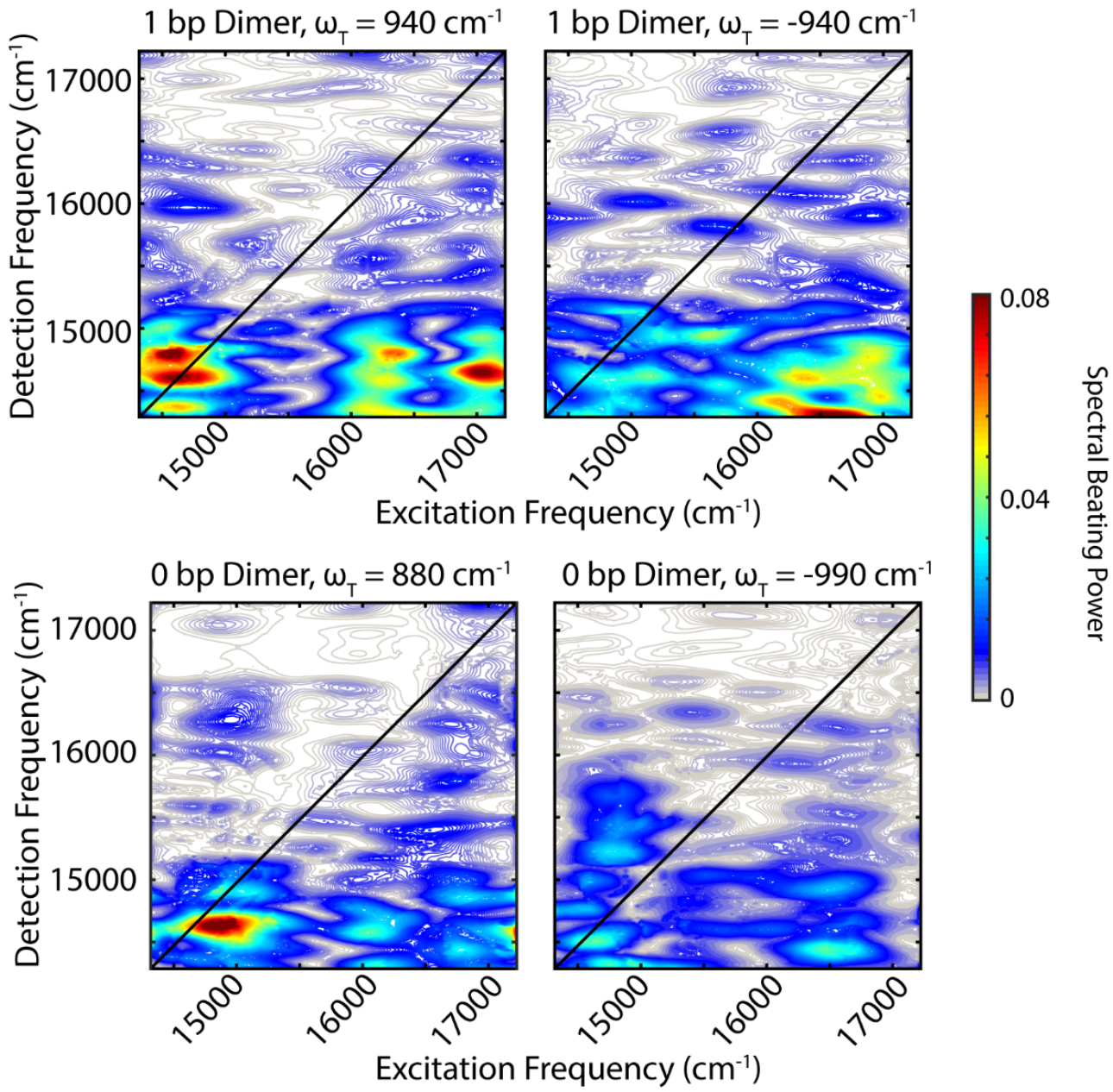

Figure 4.11: Beating frequency maps for oscillatory frequencies attributed to vibrational coherences in the 0 bp and 1 bp dimer constructs. Resolvable vibrational coherences are observed in the dimeric constructs but not the monomeric construct due to resonance of vibrational modes with vibronic transitions in the dimers.

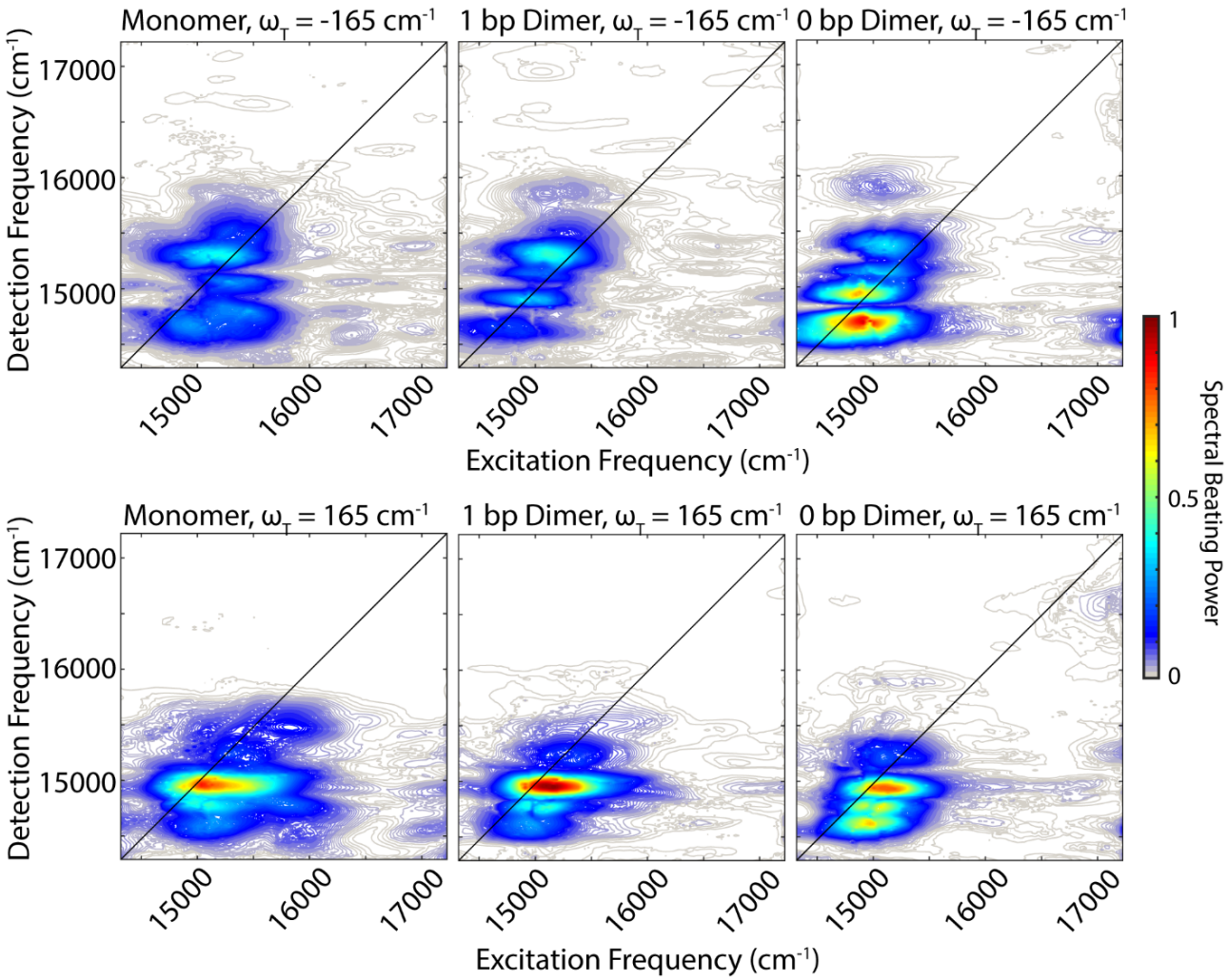

Figure 4.12: Beating frequency maps for the ± 165 cm^{-1} mode for the three studied constructs. We have attributed this beating signal to a vibrational coherence.

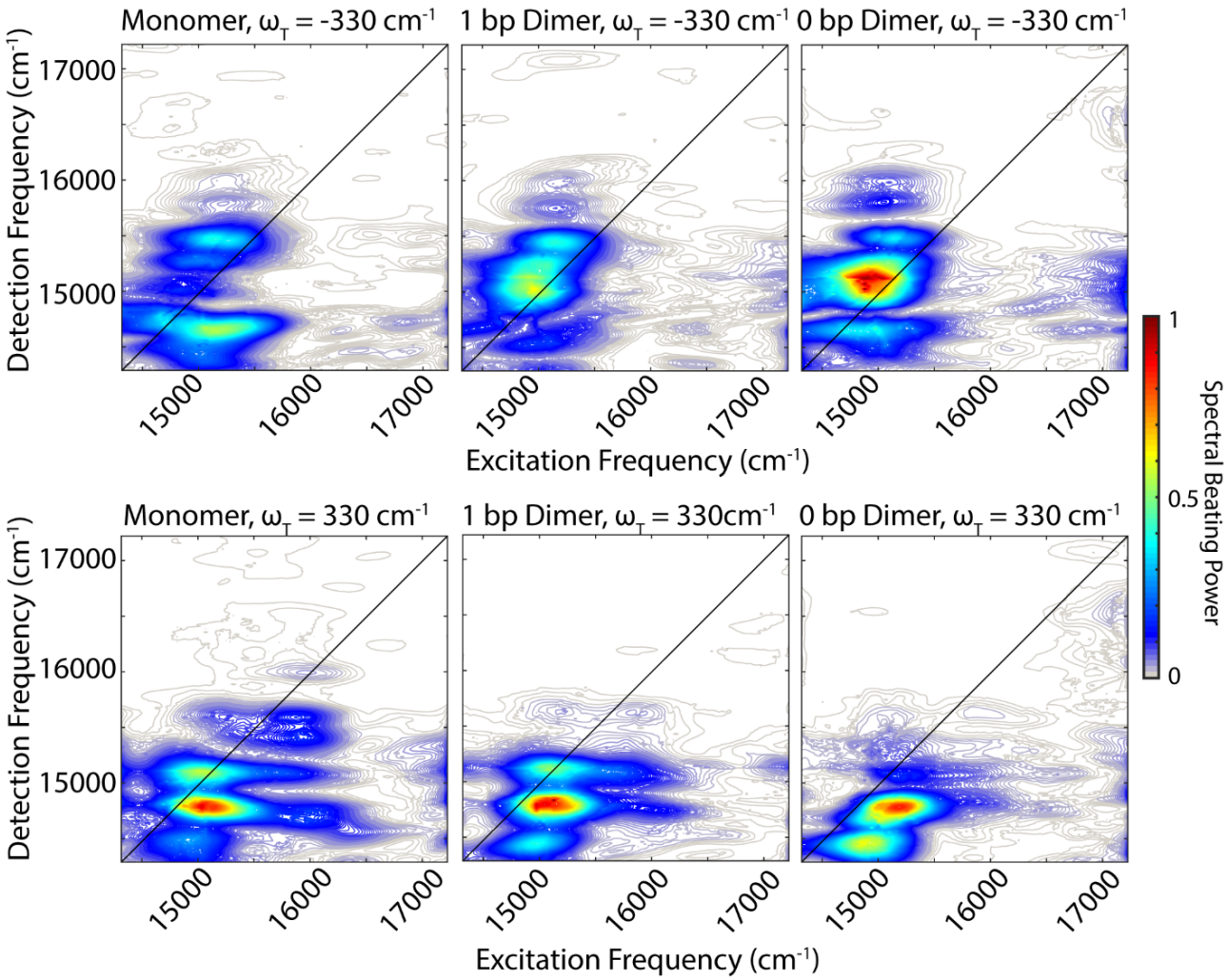

Figure 4.13: Beating frequency maps for the ± 330 cm^{-1} mode for the three studied constructs. We have attributed this beating signal to a vibrational coherence.

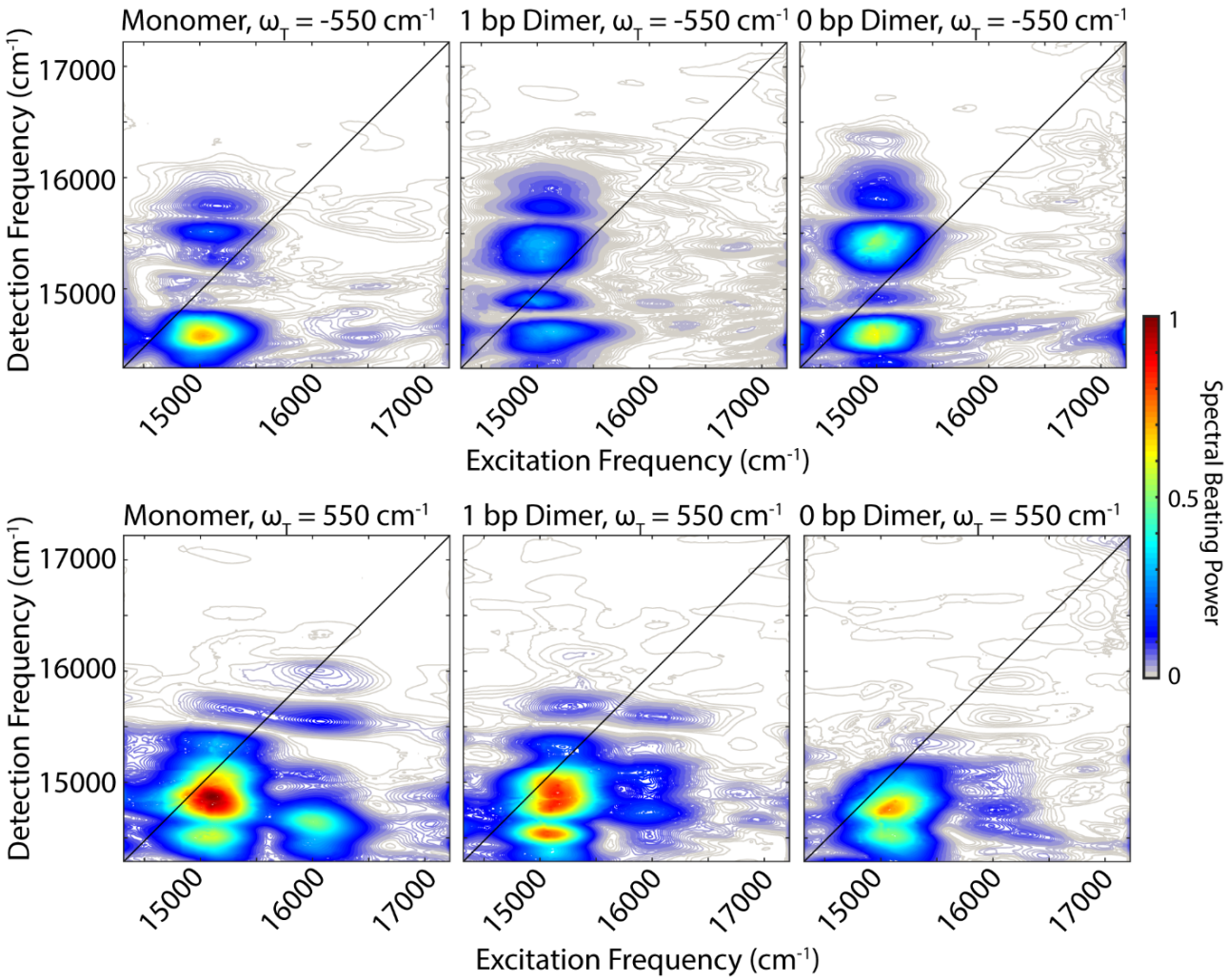

Figure 4.14: Beating frequency maps for the ± 550 cm^{-1} mode for the three studied constructs. We have attributed this beating signal to a vibrational coherence.

REFERENCES

[1] Aurélia Chenu, Niklas Christensson, Harald F. Kauffmann, and Tomáš Mančal. Enhancement of vibronic and ground-state vibrational coherences in 2D spectra of photosynthetic complexes. *Scientific Reports*, 3:2029, 2013.

[2] E. Collini, C. Y. Wong, K. E. Wilk, P. M. Curmi, P. Brumer, and G. D. Scholes. Coherently wired light-harvesting in photosynthetic marine algae at ambient temperature. *Nature*, 463(7281):644–7, 2010.

[3] Peter D. Dahlberg, Graham J. Norris, Cheng Wang, Subha Viswanathan, Ved P. Singh, and Gregory S. Engel. Communication: Coherences observed in vivo in photosynthetic bacteria using two-dimensional electronic spectroscopy. *The Journal of Chemical Physics*, 143(10):101101, 2015.

[4] Marco Ferretti, Vladimir I. Novoderezhkin, Elisabet Romero, Ramunas Augulis, Anjali Pandit, Donatas Zigmantas, and Rienk van Grondelle. The nature of coherences in the B820 bacteriochlorophyll dimer revealed by two-dimensional electronic spectroscopy. *Physical Chemistry Chemical Physics*, 16(21):9930–9939, 2014.

[5] M. L. Flanagan, P. D. Long, P. D. Dahlberg, B. S. Rolczynski, S. C. Massey, and G. S. Engel. Mutations to *R. sphaeroides* reaction center perturb energy levels and vibronic coupling but not observed energy transfer rates. *J Phys Chem A*, 120(9):1479–87, 2016.

[6] Franklin D. Fuller, Jie Pan, Andrius Gelzinis, Vytautas Butkus, S. Seckin Senlik, Daniel E. Wilcox, Charles F. Yocum, Leonas Valkūnas, Darius Abramavicius, and Jennifer P. Ogilvie. Vibronic coherence in oxygenic photosynthesis. *Nat Chem*, 6(8):706–711, 2014.

[7] G. S. Schlau-Cohen, A. Ishizaki, T. R. Calhoun, N. S. Ginsberg, M. Ballottari, R. Bassi, and G. R. Fleming. Elucidation of the timescales and origins of quantum electronic coherence in LHCII. *Nat Chem*, 4(5):389–95, 2012.

[8] V. Tiwari, W. K. Peters, and D. M. Jonas. Electronic resonance with anticorrelated pigment vibrations drives photosynthetic energy transfer outside the adiabatic framework. *Proc Natl Acad Sci U S A*, 110(4):1203–8, 2013.

[9] A. W. Chin, J. Prior, R. Rosenbach, F. Caycedo-Soler, S. F. Huelga, and M. B. Plenio. The role of non-equilibrium vibrational structures in electronic coherence and recoherence in pigment–protein complexes. *Nature Physics*, 9(2):113–118, 2013.

[10] Alexei Halpin, Philip J. M. Johnson, Roel Tempelaar, R. Scott Murphy, Jasper Knoester, Thomas L. C. Jansen, and R. J. Dwayne Miller. Two-dimensional spectroscopy of a molecular dimer unveils the effects of vibronic coupling on exciton coherences. *Nature Chemistry*, 6(3):196–201, 2014.

[11] V. Tiwari, W. K. Peters, and D. M. Jonas. Energy transfer: Vibronic coherence unveiled. *Nat Chem*, 6(3):173–5, 2014.

[12] Maximilian Schlosshauer. Decoherence, the measurement problem, and interpretations of quantum mechanics. *Reviews of Modern Physics*, 76(4):1267–1305, 2005.

[13] R. Shankar. *Principles of Quantum Mechanics*. Springer US, 2 edition, 1994.

[14] James Lim, David Paleček, Felipe Caycedo-Soler, Craig N. Lincoln, Javier Prior, Hans von Berlepsch, Susana F. Huelga, Martin B. Plenio, Donatas Zigmantas, and Jürgen Hauer. Vibronic origin of long-lived coherence in an artificial molecular light harvester. *Nature Communications*, 6:7755, 2015.

[15] L. Wang, G. B. Griffin, A. Zhang, F. Zhai, N. E. Williams, R. F. Jordan, and G. S. Engel. Controlling quantum-beating signals in 2D electronic spectra by packing synthetic heterodimers on single-walled carbon nanotubes. *Nat Chem*, 9(3):219–225, 2017.

[16] Susan Buckhout-White, Christopher M. Spillmann, W. Russ Algar, Ani Khachatrian, Joseph S. Melinger, Ellen R. Goldman, Mario G. Ancona, and Igor L. Medintz. Assembling programmable FRET-based photonic networks using designer DNA scaffolds. *Nature Communications*, 5(1), 2014.

[17] P. D. Cunningham, A. Khachatrian, S. Buckhout-White, J. R. Deschamps, E. R. Goldman, I. L. Medintz, and J. S. Melinger. Resonance energy transfer in DNA duplexes labeled with localized dyes. *J Phys Chem B*, 118(50):14555–65, 2014.

[18] Anja Dietrich, Volker Buschmann, Christian Müller, and Markus Sauer. Fluorescence resonance energy transfer (FRET) and competing processes in donor–acceptor substituted DNA strands: a comparative study of ensemble and single-molecule data. *Reviews in Molecular Biotechnology*, 82(3):211–231, 2002.

[19] T. Kato, H. Kashida, H. Kishida, H. Yada, H. Okamoto, and H. Asanuma. Development of a robust model system of FRET using base surrogates tethering fluorophores for strict control of their position and orientation within DNA duplex. *J Am Chem Soc*, 135(2):741–50, 2013.

[20] Joseph S. Melinger, Ani Khachatrian, Mario G. Ancona, Susan Buckhout-White, Ellen R. Goldman, Christopher M. Spillmann, Igor L. Medintz, and Paul D. Cunningham. FRET from multiple pathways in fluorophore-labeled DNA. *ACS Photonics*, 3(4):659–669, 2016.

[21] Paul D. Cunningham, Young C. Kim, Sebastián A. Díaz, Susan Buckhout-White, Divita Mathur, Igor L. Medintz, and Joseph S. Melinger. Optical properties of vibron-

ically coupled cy3 dimers on DNA scaffolds. *The Journal of Physical Chemistry B*, 122(19):5020–5029, 2018.

[22] Sergey Polyutov, Oliver Kühn, and Tõnu Pullerits. Exciton-vibrational coupling in molecular aggregates: Electronic versus vibronic dimer. *Chemical Physics*, 394(1):21–28, 2012.

[23] Franz Milota, Valentyn I. Prokhorenko, Tomas Mančal, Hans von Berlepsch, Oliver Bixner, Harald F. Kauffmann, and Jürgen Hauer. Vibronic and vibrational coherences in two-dimensional electronic spectra of supramolecular J-aggregates. *The Journal of Physical Chemistry A*, 117(29):6007–6014, 2013.

[24] T. Brixner, T. Mančal, I. V. Stiopkin, and G. R. Fleming. Phase-stabilized two-dimensional electronic spectroscopy. *J Chem Phys*, 121(9):4221–36, 2004.

[25] Tobias Brixner, Jens Stenger, Harsha M. Vaswani, Minhaeng Cho, Robert E. Blankenship, and Graham R. Fleming. Two-dimensional spectroscopy of electronic couplings in photosynthesis. *Nature*, 434(7033):625–628, 2005.

[26] Minhaeng Cho, Harsha M. Vaswani, Tobias Brixner, Jens Stenger, and Graham R. Fleming. Exciton analysis in 2D electronic spectroscopy. *The Journal of Physical Chemistry B*, 109(21):10542–10556, 2005.

[27] M. L. Cowan, J. P. Ogilvie, and R. J. D. Miller. Two-dimensional spectroscopy using diffractive optics based phased-locked photon echoes. *Chemical Physics Letters*, 386(1–3):184–189, 2004.

[28] Vytautas Butkus, Donatas Zigmantas, Leonas Valkūnas, and Darius Abramavicius. Vibrational vs. electronic coherences in 2D spectrum of molecular systems. *Chemical Physics Letters*, 545:40–43, 2012.

[29] C. Kreisbeck, T. Kramer, and A. Aspuru-Guzik. Disentangling electronic and vibronic coherences in two-dimensional echo spectra. *J Phys Chem B*, 117(32):9380–5, 2013.

[30] Daniel B. Turner, Krystyna E. Wilk, Paul M. G. Curmi, and Gregory D. Scholes. Comparison of electronic and vibrational coherence measured by two-dimensional electronic spectroscopy. *The Journal of Physical Chemistry Letters*, 2(15):1904–1911, 2011.

[31] Elana M. S. Stennett, Ning Ma, Arjan van der Vaart, and Marcia Levitus. Photophysical and dynamical properties of doubly linked cy3–DNA constructs. *The Journal of Physical Chemistry B*, 118(1):152–163, 2014.

[32] Heinz Mustroph, Knut Reiner, Jürgen Mistol, Steffen Ernst, Dietmar Keil, and Lothar Hennig. Relationship between the molecular structure of cyanine dyes and the vibrational fine structure of their electronic absorption spectra. *ChemPhysChem*, 10(5):835–840, 2009.

[33] Francesca Nicoli, Matthias K. Roos, Elisa A. Hemmig, Marco Di Antonio, Regina de Vivie-Riedle, and Tim Liedl. Proximity-induced H-aggregation of cyanine dyes on DNA-duplexes. *The Journal of Physical Chemistry A*, 120(50):9941–9947, 2016.

[34] Villy Sundström and Tomas Gillbro. Excited state dynamics and photophysics of aggregated dye chromophores in solution. *The Journal of Chemical Physics*, 83(6):2733–2743, 1985.

[35] Michael Kasha. Energy transfer mechanisms and the molecular exciton model for molecular aggregates. *Radiation Research*, 20(1):55–70, 1963.

[36] Brittany L. Cannon, Lance K. Patten, Donald L. Kellis, Paul H. Davis, Jeunghoon Lee, Elton Graugnard, Bernard Yurke, and William B. Knowlton. Large Davydov splitting and strong fluorescence suppression: An investigation of exciton delocalization in DNA-

templated Holliday junction dye aggregates. *The Journal of Physical Chemistry A*, 122(8):2086–2095, 2018.

[37] M. Schröter, S. D. Ivanov, J. Schulze, S. P. Polyutov, Y. Yan, T. Pullerits, and O. Kühn. Exciton–vibrational coupling in the dynamics and spectroscopy of frenkel excitons in molecular aggregates. *Physics Reports*, 567:1–78, 2015.

[38] Oliver Kühn, Thomas Renger, and Volkhard May. Theory of exciton-vibrational dynamics in molecular dimers. *Chemical Physics*, 204(1):99–114, 1996.

[39] J. Han, H. Zhang, and D. Abramavicius. Exchange narrowing and exciton delocalization in disordered J aggregates: simulated peak shapes in the two dimensional spectra. *J Chem Phys*, 139(3):034313, 2013.

[40] Y. C. Cheng and G. R. Fleming. Dynamics of light harvesting in photosynthesis. *Annu Rev Phys Chem*, 60:241–62, 2009.

[41] Yuan-Chung Cheng, Gregory S. Engel, and Graham R. Fleming. Elucidation of population and coherence dynamics using cross-peaks in two-dimensional electronic spectroscopy. *Chemical Physics*, 341(1):285–295, 2007.

[42] D. B. Turner, R. Dinshaw, K. K. Lee, M. S. Belsley, K. E. Wilk, P. M. Curmi, and G. D. Scholes. Quantitative investigations of quantum coherence for a light-harvesting protein at conditions simulating photosynthesis. *Phys Chem Chem Phys*, 14(14):4857–74, 2012.

[43] Andrea Volpato, Luca Bolzonello, Elena Meneghin, and Elisabetta Collini. Global analysis of coherence and population dynamics in 2D electronic spectroscopy. *Optics Express*, 24(21):24773–24785, 2016.

[44] S. H. Sohail, P. D. Dahlberg, M. A. Allodi, S. C. Massey, P. C. Ting, E. C. Martin, C. N. Hunter, and G. S. Engel. Communication: Broad manifold of excitonic states in

light-harvesting complex 1 promotes efficient unidirectional energy transfer *in vivo*. *J Chem Phys*, 147(13):131101, 2017.

[45] Elad Harel, Andrew F. Fidler, and Gregory S. Engel. Real-time mapping of electronic structure with single-shot two-dimensional electronic spectroscopy. *Proceedings of the National Academy of Sciences*, 107(38):16444–16447, 2010.

[46] Elad Harel, Andrew F. Fidler, and Gregory S. Engel. Single-shot gradient-assisted photon echo electronic spectroscopy. *The Journal of Physical Chemistry A*, 115(16):3787–3796, 2011.

CHAPTER 5

TWO-DIMENSIONAL ELECTRONIC SPECTROSCOPY OF LIVING CYANOBACTERIA CELLS

Cyanobacteria use peripheral light-harvesting antenna, phycobilisomes, to harvest solar excitations and funnel them to the cyanobacterial reaction centers where charge separation occurs to initiate photochemistry. The phycobilisomes are extremely delicate complexes that can freely associate and dissociate with either of the two photosystems (fused antenna/reaction center complexes) that are embedded in the thylakoid membrane. As they are not membrane-bound, upon cell lysis, the phycobilisomes remain soluble in the aqueous fraction while the photosystems are membrane-bound. This makes it impossible to study energy transfer through the phycobilisome to the reaction centers unless the organism remains intact. This is not the case for other photosynthetic organisms such as purple bacteria and algae, in which all key photosynthetic machinery is embedded in a membrane. Studying the complete pathway of energy transfer in cyanobacteria requires an ultrafast *in vivo* measurement. GRadient-Assisted Photon Echo Spectroscopy (GRAPES) has *in vivo* capabilities and we present the first two-dimensional electronic spectrum of a living cyanobacteria, acquired using GRAPES. We see absorption features corresponding to the photosystems and several components of the phycobilisomes. Future work includes improving the signal-to-noise of the measurement and using *in vivo* GRAPES to track ultrafast dynamical changes to alterations in environmental conditions in real time.

5.1 Energy Transfer Pathways in Cyanobacteria

The phycobilisome (PBS) is the primary light-harvesting antenna for cyanobacteria. [1–5] The PBS has a rod-core structure that associates with the lumenal side of the thylakoid membrane. The PBS rods are made up of the phycobiliprotein (PBP) phycocyanin and, in some

species, phycoerythrin as well. The rods are attached to an allophycocyanin (APC) core. [3, 6] The PBS represents a spatial and energetic funnel, a light-harvesting motif seen in many photosynthetic organisms. Each PBP contains bilins, tetrapyrrole pigments, that are covalently linked to the surrounding protein. The rod pigments absorb the highest energy photons and can transfer energy downhill to APC core, which absorbs at a slightly lower energy. Phycoerythrin absorption is centered at 580 nm, phycocyanin absorption is centered around 630 nm, and the APC core absorbs around 650 nm. [4] Excitations captured by the PBS are transferred from the APC core to the chlorophyll pigments in the fused antenna/reaction center complexes, Photosystem I (PSI) and Photosystem II (PSII), where trapping by the reaction centers occurs. [7] A complete map of energy transfer dynamics through the PBS to the photosystems is inaccessible by standard spectroscopic techniques. [4] Most time-resolved spectroscopic measurements of light-harvesting and energy transfer dynamics must be done on isolated complexes or intact thylakoid membranes. The PBS dissociates from the thylakoid membrane upon cell lysis, preventing experiments that can measure the complete pathways of energy transfer. We have applied our *in vivo* two-dimensional electronic spectroscopy in order to examine energy transfer dynamics and couplings in living cyanobacteria cells.

5.2 Photoprotective Mechanisms in Cyanobacteria

One of the large motivators behind adapting our GRAPES setup for use with living cyanobacterial samples is accessing the changes in ultrafast energy transfer pathways as a result of photoprotection. While our spectroscopic capabilities are not quite at the point of being able to study these dynamics, *in vivo* GRAPES is uniquely positioned to examine real-time response to changing environmental conditions. Oxygenic phototrophs use a variety of photoprotective and photoacclimation mechanisms to quench excess excitations. Photoprotection is the organism's response to rapid fluctuations in irradiance. These defense

mechanisms prevent the buildup of excited chlorophyll pigments. An excess of these singlet excited chlorophyll that cannot be transferred to the reaction center can decay into triplet chlorophyll. Triplet chlorophyll can react with triplet oxygen in the atmosphere to produce singlet oxygen. Singlet oxygen is a dangerous oxidizer that can severely damage the photosynthetic apparatus. Cyanobacteria have two major means of dealing with excess excitations: state transitions and non-photochemical quenching. [8]

State transitions involve the redistribution of excitations between PSI and PSII. The PBS is highly mobile and energy transfer from the PBS to each of the photosystems can be regulated through changes in the affinity of the PBS to each PSI and PSII. [9] *State 1* refers to preferential excitation of PSI and *State 2* refers to preferential excitation of PSII. Increased illumination causes a transition from *State 2* to *State 1*. Historically, this transition has been monitored using the fluorescence intensity from PSII. After the transition to *State 1*, there is an increase in PSII fluorescence due to decreased photoquenching of PSII excitations for photosynthesis. The existence of state transitions as the predominant photoprotective mechanism in cyanobacteria has been well known for several decades; however, the specific ultrafast energy pathways and quantum dynamics of the transitions between *State 1* and *State 2* remain unknown.

Non-photochemical quenching (NPQ) was more recently discovered as a photoprotective mechanism in cyanobacteria. [10] NPQ in cyanobacteria uses a pigment-protein complex distinct from the photosynthetic light-harvesting machinery to quench excitations in the phycobilisome. This specialized protein, orange carotenoid protein (OCP), binds a single 3'-hydroxyechinenone (hECN) carotenoid molecule. [5, 11–13] Upon exposure to blue-green light, OCP is photactivated, undergoing conformational rearrangement from its inactive orange form (OCP^O) to its active red form (OCP^R). The activated OCP^R binds to the PBS and induces ultrafast quenching. The molecular mechanics and quantum dynamics of this quenching is unknown. It has been suggested that the carotenoid directly accepts excitations

from the PBS or that the binding of OCP^R to the PBS induces a conformational change in the PBS resulting in quenching of excitations. [11]

5.3 Two-Dimensional Electronic Spectroscopy of Living *S. Leopoliensis* cells

5.3.1 Experimental Challenges

We have successfully acquired 2DES spectra on living *Rba. sphaeroides*. [14–17] The logical extension of our *in vivo* capabilities was to use 2DES to examine light harvesting and energy transfer dynamics in more complex organisms. Evolutionarily, cyanobacteria present the logical next step and contain the photosynthetic machinery that builds the foundation for photosynthesis in green algae and higher plants. Successfully capturing energy transfer dynamics in cyanobacteria has presented many experimental challenges and has required significant adaptation of the GRAPES instrumentation (see Section 2.2). A close examination of how the live cell sample should be prepared to give the highest signal-to-noise is also important.

Two marked differences between cyanobacteria and purple bacteria make cyanobacteria a significantly more challenging sample for *in vivo* GRAPES. Cyanobacteria cells are substantially larger than purple bacteria (*Rba. sphaeroides*) and they contain chlorophyll instead of bacteriochlorophyll which absorbs higher energy light. This combination of size and absorption energy makes the cyanobacteria cells a more highly scattering spectroscopic sample than purple bacteria. This difference in optical scattering can be seen in the baseline of the linear absorption spectra for each of the cell cultures (Figure 5.1). Generally, purple bacteria are sub-micron in both dimensions (*Rba. sphaeroides* are ∼800 nm by ∼300 nm). We have examined two different genus of widely studied cyanobacteria, *Synechocystis* and *Synechoccocus*. *Synechocystis* are circularly shaped with a diameter of $\sim$ 2.5 to 3.5 μm.

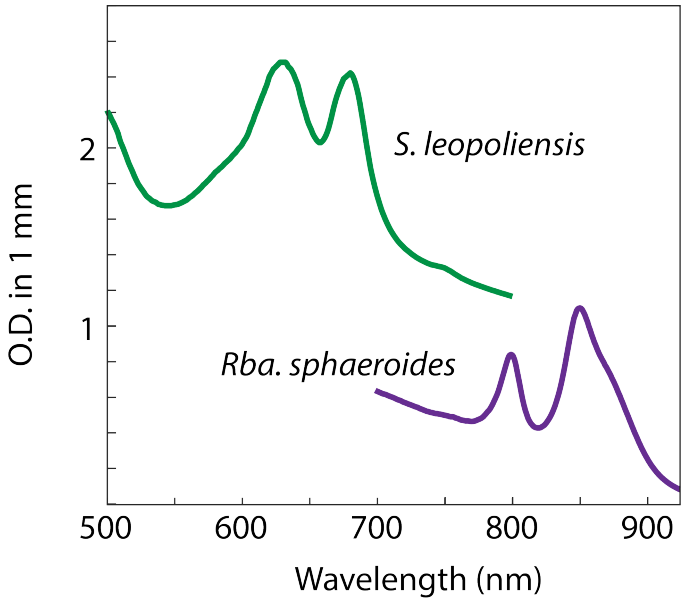

Figure 5.1: A comparison of the scatter baseline of *Rba. sphaeroides* (purple) cells and *S. leopoliensis* cells (green) in their linear absorption spectra. Both live cell samples were prepared to a final O.D. of 0.3 to 0.4 above the scatter baseline in a 200 μm or 500 μm sample cell for 2DES experiments.

Synechoccocus leopoliensis are rod shaped. They are 800 to 900 nm in the narrow dimension and range from a 5 to 15 μm in length. The difference in morphology can be seen in the micrographs presented in Figure 5.2. The morphological differences between *Synechocystis* and *Synechoccocus* cells have permitted the collection of 2DES spectra for *Synechoccocus*, only. Scattering intensity of thin rod-shaped particles is much less than spheres or disks, [18] thus it is not surprising that we were unable to surpass the severe scatter from *Synechocystis* cells and detect a 2DES signal.

5.3.2 Analysis of 2DES Data

We successfully collected a 2DES spectra from living *S. leopoliensis* cells (Figure 5.3). The 2DES spectra of *S. leopoliensis* cells show three diagonal features. The two higher energy features are PBS features and range from 625 nm to 675 nm. Photosystems I and II give rise to the lowest energy diagonal feature at 680 nm. As a function of waiting time, we see

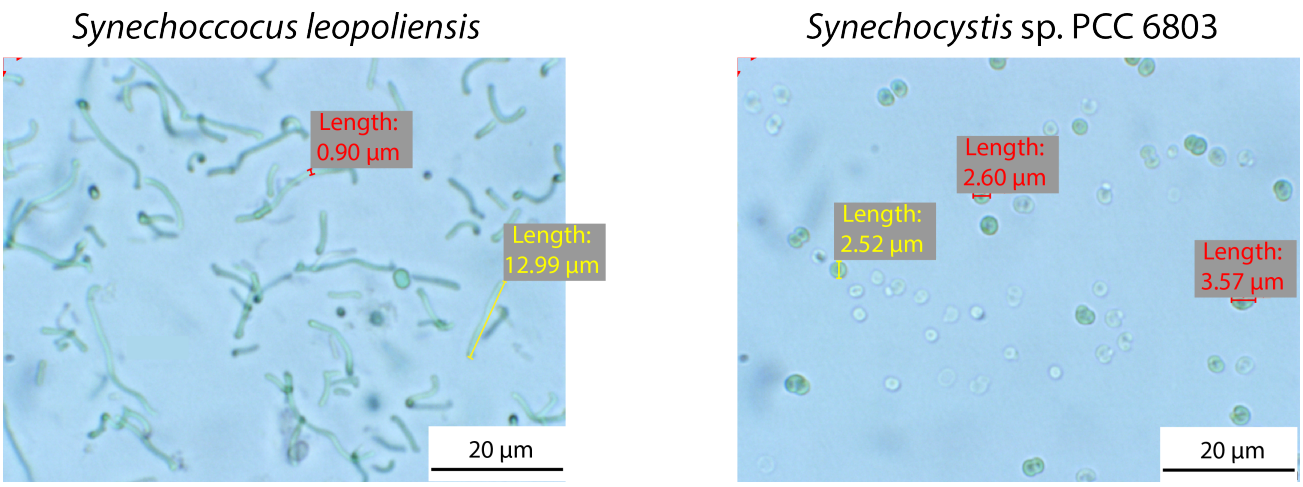

Figure 5.2: Optical micrographs of *Synechoccocus* and *Synechocystis* cyanobacteria cells. The rod shape of *Synechoccocus* makes it easier to get a 2DES *in vivo* signal from these cells due to lower scatter contributions.

relaxation to below diagonal features. The signal-to-noise of the acquired spectra make it difficult to parse out specific energy transfer pathways in the data, but we do see resolvable dynamics in the feature corresponding to the photosystems and the PBS features. Transfer from the rod pigments of the PBS to the APC core occurs within 10 ps and trapping by the APC takes 100 ps. [7, 19–21] Our 2DES spectra only report on 600 fs of waiting time so we are unable to observe these kinetics in our data set. However, the diagonal feature corresponding to the phycocyanin pigments in the rods of the PBS shows an ultrafast decay and its corresponding below diagonal feature is much more prominent (Figure 5.4). These sub-100 fs dynamics could be due to an ultrafast intra-complex relaxation or a solvation event. Given the low signal-to-noise of the data it is difficult to discern more detailed information.

The maximum of the feature corresponding to PSI and PSII falls slightly below the diagonal ($\lambda_{exc} = 678nm, \lambda_{det} = 691nm$) even at T = 0 fs. This is not dissimilar to what has been seen in other 2DES measurements on isolated PSI. [22] The appearance of this feature below the diagonal is attributed to the laser spectrum having more intensity on the lower

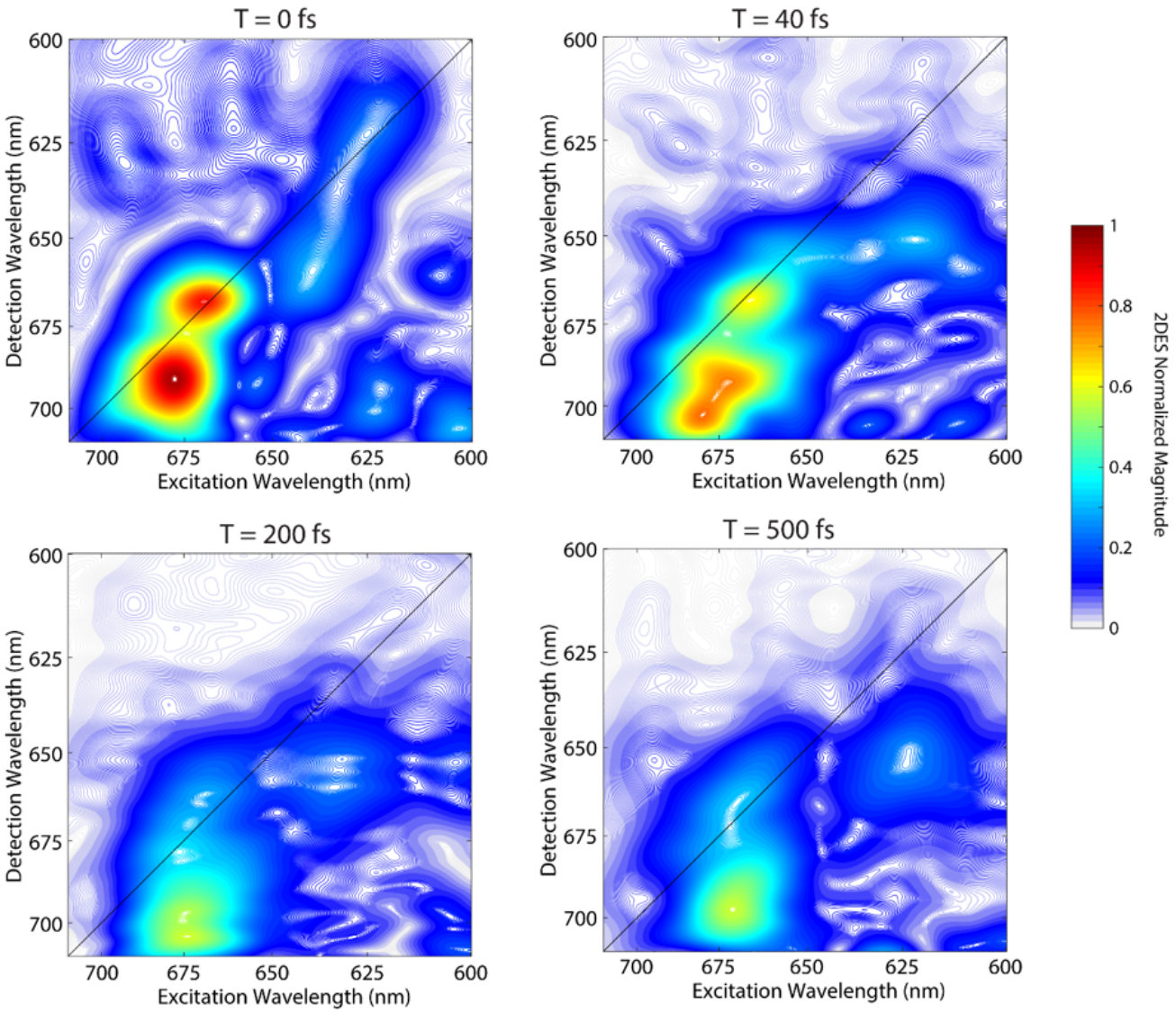

Figure 5.3: Early times *in vivo* 2DES spectra of *S. leopoliensis* cells. Upper diagonal features correspond to PBS rods and core and the lowest energy below diagonal feature corresponds to PSI and PSII.

energy side. The timescale of our measurement is likely too short to see evidence of energy transfer between the PBS core and the photosystems, but analysis of the PSI/PSII feature on this timescale reveals excitation wavelength-dependent dynamics (Figure 5.5). Because this data set was unable to be phased successfully, the dynamics close to T = 0 fs are difficult to interpret as non-resonant transient grating signals have not been eliminated through phase correction. Still, if we ignore the very early time dynamics, we see a trend across different excitation wavelengths for the same detection wavelength. The higher energy side of the photosystem feature shows slower decay dynamics with almost no decay on the timescale of our measurement. As we move across the feature to higher detection wavelengths (lower detection energies), the signal decays more quickly. We believe the differences in dynamics are attributed to coupling between the APC core and the photosystems. The timescale for energy transfer bewteen the APC core and chlorophyll pigments in PSII is believed to be on the order of 100-200 ps [9, 20] and, therefore, would not be resolvable in this data set.

5.4 Conclusions and Future Work

The 2DES spectra of living cells presented in this chapter represent a proof of principle that GRAPES is capable of being adapted as an *in vivo* spectrometer for oxygenic phototrophs. Because the PBS dissociates from the thylakoid membrane upon cell lysis, *in vivo* studies are the only path to mapping native energy transfer pathways in these organisms. *In vivo* GRAPES also enables measurement of the response of ultrafast energy transfer pathways and dynamics to changing environmental conditions. Short-term photoprotective mechanisms are enacted on the timescale of minutes and, therefore, also necessitate a live cell measurement. The data presented here pave the way for further studies in high and low light conditions. In order to study OCP, we will need to push our laser spectrum to bluer wavelengths, but *in vivo* GRAPES represents the only current method that can access the mechanism of OCP-induced quenching.

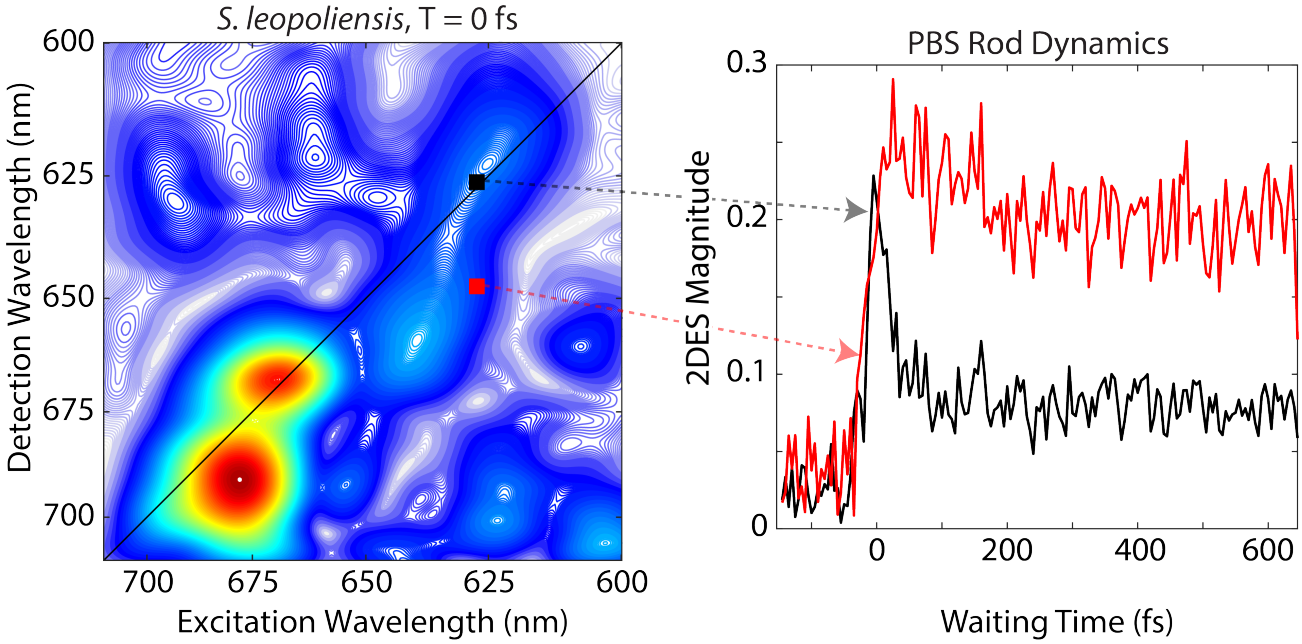

Figure 5.4: The diagonal feature corresponding to the PBS rods (highest energy) shows an initial ultrafast relaxation in the first 100 fs of the measurement (black trace). The below diagonal feature at the same excitation wavelength but a detection wavelength equal to the lower energy rod pigments does not show this initial ultrafast decay. This may be due to an initial ultrafast equilibration to the lowest energy pigments in the rods in preparation for energy transfer to the PBS core which happens on a timescale beyond the range of this measurement.

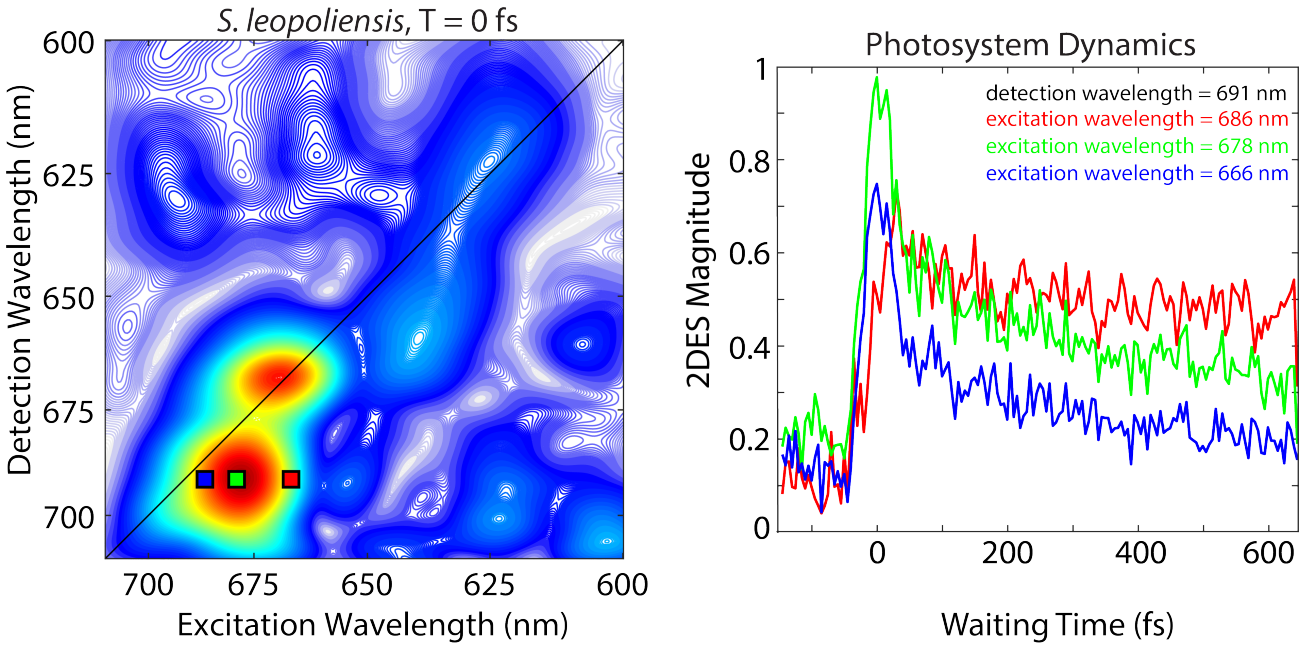

Figure 5.5: The feature corresponding to the cyanobacterial photosystems show excitation wavelength-dependent dynamics. Slowest decays occur on the higher energy side of the photosystem feature.

REFERENCES

[1] Noam Adir. Elucidation of the molecular structures of components of the phycobilisome: reconstructing a giant. *Photosynthesis Research*, 85(1):15–32, 2005.

[2] Robert MacColl. Cyanobacterial phycobilisomes. *Journal of Structural Biology*, 124(2):311–334, 1998.

[3] Alexander N. Glazer. Phycobilisome a macromolecular complex optimized for light energy transfer. *Biochimica et Biophysica Acta (BBA) - Reviews on Bioenergetics*, 768(1):29–51, 1984.

[4] Rafael G. Saer and Robert E. Blankenship. Light harvesting in phototrophic bacteria: structure and function. *Biochemical Journal*, 474(13):2107–2131, 2017.

[5] Diana Kirilovsky and Cheryl A. Kerfeld. The orange carotenoid protein in photoprotection of Photosystem II in cyanobacteria. *Biochimica et Biophysica Acta (BBA) - Bioenergetics*, 1817(1):158–166, 2012.

[6] Robert E. Blankenship. *Molecular Mechanisms of Photosynthesis*. John Wiley& Sons, Ltd, Chinchester, West Sussex, 2nd edition, 2014.

[7] G. W. Suter and A. R. Holzwarth. A kinetic model for the energy transfer in phycobilisomes. *Biophysical journal*, 52(5):673–683, 1987.

[8] Shaun Bailey and Arthur Grossman. Photoprotection in cyanobacteria: Regulation of light harvesting. *Photochemistry and Photobiology*, 84(6):1410–1420, 2008.

[9] J. J. van Thor, C. W. Mullineaux, H. C. P. Matthijs, and K. J. Hellingwerf. Light harvesting and state transitions in cyanobacteria. *Botanica Acta*, 111(6):430–443, 1998.

[10] D. Campbell, V. Hurry, A. K. Clarke, P. Gustafsson, and G. Oquist. Chlorophyll fluorescence analysis of cyanobacterial photosynthesis and acclimation. *Microbiology and molecular biology reviews : MMBR*, 62(3):667–683, 1998.

[11] Dvir Harris, Ofir Tal, Denis Jallet, Adjélé Wilson, Diana Kirilovsky, and Noam Adir. Orange carotenoid protein burrows into the phycobilisome to provide photoprotection. *Proceedings of the National Academy of Sciences*, 113(12):E1655, 2016.

[12] Rudi Berera, Ivo H. M. van Stokkum, Michal Gwizdala, Adjélé Wilson, Diana Kirilovsky, and Rienk van Grondelle. The photophysics of the orange carotenoid protein, a light-powered molecular switch. *The Journal of Physical Chemistry B*, 116(8):2568–2574, 2012.

[13] Denis Jallet, Adrien Thurotte, Ryan L. Leverenz, François Perreau, Cheryl A. Kerfeld, and Diana Kirilovsky. Specificity of the cyanobacterial orange carotenoid protein: Influences of orange carotenoid protein and phycobilisome structures. *Plant Physiology*, 164(2):790, 2014.

[14] S. H. Sohail, P. D. Dahlberg, M. A. Allodi, S. C. Massey, P. C. Ting, E. C. Martin, C. N. Hunter, and G. S. Engel. Communication: Broad manifold of excitonic states in light-harvesting complex 1 promotes efficient unidirectional energy transfer *in vivo*. *J Chem Phys*, 147(13):131101, 2017.

[15] Peter D. Dahlberg, Po-Chieh Ting, Sara C. Massey, Marco A. Allodi, Elizabeth C. Martin, C. Neil Hunter, and Gregory S. Engel. Mapping the ultrafast flow of harvested solar energy in living photosynthetic cells. *Nature Communications*, 8(1):988, 2017.

[16] Peter D. Dahlberg, Graham J. Norris, Cheng Wang, Subha Viswanathan, Ved P. Singh, and Gregory S. Engel. Communication: Coherences observed *in vivo* in photosyn-

thetic bacteria using two-dimensional electronic spectroscopy. *The Journal of Chemical Physics*, 143(10):101101, 2015.

[17] Peter D. Dahlberg, Andrew F. Fidler, Justin R. Caram, Phillip D. Long, and Gregory S. Engel. Energy transfer observed in live cells using two-dimensional electronic spectroscopy. *The Journal of Physical Chemistry Letters*, 4(21):3636–3640, 2013.

[18] Dmitri I. Svergun and Michel H. J. Koch. Small-angle scattering studies of biological macromolecules in solution. *Reports on Progress in Physics*, 66(10):1735–1782, 2003.

[19] A. R. Holzwarth, J. Wendler, and G. W. Suter. Studies on chromophore coupling in isolated phycobiliproteins: II. Picosecond energy transfer kinetics and time-resolved fluorescence spectra of C-Phycocyanin from *Synechococcus* 6301 as a function of the aggregation state. *Biophysical journal*, 51(1):1–12, 1987.

[20] Georg W. Suter, Paola Mazzola, Joachim Wendler, and Alfred R. Holzwarth. Fluorescence decay kinetics in phycobilisomes isolated from the bluegreen alga *Synechococcus* 6301. *Biochimica et Biophysica Acta (BBA) - Bioenergetics*, 766(2):269–276, 1984.

[21] Jingquan Zhao, Jinchang Zhu, and Lijin Jiang. Study on the energy transfer processes in phycobilisomes from blue-green algae by the use of stochastic simulation approach. *Biochimica et Biophysica Acta (BBA) - Bioenergetics*, 1229(1):39–48, 1995.

[22] Yumin Lee, Michael Gorka, John H. Golbeck, and Jessica M. Anna. Ultrafast energy transfer involving the red chlorophylls of cyanobacterial Photosystem I probed through two-dimensional electronic spectroscopy. *Journal of the American Chemical Society*, 140(37):11631–11638, 2018.

CHAPTER 6

FLUENCE-DEPENDENT DYNAMICS OF PHOTOSYSTEM I IN NATIVE THYLAKOID MEMBRANES

Cyanobacteria use three primary complexes to accomplish light-harvesting and charge separation. The phycobilisome is the peripheral light-harvesting antenna that associates with the cytoplasmic side of the thylakoid membrane. The fused antenna/reaction center complexes Photosystem I (PSI) and Photosystem II (PSII) are embedded in the thylakoid membrane. Excitations are funneled from the most distal pigments of the phycobilisome through the photosystems until trapping occurs by the reaction centers. While PSI is the dominant source of chlorophyll in cyanobacteria, the pigments that make up PSI and PSII are only mildly spectrally distinct. This frustrates the assignment of dynamics to specific complexes in cyanobacterial cells or membranes prepared from wild-type cyanobacteria. In this study, we employ intact thylakoid membranes prepared from *Synechocystis* sp. PCC 6803 cells that do not contain PSII. These PSI-only membranes enable us to examine the long-range connectivity of PSI monomers within the membrane. We use power-dependent transient absorption spectroscopy to measure inter-complex dynamics between isoenergetic PSI complexes. We observe clear power-dependent dynamics at the longest wavelength absorbing pigments in PSI, known as the red Chl pool. We attribute these power-dependent dynamics to inter-monomer hopping between red Chl pools before trapping by the reaction center.

6.1 Energy Transfer in Cyanobacterial Thylakoids

There are three major pieces of light-harvesting machinery in cyanobacteria. The phycobilisome (PBS) is a peripheral light harvesting antenna composed of several phycobiliproteins that funnels excitations to the two fused antenna/reaction center complexes, Photosystem I (PSI) and Photosystem II (PSII). PSI and PSII are embedded in the thylakoid membrane

and contain the P700 and P680 reaction centers, respectively. Most of the chlorophyll in cyanobacteria is from PSI. As such, PSI is responsible for most of the spectral signature seen in wild-type thylakoids (Figure 6.1). PSI monomers contain more chlorophyll than PSII monomers, 96 Chl in PSI compared to 35 Chl in PSII, and PSI:PSII ratios range from 2:1 to as high as 10:1. [1, 2]

Room-temperature fluorescence from PSI is extremely weak, as trapping by the P700 reaction center occurs with a 20 ps lifetime in *Synechocystis* sp. PCC 6803. [3] Trapping in PSI is four to five times more efficient than trapping in PSII, therefore photosynthetic efficiency is conventionally measured by PSII fluorescence lifetime which contains a nanosecond decay component. It is undecided whether energy transfer within PSI follows a trap-limited or a diffusion-limited model or some intermediate mechanism. [4] In a trap-limited model, the excited state lifetime is limited by the charge-separation rate at the reaction center. If the trap is shallow, the exciton can escape the trap and return the Chl pool. A diffusion-limited model presumes that the trap is extremely efficient and that the overall excited state lifetime is dependent on the rate at which the exciton reaches the reaction center. In this framework, once the exciton reaches the reaction center, charge separation occurs. PSI additionally contains sets of strongly coupled Chl pigments which lie lower in energy than the P700 reaction center. The precise transition energy of these Chl pools, named the red Chl, and the number of low energy pools are species-specific. Red Chl pools are unique to cyanobacterial PSI and are used to increase the absorption cross section of PSI but also compete with energy transfer to P700. [5–8] Uphill energy transfer from the red Chl pool to P700 is on the order of kT. [9]

The core of the PSII antennae contains CP47 and CP43 subunits and a water oxidation catalytic center. The CP47 and CP43 subunits are most proximal to the P680 reaction center. The P680 reaction center contains four Chl a molecules, two pheophytin a molecules, and two β-carotene molecules. [2, 10] Two-dimensional electronic spectroscopy (2DES) measurements

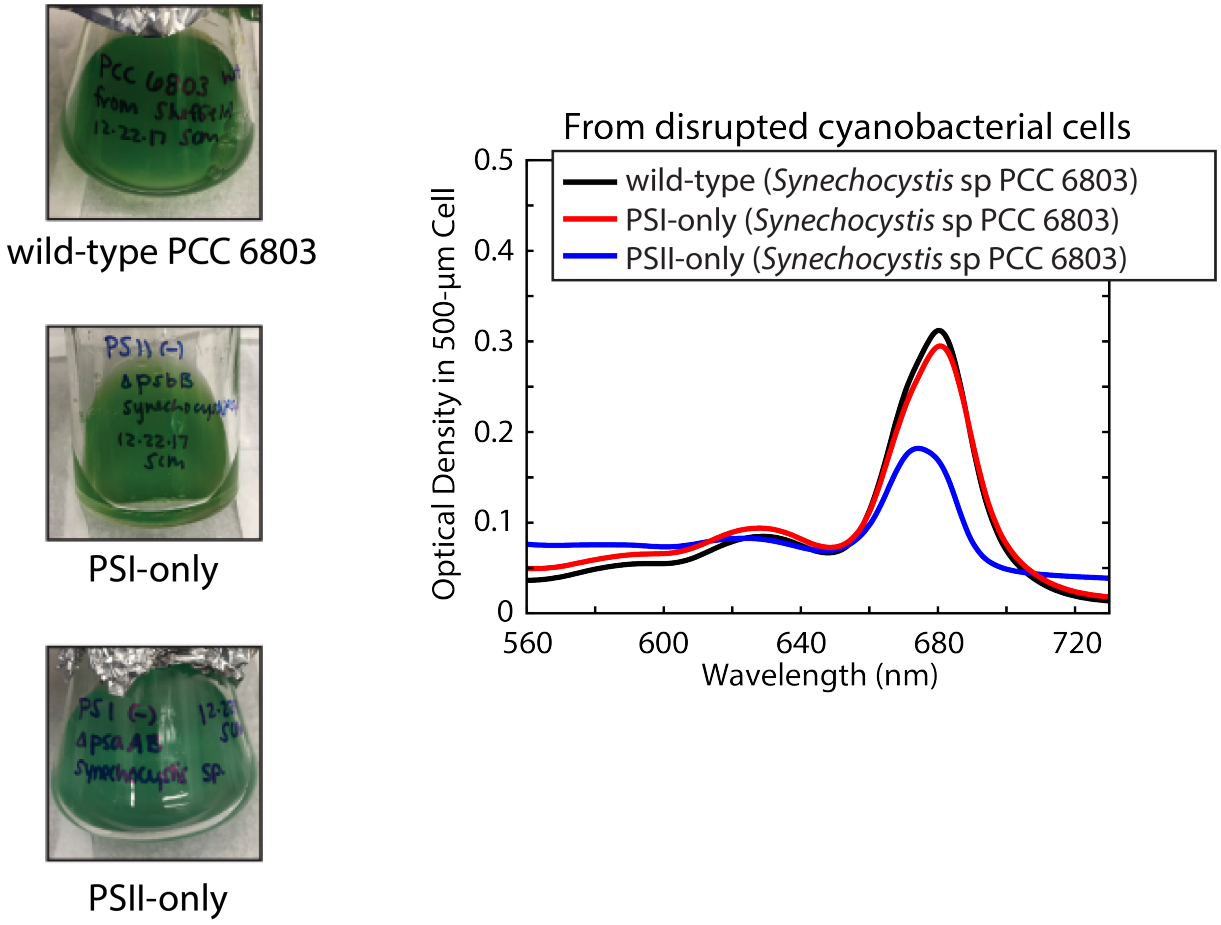

Figure 6.1: (Left) Photographs of cyanobacterial cell cultures for wild-type, PSI-only, and PSII-only *Synechocystis* sp. PCC 6803 cells. (Right) Linear absorption spectra of thylakoid membranes prepared from wild-type (black), PSI-only (red), and PSII-only (blue) cells.

of the PSII core complex from *Thermosynechococcus vulcanus* at 77 K reveal three diagonal features at 670 nm, 677 nm, and 683 nm. Relaxation time constants for these three main features are ∼60 fs. [11] This rapid redistribution of energy to lower lying exciton states is surprising as the pigments within the CP43 and CP47 subunits are only weakly coupled to each other (∼78 cm^{-1} interchromophore coupling). [11, 12]

In the present study, we use singlet-singlet annihilation to study energy flow through PSI and PSII in intact thylakoids prepared from wild-type and mutant *Synechocystis* sp. PCC 6803 cells. We use the annihilation rates to determine the hopping time between isoenergetic complexes using a diffusion-limited.

6.2 Singlet-Singlet Annihilation to Map Energy Flow in Photosynthetic Complexes

Singlet-singlet annihilation occurs due to a dipolar interaction between two excited pigments or excitons. The dipolar interaction causes a non-radiative transition: one molecule relaxes to the ground state and the other is promoted to a higher energy state before rapidly returning to the first excited state. The end result is the annihilation of one of the original excitations. This process results in faster decay dynamics than are observed under conditions with flower excitation density (lower probability of annihilation). [4] The probability of an annihilation event is not only dependent on the number excitations present in the system, but also on the number of pigments or excitons forming a connected domain. The number of excitations absorbed by a given domain is governed by Poisson statistics. [4] That is, a laser fluence that corresponds to one excitation per domain will result in many doubly excited domains. To operate in a regime with extremely low probability of annihilation, laser fluences must correspond to many fewer than one excitation per domain.

The lifetime of an excitation in a photosynthetic antenna can be described by the following equation,

$$\tau_{exc} = \tau_{trap} + \tau_{del} + \tau_{mig} \tag{6.1}$$

where τ_{exc} is the total lifetime of an excitation in a photosynthetic antenna, τ_{trap} is the trapping time, τ_{del} is the transfer time between the antenna and the RC, and τ_{mig} is the migration term. If trapping is trap-limited, then τ_{trap} dominates because this process is much slower than the pigment-to-pigment hopping time. If trapping is diffusion-limited, then τ_{mig} dominates. The τ_{del} term only becomes important if trapping is transfer-to-trap limited. [13]

We use broadband femtosecond transient absorption spectroscopy to measure frequency-resolved ultrafast signals as a function of excitation intensity. In doing so we can reconstruct the energy flow through the fused antenna-reaction center complexes in intact thylakoid membranes.

6.3 Intercomplex Energy Transfer in Cyanobacterial Thylakoids

In the present study, we use intact thylakoid membranes prepared from wild-type and PSI-only *Synechocystis* sp. PCC 6803 cells. Thylakoids were prepared according to the procedure described in Section 2.3.2. Figure 6.1 shows the linear absorption spectra of the wild-type and mutant membrane fragments. The absorption of the Chl *a* Q_y band in *Synechocystis* sp. PCC 6803 is centered at 680 nm. The broad absorption feature seen at 680 nm contains the absorption of both PSI and PSII. The PSII absorbance is blue-shifted relative to PSI with an absorbance maximum at 670 nm (see PSII-only absorption spectra, blue curve in Figure 6.1).

We conducted fluence-dependence studies of wild-type and PSI-only membranes using transient absorption spectroscopy. We initially attempted to use singlet-singlet annihilation to map intra- and inter-complex energy flow in these samples using 2DES, but we were

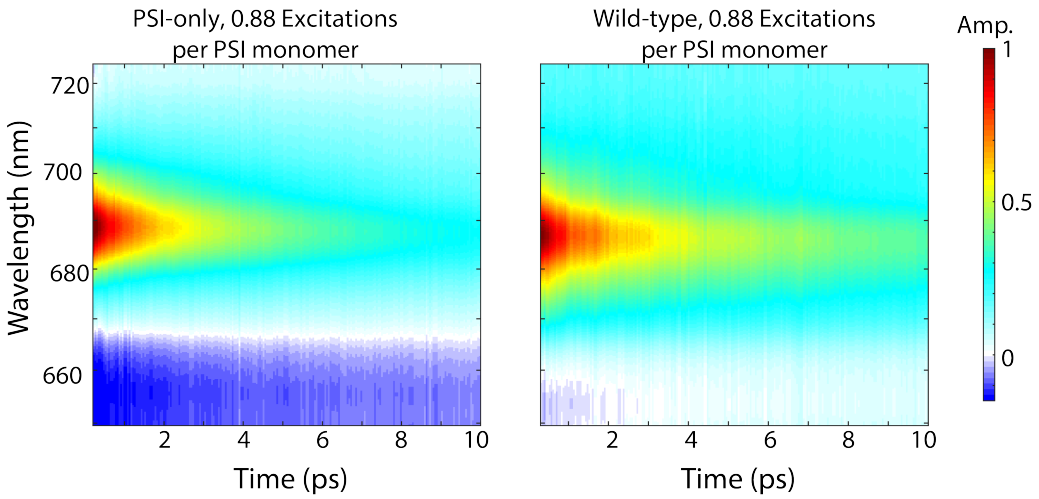

Figure 6.2: (Left) Transient absorption spectrum of PSI-only thylakoids at an excitation power corresponding to 0.88 excitations per PSI monomer. (Right) Transient absorption spectrum of WT thylakoids at the same excitation fluence.

unable to access laser fluences high enough to see annihilation in our GRAPES experimental geometry. Both wild-type and PSI-only transient absorption spectra show a single prominent stimulated emission/ground state bleach (SE/GSB) feature centered near 687 nm and a much weaker excited state absorption (ESA) blue of 667 nm (Figure 6.2). The ESA feature is hardly detectable in the WT spectrum likely due to cancellation of PSI ESA with PSII GSB/SE features at those wavelengths.

We observe singlet-singlet annihilation in PSI-only and WT membranes. As we move to higher excitation fluences we see faster decay dynamics. Interestingly, this power-dependent behavior is localized to specific wavelengths. Figure 6.3 shows the power-dependent decay dynamics in PSI-only membranes. While we observe fluence-dependent dynamics near 700 nm and in the red Chl pool (red of P700), we do not observe fluence-dependent dynamics in the bulk Chl pool. The bulk Chl pool gives rise to the maximum in both the linear absorption (Figure 6.1) and TA spectra (Figure 6.2). Excitations in the red Chl pool must undergo uphill energy transfer to the P700 RC. Excitations in the bulk Chl have energetically favorable transfer to the RC. The difference in direction of energy transfer from the red Chl

to the RC and the bulk Chl to the RC may account for the annihilation we see in the red Chl pool. With less favorable transfer to the trap, trapping of red Chl excitations could be diffusion-limited, whereas excitations in the bulk Chl pool are trap limited, since the energetic funnel to the trap is much more efficient.

Due to a higher energetic barrier to transfer to the trap, we observe a longer τ_{exc} for the red Chl pool than the bulk Chl pool. This leads to inter-complex energy transfer between red Chl pools on neighboring PSI monomers. PSI exists mainly as a trimer *in vivo* and the hopping is likely to occur between red Chl pools on monomers within a trimer. [14] We apply the diffusion-limited model as detailed in [13], in which it was applied to aggregates of an isolated plant antenna. In this diffusion-limited model, the annihilation rate, γ_0, is related to the hopping time, τ_{hop}, bewteen isoenergetic complexes. The equation for the annihilation rate is

$$\gamma_0^{-1} = 0.5 N f_d(N) \tau_{hop} \tag{6.2}$$

where N is the number of connected PSI antenna complexes and $f_d(N)$ is a structural factor representing the packing arrangement. Though previous AFM studies on *Synechocystis* membranes report a random packing arrangement of PSI complexes in the membrane [14], an ordered lattice must be presumed for application of the diffusion-limited trapping model. [13] AFM studies on the arrangement of PSI complexes in thylakoids from *Thermosynechococcus elongatus* report hexagonal packing within the membrane. [14] We use $f_d = 0.6$ which corresponds to a hexagonal lattice in our calculations for this reason. The measured TA signal can then be related to the annihilation rate through the following relationship

$$\log(\frac{1}{n(T)} - \frac{1}{n(0)}) = (d_s/2)\log(T) + \log(\frac{\gamma_0}{d_s}) \tag{6.3}$$

where $n(T)$ is the population of excitations at waiting time T and d_s is the fractal

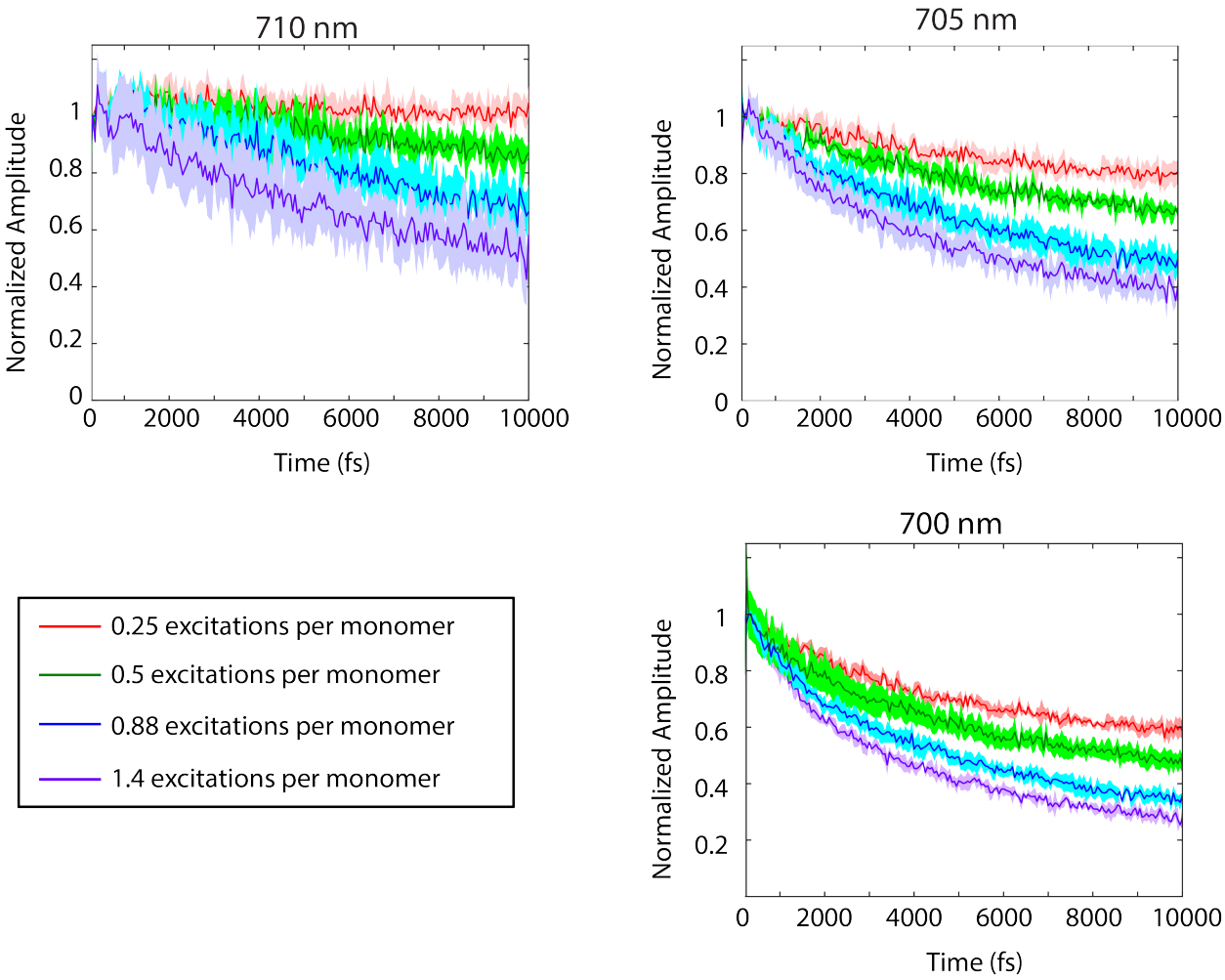

Figure 6.3: Kinetic traces at four excitation fluences from wavelengths corresponding to the red Chl pool of PSI. Trends show faster decay kinetics with increasing excitation intensity at all three wavelengths. The fast kinetics are indicative of singlet-singlet annihilation.

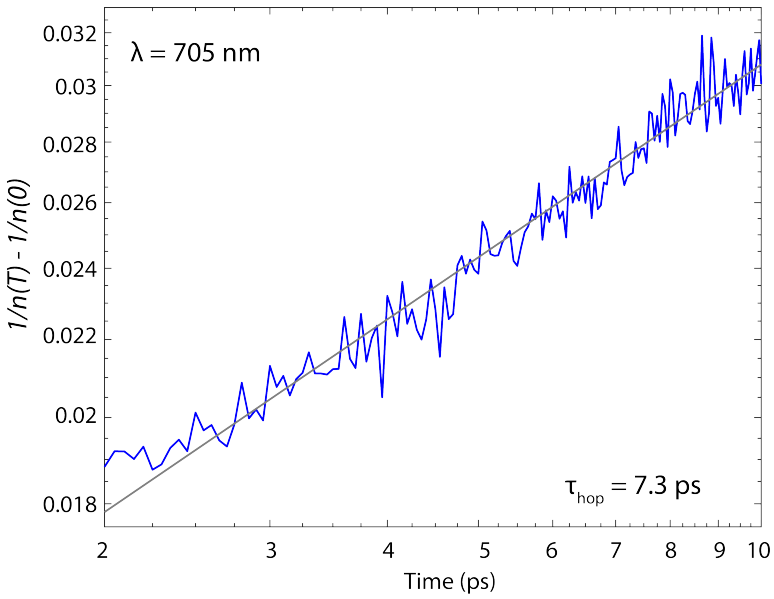

Figure 6.4: Waiting time dynamics at 705 nm from the TA data presented following Equation 6.3. The TA amplitude is $n(T)$. The y-intercept of the linear fit (blue) to the data (gray) gives the annihilation rate. We use this annihilation rate to compute the hopping time (τ_{hop}) between isoenergetic complexes following Equation 6.2.

dimension. The fractal dimension accounts for restricted diffusion in the membrane to the lattice of PSI complexes. [15]

The results of fitting our experimental data from the fluence corresponding to 0.88 excitations per PSI monomer are shown in Figure 6.4. Application of the diffusion-limited model to our TA data yields a hopping time (τ_{hop}) of 7.3 ps between red Chl pools. As seen in Figure 6.4, the data fits well to a line in the log-log plot. The next steps would be to determine how many hops between red Chl pools occur before those excitations end up trapped by the RC. Previous 2DES studies on isolated PSI trimers from *Synechocystis* sp. PCC 6803 indicate that trapping occurs in ∼16 ps for excitations originating in the bulk Chl pool or the red Chl pool. [8] These results would suggest that only 1-2 hops would occur between monomers before trapping occurs. Further modeling is required to confirm this hypothesis.

The experiments run on WT membranes show nearly identical kinetic trends to the PSI-only data (Figure 6.5). This is not completely surprising as PSI is the dominate source of Chl

in this organism. In order to understand trapping and inter-complex connectivity in PSII, we must run experiments on PSII-only membranes. This has proven to be a challenge as cells lacking PSI are extremely challenging to grow. They cannot grow photosynthetically and do not grow to high optical densities. This presents a challenge in gaining enough cell mass to make a membrane preparation with sufficient concentration for an ultrafast experiment. Efforts are ongoing to collect data on PSII-only samples.

6.4 Long Time Dynamics in Cyanobacterial Thylakoids

Preliminary fluence-dependent experiments on PSI-only and WT thylakoids indicated that the most prominent fluence-dependent behavior occurred on a short timescale. While we did not run a complete power-dependence study to look at long time dynamics, but we did collect long time TA data at a single power, corresponding to 0.5 excitations per PSI monomer. Long time PSI-only kinetics at 705 nm are shown in Figure 6.6. Data was collected from -50 ps to 200 ps in 2 ps steps. Unlike the short time data presented in Section 6.2, in which dynamics varied as a function of detection wavelength, the long time data show consistent dynamics across the spectrum. Decay traces fit well ($R^2 > 0.98$) to a monoexponential with an offset. The decay constant from the fit consistently yields $\tau = \sim 22$ ps. This time constant represents trapping by the RC in PSI and this process dominates all other decay pathways on this timescale. This time constant is longer than the time constant reported in recent 2DES studies of isolated PSI trimers from *Synechocystis* sp. PCC 6803 [8], but is within the range reported by other studies. [3, 16] Discrepancies can also arise due to our maintaining the PSI complexes in their native thylakoid environment, rather than completely isolating them in detergent.

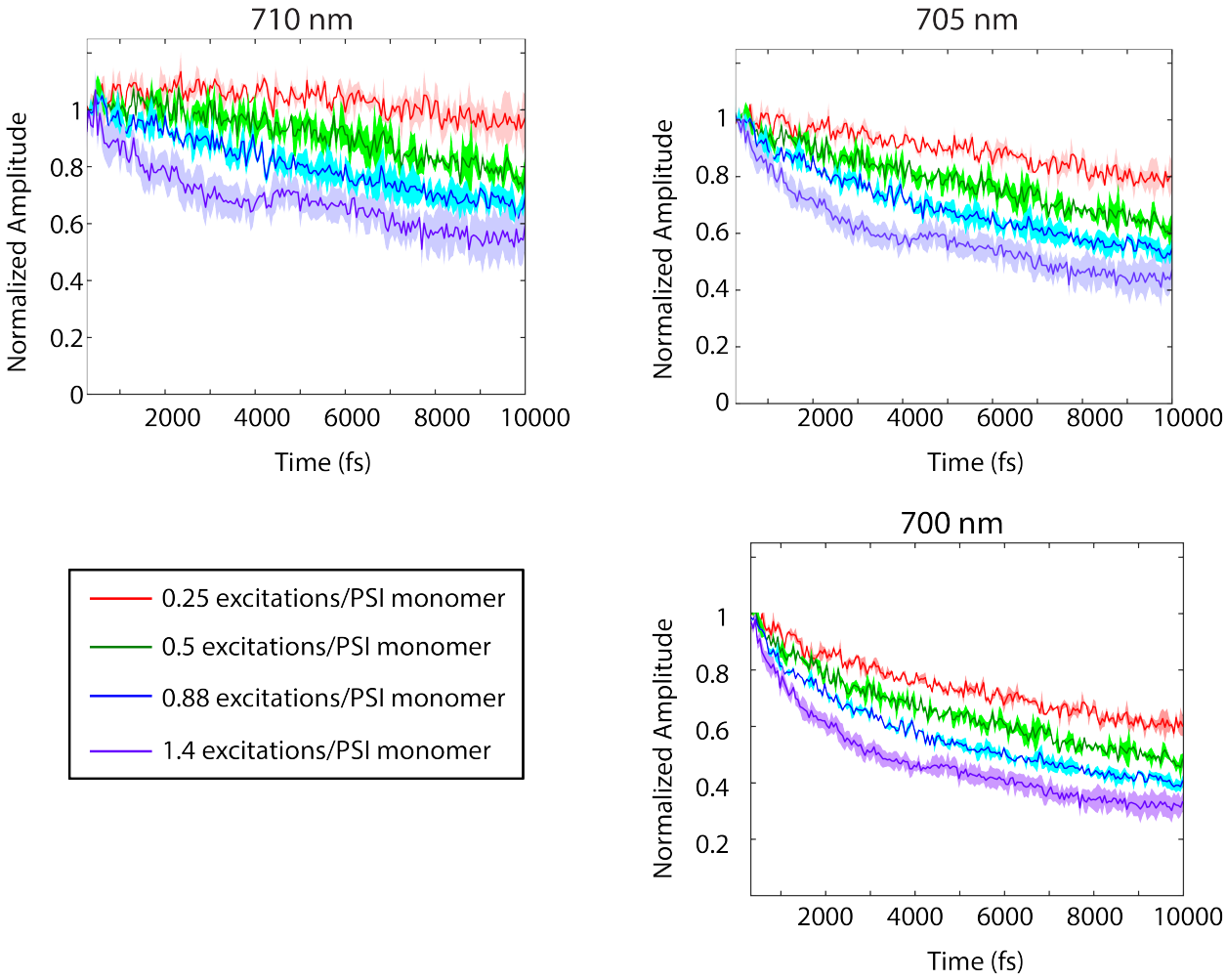

Figure 6.5: Kinetic traces at four excitation fluences from wavelengths corresponding to the red Chl pool of PSI in WT thylakoid membranes. Trends show faster decay kinetics with increasing excitation intensity at all three wavelengths. The fast kinetics are indicative of singlet-singlet annihilation. The dynamics in the WT at these wavelengths precisely mirror the data from PSI-only membranes presented in Figure 6.3.

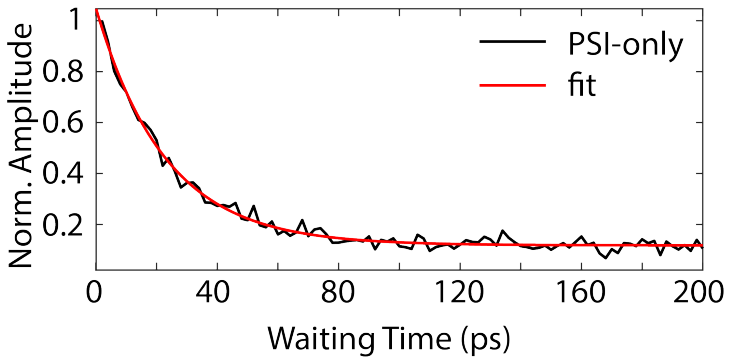

Figure 6.6: Long time dynamics in PSI-only thylakoids show consistent decay dynamics across detection wavelength. The decay kinetics at 705 nm (black) were fit to a monoexponential with an offset (red). The decay constant was ∼22 ps.

6.5 Conclusions and Future Work

We observe power-dependence dynamics at short waiting times (300 fs to 10 ps) in both PSI-only and WT thylakoids prepared from *Synechocystis* sp. PCC 6803 cells. These power-dependent dynamics offer new insight into long-range connectivity of PSI monomers in the membrane and, specifically, the connectivity of the red Chl pools between monomers. We attribute the power-dependent dynamics observed in our TA studies to singlet-singlet annihilation. On this timescale, we apply a diffusion-limited model of trapping to explain the inter-complex transfer occurring between red Chl pools. Though it has been suggested that on a longer (10s of picoseconds) timescale, dynamics in PSI are trap-limited, the diffusion-limited model can explain the dynamics we observe at the red Chl pool. These observations offer new insights into the role of the red Chl pool and the spatial distances excitations can travel within or between PSI trimers before being trapped by the RC.

While the femtosecond transient absorption experiments described in this Chapter can give insight into inter-complex hopping times, our analysis is confounded by the lack of spectral resolution in excitation wavelength. Repeating these studies using 2DES, which has spectral resolution in both excitation and detection wavelengths, would greatly strengthen the conclusions we are able to draw about inter-complex hopping and connectivity in the

thylakoid membrane. Similar studies using power-dependent 2DES experiments to map long range membrane architecture in living *Rhodobacter sphaeroides* have been successful in determining the number of connected light-harvesting complexes that make up the photosynthetic functional unit in that organism. [17]

REFERENCES

[1] L. Bar-Eyal, A. Shperberg-Avni, Y. Paltiel, N. Keren, and N. Adir. Light harvesting in cyanobacteria: The phycobilisomes. 2018.

[2] J. J. van Thor, C. W. Mullineaux, H. C. P. Matthijs, and K. J. Hellingwerf. Light harvesting and state transitions in cyanobacteria. *Botanica Acta*, 111(6):430–443, 1998.

[3] L. DiMagno, C. K. Chan, Y. Jia, M. J. Lang, J. R. Newman, L. Mets, G. R. Fleming, and R. Haselkorn. Energy transfer and trapping in Photosystem I reaction centers from cyanobacteria. *Proceedings of the National Academy of Sciences*, 92(7):2715, 1995.

[4] R. van Grondelle. Excitation energy transfer, trapping and annihilation in photosynthetic systems. *Biochimica et Biophysica Acta (BBA) - Reviews on Bioenergetics*, 811(2):147–195, 1985.

[5] Bas Gobets and Rienk van Grondelle. Energy transfer and trapping in Photosystem I. *Biochimica et Biophysica Acta (BBA) - Bioenergetics*, 1507(1):80–99, 2001.

[6] Navassard V. Karapetyan, Alfred R. Holzwarth, and Matthias Rögner. The Photosystem I trimer of cyanobacteria: molecular organization, excitation dynamics and physiological significance. *FEBS Letters*, 460(3):395–400, 1999.

[7] Karapetyan N.V., Schlodder E., van Grondelle R., and Dekker J.P. The long wavelength chlorophylls of Photosystem I. 24, 2006.

[8] Yumin Lee, Michael Gorka, John H. Golbeck, and Jessica M. Anna. Ultrafast energy transfer involving the red chlorophylls of cyanobacterial Photosystem I probed through two-dimensional electronic spectroscopy. *Journal of the American Chemical Society*, 140(37):11631–11638, 2018.

[9] J. M. Hayes, S. Matsuzaki, M. Rätsep, and G. J. Small. Red chlorophyll *a* antenna states of Photosystem I of the cyanobacterium *Synechocystis* sp. PCC 6803. *The Journal of Physical Chemistry B*, 104(23):5625–5633, 2000.

[10] Yasufumi Umena, Keisuke Kawakami, Jian-Ren Shen, and Nobuo Kamiya. Crystal structure of oxygen-evolving Photosystem II at a resolution of 1.9 Å. *Nature*, 473(7345):55–60, 2011.

[11] Jie Pan, Andrius Gelzinis, Vladimir Chorošajev, Mikas Vengris, S. Seckin Senlik, Jian-Ren Shen, Leonas Valkunas, Darius Abramavicius, and Jennifer P. Ogilvie. Ultrafast energy transfer within the Photosystem II core complex. *Physical Chemistry Chemical Physics*, 19(23):15356–15367, 2017.

[12] Yutaka Shibata, Shunsuke Nishi, Keisuke Kawakami, Jian-Ren Shen, and Thomas Renger. Photosystem II does not possess a simple excitation energy funnel: Time-resolved fluorescence spectroscopy meets theory. *Journal of the American Chemical Society*, 135(18):6903–6914, 2013.

[13] V. Barzda, V. Gulbinas, R. Kananavicius, V. Cervinskas, H. van Amerongen, R. van Grondelle, and L. Valkunas. Singlet–singlet annihilation kinetics in aggregates and trimers of LHCII. *Biophysical Journal*, 80(5):2409–2421, 2001.

[14] Craig MacGregor-Chatwin, Melih Sener, Samuel F. H. Barnett, Andrew Hitchcock, Meghan C. Barnhart-Dailey, Karim Maghlaoui, James Barber, Jerilyn A. Timlin, Klaus Schulten, and C. Neil Hunter. Lateral segregation of Photosystem I in cyanobacterial thylakoids. *The Plant Cell*, 29(5):1119, 2017.

[15] Armin Bundle Havlin and Shlomo. Fractals and disordered systems. 1996.

[16] Alfred R. Holzwarth, Günther Schatz, Helmuth Brock, and Edith Bittersmann. Energy transfer and charge separation kinetics in Photosystem I: Part 1: Picosecond transient

absorption and fluorescence study of cyanobacterial Photosystem I particles. *Biophysical Journal*, 64(6):1813–1826, 1993.

[17] Peter D. Dahlberg, Po-Chieh Ting, Sara C. Massey, Marco A. Allodi, Elizabeth C. Martin, C. Neil Hunter, and Gregory S. Engel. Mapping the ultrafast flow of harvested solar energy in living photosynthetic cells. *Nature Communications*, 8(1):988, 2017.

CHAPTER 7

FUTURE DIRECTIONS

Many exciting experiments remain now that we have extended *in vivo* GRAPES capabilities to oxygenic phototrophes. Maintaining native membrane architecture and keeping the functional photosynthetic units intact becomes increasingly important in these more complicated systems. The first two proposed experiments in this Chapter explore ultrafast energy transfer pathways in living oxygenic phototrophes (green algae and cyanobacteria) as a result of changing light conditions. Photoprotective and adaptive strategies in these organisms are extremely important to their evolutionary fitness and demand *in vivo* studies to preserve dynamics. The final proposed experiment offers an extension of the study of engineering vibronic coherence into a molecular light harvesting construct presented in Chapter 4. This proposed experiment will investigate the role of vibronic coupling and coherence on energy transfer in a heterodimer of cyanine dyes on a DNA scaffold.

7.1 Photoprotective Quenching in LHCII of Green Algae

Photosynthetic organisms have evolved a set of photoprotective mechanisms to avoid photodamage to their cellular machinery as a result of excess sunlight. Excess light can form excited chlorophyll triplets that react with triplet oxygen in the atmosphere to form singlet oxygen, which will cause severe oxidative damage to photosynthetic proteins. In plants and green algae, short-term molecular adaptation mechanisms to safely dissipate excess excitation energy as heat are known as non-photochemical quenching (NPQ) of chlorophyll fluorescence. [1] Fast, reversible quenching that can be activated within seconds is called qE (energy-dependent quenching). The qE feedback loop, which is triggered by low lumen pH ($\sim$pH 5.8 and below) as a result of a buildup of excitation energy in the membrane, initiates conformational changes in the core light-harvesting antenna (LHCII). These changes rear-

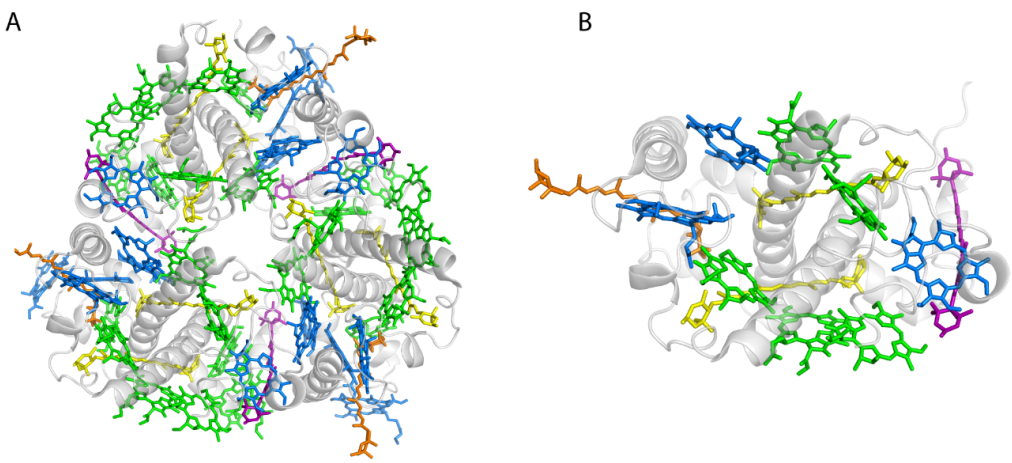

Figure 7.1: (A) LHCII trimer viewed normal to the stromal side of the thylakoid membrane. (B) An LHCII monomer. Each monomer contains five Chl *a* molecules (green), three Chl *b* molecules (blue), and four carotenoids: two luteins (yellow), one neoxanthin (orange), and one xanthophyll (purple). Crystal structure from [3] (PDB ID: IRWT).

range the pigments to optimize quenching excited chlorophylls and dissipating excess energy through non-radiative processes. [2]

LHCII is a pigment protein complex that exists as a trimer in the thylakoid membrane. [1] Figure 7.1A shows the crystal structure of trimeric LHCII. Each monomer of LHCII contains five chlorophyll *a* (Chl *a*) molecules and 3 chlorophyll *b* (Chl *b*) molecules. Chl *b* is an accessory light harvesting pigment which funnels energy into Chl *a* as part of a downhill energy transfer cascade. [1] This transfer occurs with a rate constant k_{ba}= 0.2 ps^{-1} (a transfer lifetime of 5 ps). Excitation energy transfer between Chl *a* and Chl *b* pigments in LHCII can be described by Förster resonance energy transfer (FRET). [4]

Each LHCII monomer also contains four carotenoids. Carotenoids are additional pigment molecules that provide structural integrity to the antenna complex, absorb light in

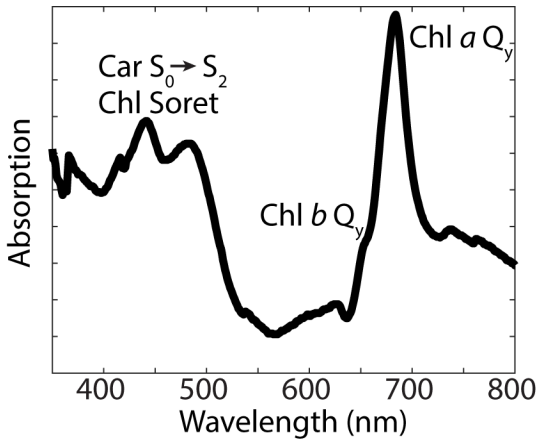

Figure 7.2: The linear absorption spectrum of *C. reinhardtii* cells. Spectral features are attributed to chlorophyll and carotenoid transitions. Starter cultures for these cells were sent to our group from Prof. Roberta Croce's group at VU Amsterdam (Netherlands).

complementary regions of the spectrum to chlorophyll, and play a role in photoprotective mechanisms. [3, 5] Figure 7.1B shows an LHCII monomer with the discussed Chl *a* (green) and Chl *b* (blue) molecules and carotenoids. The carotenoid lutein is shown in yellow, neoxanthin in orange, and xanthophyll shown in purple. Each carotenoid is 5 to 6 Å from the nearest Chl *a* molecule.

Carotenoid pigments have long conjugated, polyene chains. All-trans carotenoids have C_{2h} symmetry giving their ground state (S_0) and lowest excited state (S_1) the same Ag_- symmetry. As a result, the S_0 to S_1 transition is symmetry forbidden (both states have gerade symmetry) and the lowest optically allowed transition is S_0 to S_2. [6] The S_2 state, unlike the S_0 and S_1 states, has ungerade symmetry (Bu_+). The S_0 to S_2 transition is strongly allowed and gives rise to the characteristic linear absorption feature of carotenoids in the blue-green region of the spectrum. Figure 7.2 shows the linear absorption spectrum of the green algae *Chlamydamonas reinhardtii*, and denotes the carotenoid S_0 to S_2 absorption as well as the Chl *a* and Chl *b* spectral features.

Under normal light conditions, after an S_0 to S_2 absorption event, the carotenoid can transfer energy into a Chl *a* or Chl *b* Q_y state or relax into the dark S_1 state via internal

conversion. S_2 to S_1 internal conversion occurs within a couple hundred femtoseconds. Subsequent S_1 to S_0 relaxation occurs within 10 ps. [6] Compared to the ∼2 ns *in vivo* lifetime of singlet excited chlorophyll [4], the carotenoid S_1 state is short lived, making a carotenoid a strong candidate as a quencher for chlorophyll fluorescence during photoprotection.

The carotenoid (Car) dark S_1 state has been proposed to be a direct quencher of chlorophyll fluorescence during NPQ, but whether or not this direct energy transfer from the Chl Q_y state to the Car S_1 state occurs is still under contention in the field. [1, 7–10] The conformational rearrangement that occurs in LHCII to shift the organism from efficiently harvesting incident excitations to efficiently quenching incident excitations can affect the capacity for Chl Q_y to Car S_1 transfer by either spatially moving a carotenoid closer to neighboring Chl molecules or altering the energy of the S_1 state due to chemical modification or local solvation changes. Transient absorption spectroscopy experiments [7] have been able to indirectly measure Chl to Car energy transfer by selectively exciting chlorophyll and probing the carotenoid S_1 to S_n transition, where S_n is a higher lying excited state of Bu_+ symmetry. [6] However, the lack of sufficient spectral resolution to identify which pigments are involved (and the coupling between them) and temporal resolution to resolve dynamics within 200 fs in these experiments have precluded direct observation of the transfer dynamics through the dark S_1 state as a means of photoprotective quenching.

The proposed experiments involve the measurement of photoprotective control mechanisms and dynamics in living green algae *Chlamydamonas reinhardtii*. Such measurements have high experimental demands. Fast temporal resolution is needed to resolve femtosecond energy transfer dynamics. Broad spectral coverage with high resolution is required in order to resolve contributions from the chlorophyll and carotenoid pigments involved in excitation transfer dynamics. Resolution of energies along excitation and detection axes is important in order to directly observe energy transfer from Chl Q_y to another pigment. Short acquisition times are critical to collecting data which reflect qE dynamics, as after ∼1 hr a cell will stop

using qE as its quenching mechanism and implement a more long-term control strategy. The ability to control the scatter present in *in vivo* samples is also necessary since these organisms must stay intact to maintain their photoprotective mechanisms. *In vivo* GRAPES presents a method for uncovering the quenching mechanism in LHCII.

7.2 Ultrafast Manifestations of State Transitions in Living Cyanobacteria

Chapter 5 presents the first 2DES spectra of living cyanobacterial cells. This technical advance opens up many questions that can only be answered through *in vivo* ultrafast measurements. One question that has been previously inaccessible by conventional techniques is the ultrafast dynamics of *State 1* and *State 2*.

Cyanobacteria use bilin pigments in their phycobilisomes (PBS) and chlorophyll pigments in their fused antenna/reaction center complexes, Photosystem I (PSI) and Photosystem (II), to harvest solar excitations. Both the PBS and the photosystems can capture solar photons. It has been reported that PBSs are mainly associated with PSII on the cytoplasmic side of the thylakoid membrane, but they are extremely mobile and can freely dissociate from the membrane and associate with either photosystem. [11] Excitations are funneled to the reaction centers in PSI and PSII where photochemistry occurs to produce biomass. [12] The quality (spectral composition) of the incident light determines the relative number of excitations that make it to the P700 reaction center (RC) of PSI and the P680 reaction center of PSII. Light quality can vary instantaneously as a function of cloud cover or other weather conditions. The number of excitations that reach each RC is determined by the association between PBSs and each of the photosystems. *State 1* occurs upon illumination with blue or far-red light and *State 2* occurs upon illumination with orange-green light or upon dark adaptation. [13] In *State 1*, PSI is preferentially excited and in *State 2*, PSII is preferentially excited. *State 1* and *State 2* are differentiated experimentally using the PSII

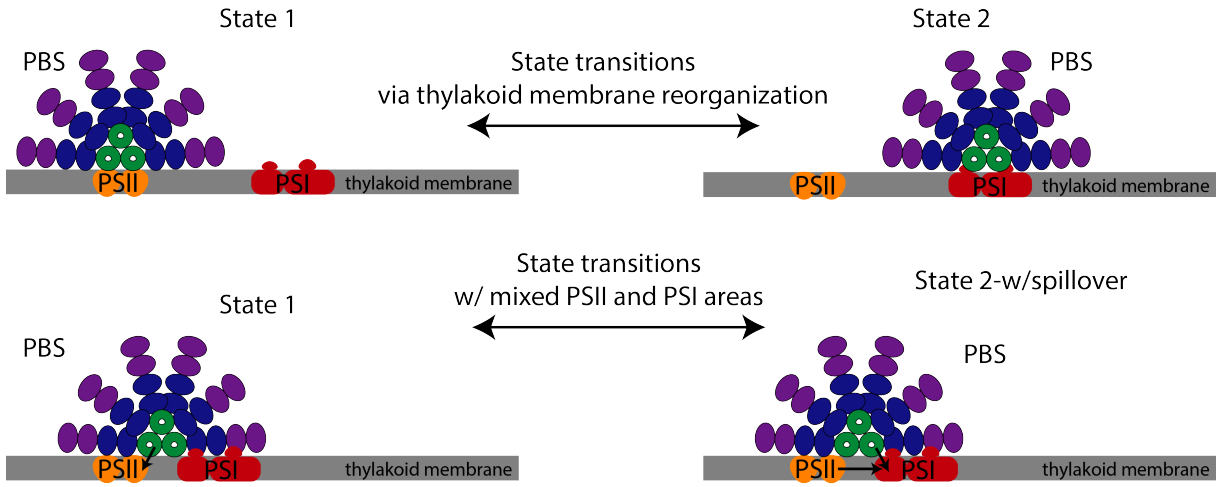

Figure 7.3: A comparison of the two proposed mechanisms for state transitions in cyanobacteria. (Top) State transitions occur through membrane reorganization. The PBS can shuttle bewteen PSI and PSII depending on incident illumination quality. (Bottom) The PBS and both photosystems form a megacomplex. Changes in incident illumination change the spectral overlap between the PBS and the photosystems resulting in *State 1* or *State 2*. In *State 2*, there is transfer from the PBS to PSI and spillover from PSII, which has been directly excited, to PSI.

fluorescence quantum yield. *State 1* is associated with high PSII fluorescence. In *State 1*, the absorption cross-section of PSI and the PBS is reduced leading to no association between these two complexes. It is also possible to bring the cells to a state intermediate between states 1 and 2 using yellow-orange light. [13, 14]

Two models have been proposed to explain state transitions in cyanobacteria. The first involves a reversible migration of the PBS between PSI and PSII. [15] The second, called the "spill-over" model, involves energy transfer between PSI and PSII and does not rely on the PBS to explain the difference between *State 1* and *State 2*. [16, 17] Figure 7.3 depicts the mechanics of the photosynthetic complexes during these two scenarios to explain the photophysical differences between states 1 and 2.

Currently, characterizations of dynamical differences between *State 1* and *State 2* are determined using time-resolved fluorescence measurements. [12, 14, 16–18]. These measurements are limited to a timescale of several picoseconds and do not offer spectral resolution

in excitation wavelength or pathway information. Our *in vivo* GRadient-Assisted Photon Echo Spectroscopy (GRAPES) offers a path to determining the ultrafast dynamical differences in *State 1* and *State 2*. We can use GRAPES to track energy migration from the distal pigments of the PBS rods to each of the photosynthetic RCs. In doing so, we will be able to track relative trapping by P700 and P680 in different light conditions. Due to the spatial overlap of PSI and PSII features in the 2D spectrum (see Chapter 5), this could present an experimental challenge. A strategy to mitigate the assignment of features in the 2D spectrum is to develop a 2-color iteration of the GRAPES setup. The interpretation of experimental results on living cyanobacterial cells would be simplified if we could only excite the distal phycocyanin and phycoerythrin pigments in the PBS rods, then detect at the transition frequency of PSI and PSII. A 2-color experiment should be able differentiate between the two proposed mechanisms of state transition mechanics. We can also expose the cells to different light conditions during the measurement. We do not have to solely rely on adaptation of the cells prior to the measurement and then run the measurement in the dark or at cryogenic temperatures. We have developed a box in which we can put the reservoir of cells that are continuously flowing through our measurement sample cell in GRAPES that is equipped with LED lights. These LED lights can be set to many different colors, giving us the flexibility to switch between several light conditions with ease (Figure 7.4). The relative trapping by P700 and P680 in *State 1* and *State 2* is of utmost interest to the photosynthetic community and *in vivo* GRAPES is the only technique that offers a path forward to determine the relative trapping ratio.

7.3 Vibronic Coherence and Ultrafast Energy Transfer in a Dye-DNA Construct

In Chapter 4, we showed that a DNA scaffold can support long-lived vibronic coherence in a indocarbocyanine (Cy5) homodimer. We did not, however, explore how vibronic coherence

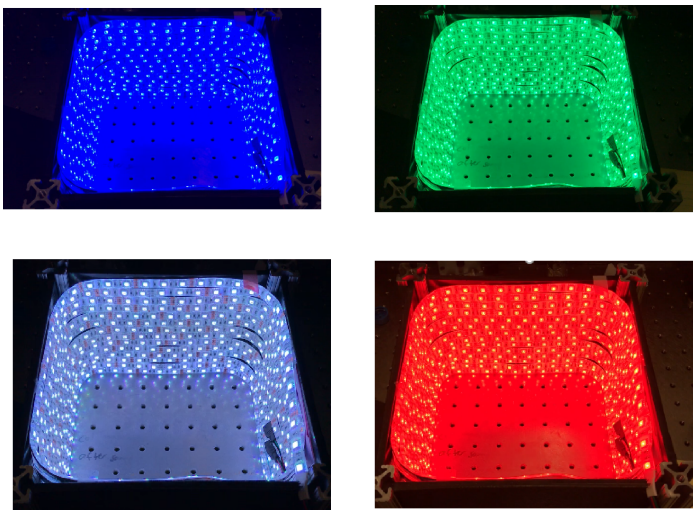

Figure 7.4: Strips of LED lights line a plastic box that is mounted on the laser table proximal to the GRAPES setup. The reservoir for the flow cell used in a GRAPES measurement is placed within the box. The LEDs can be set to any color. Blue, green, white, and red are shown as examples. This setup presents a modular mechanism for invoking *State 1* or *State 2* in living cyanobacteria.

can be exploited to optimize energy transfer in a DNA-based synthetic system. Many of the long-lived quantum coherences observed in photosynthetic pigment-protein complexes have been assigned as vibronic coherences. [19–26] A vibronic coherence involves a quantum superposition between an electronic excited state on one molecule and an underdamped vibrational mode on another molecule. The coupling between the electronic excited state and the vibrational mode is known as vibronic coupling. It has been suggested that vibronic coupling in photosynthetic pigment-protein complexes is responsible for the efficient energy transfer observed in biosystems. [27, 28]

Proposed work will study a heterodimer of cyanine dyes attached at a small separations on a double-stranded (dsDNA) scaffold. Since we have already observed vibronic coherence in Cy5 dimers, we propose to use Cy5 and Cy5.5 to form the heterodimer. Cy5.5 absorption falls just red of Cy5 absorption and they are commonly used as a FRET pair in biological studies. [29, 30] At small base pair separations on a DNA scaffold, FRET transfer breaks down and we see evidence quantum coherent behavior. [31] The proposed experiments would

explore the effects of strong vibronic coupling on ultrafast energy transfer on a DNA scaffold.

The linear absorption spectra of the Cy5-Cy5.5 heterodimer at 0, 1, 2, and 3 bp separations are shown in Figure 7.5. Constructs with the dyes separated at 0, 1, and 2 bp show evidence of molecular aggregates and the progressive deviations from the 3 bp separated spectrum with smaller dye separations. At a separation of 3 bp on the dsDNA scaffold, the two dyes should behave classically, with FRET transfer between them. [31] Specifically, the 0 bp separated heterodimer shows a large redistribution of oscillator strength to the highest energy transition near 600 nm. While absorption is present near 600 nm in the 1 bp, 2 bp, and 3 bp separated heterodimers, the transition carries little oscillator strength. Coupling between the excitonic and vibrational states on the two dyes creates the set of vibronic exciton states that give rise to the drastically different linear absorption spectra at different inter-dye separations. We will apply the vibronic exciton model presented in Chapter 4 to calculate the vibronic states in the heterodimers at these base pair separations. The linear absorption spectra in Figure 7.5 indicate that a heterodimer with 3 bp separating the two cyanine dyes could serve as a control. In this construct, we expect to see incoherent hopping (FRET) as the mechanism for ultrafast energy transfer.

The 0 bp, 1bp, and 2 bp dimers all show deviation from what a summed spectra of a Cy5 monomer and a Cy5.5 monomer would give. This series of construct can be used to study the effect of coupling strength on coherence and energy transfer in a DNA-based synthetic system. I expect that energy transfer dynamics between the vibronic exciton states will be extremely fast (10s-100s of fs) due to the strong excitonic coupling between the dyes. Beating frequency analysis of observed coherences will lend insight into the role of vibronic coherence in mediating ultrafast energy transfer. The 0 bp separated heterodimer would be a strong candidate to look for coherence transfer in a synthetic system. Coherence transfer would manifest as a coherence (likely of vibronic origin in this construct) that transfers between excited state surfaces as energy transfer occurs. Developing artificial molecular

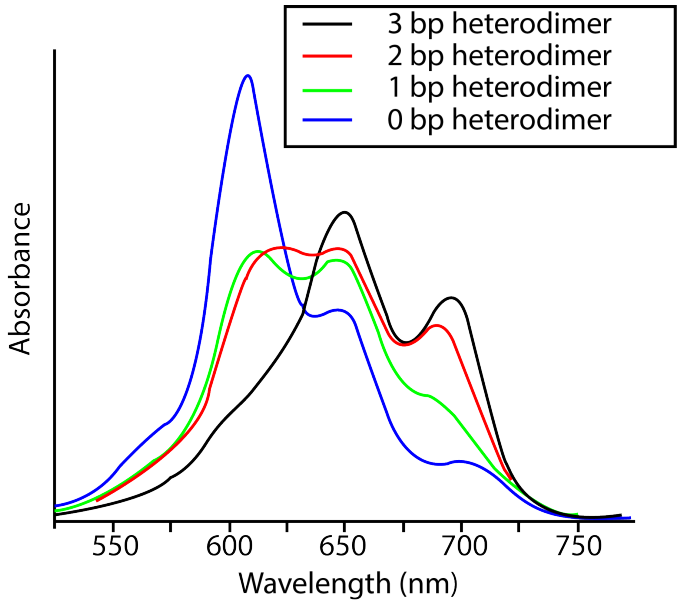

Figure 7.5: Linear absorption spectra of Cy5-Cy5.5 heterodimers on a DNA scaffold at 3 bp (black), 2 bp (red), 1bp (green), and 0 bp (blue) separations. An increase in excitonic coupling between the dyes occurs at smaller inter-dye separations and is accompanied by larger deviations in the linear absorption spectra from the monomeric signatures of Cy5 and Cy5.5. The 0 bp, 1 bp, and 2 bp constructs show signatures of molecular aggregates.

light-harvesting systems that mimic photosynthetic design principles is an important step in developing robust, efficient synthetic light-harvesting tools.

REFERENCES

[1] Zhenfeng Liu, Hanchi Yan, Kebin Wang, Tingyun Kuang, Jiping Zhang, Lulu Gui, Xiaomin An, and Wenrui Chang. Crystal structure of spinach major light-harvesting complex at 2.72 Å resolution. *Nature*, 428(6980):287–292, 2004.

[2] Julia Zaks, Kapil Amarnath, David M. Kramer, Krishna K. Niyogi, and Graham R. Fleming. A kinetic model of rapidly reversible nonphotochemical quenching. *Proceedings of the National Academy of Sciences of the United States of America*, 109(39):15757–15762, 2012.

[3] Robert E. Blankenship. *Molecular Mechanisms of Photosynthesis*. John Wiley & Sons, Ltd, Chinchester, West Sussex, 2nd edition, 2014.

[4] Roberta Croce and Herbert van Amerongen. Natural strategies for photosynthetic light harvesting. *Nat Chem Biol*, 10(7):492–501, 2014.

[5] Tomáš Polívka and Villy Sundström. Ultrafast dynamics of carotenoid excited states-from solution to natural and artificial systems. *Chemical Reviews*, 104(4):2021–2072, 2004.

[6] Baldassare Di Bartolo and Ottavio Forte. *Frontiers of optical spectroscopy: investigating extreme physical conditions with advanced optical techniques*, volume 168 of *NATO science series. Series II, Mathetmatics, physics, and chemistry*. Springer, Dordrecht, 2005.

[7] Ying-Zhong Ma, Nancy E. Holt, Xiao-Ping Li, Krishna K. Niyogi, and Graham R. Fleming. Evidence for direct carotenoid involvement in the regulation of photosynthetic light harvesting. *Proceedings of the National Academy of Sciences*, 100(8):4377–4382, 2003.

[8] Krishna K. Niyogi and Thuy B. Truong. Evolution of flexible non-photochemical quenching mechanisms that regulate light harvesting in oxygenic photosynthesis. *Current Opinion in Plant Biology*, 16(3):307–314, 2013.

[9] A. V. Ruban, M. P. Johnson, and C. D. Duffy. The photoprotective molecular switch in the Photosystem II antenna. *Biochim Biophys Acta*, 1817(1):167–81, 2012.

[10] Alexander V. Ruban, Rudi Berera, Cristian Ilioaia, Ivo H. M. van Stokkum, John T. M. Kennis, Andrew A. Pascal, Herbert van Amerongen, Bruno Robert, Peter Horton, and Rienk van Grondelle. Identification of a mechanism of photoprotective energy dissipation in higher plants. *Nature*, 450(7169):575–578, 2007.

[11] Mai Watanabe and Masahiko Ikeuchi. Phycobilisome: architecture of a light-harvesting supercomplex. *Photosynthesis Research*, 116(2):265–276, 2013.

[12] Reza Ranjbar Choubeh, Emilie Wientjes, Paul C. Struik, Diana Kirilovsky, and Herbert van Amerongen. State transitions in the cyanobacterium *Synechococcus elongatus* 7942 involve reversible quenching of the Photosystem II core. *Biochimica et Biophysica Acta (BBA) - Bioenergetics*, 1859(10):1059–1066, 2018.

[13] Diana Kirilovsky. Modulating energy arriving at photochemical reaction centers: orange carotenoid protein-related photoprotection and state transitions. *Photosynthesis Research*, 126(1):3–17, 2015.

[14] Conrad W. Mullineaux and John F. Allen. State 1-State 2 transitions in the cyanobacterium *Synechococcus* 6301 are controlled by the redox state of electron carriers between Photosystems I and II. *Photosynthesis Research*, 23(3):297–311, 1990.

[15] Conrad W. Mullineaux. Excitation energy transfer from phycobilisomes to Photosystem I in a cyanobacterium. *Biochimica et Biophysica Acta (BBA) - Bioenergetics*, 1100(3):285–292, 1992.

[16] Doug Bruce, Scott Brimble, and Donald A. Bryant. State transitions in a phycobilisomeless mutant of the cyanobacterium *Synechococcus* sp. PCC 7002. *Biochimica et Biophysica Acta (BBA) - Bioenergetics*, 974(1):66–73, 1989.

[17] C. Vernotte, C. Astier, and J. Olive. State 1-state 2 adaptation in the cyanobacteria *Synechocystis* PCC 6714 wild type and *Synechocystis* PCC 6803 wild type and phycocyanin-less mutant. *Photosynthesis Research*, 26(3):203–212, 1990.

[18] Volha Chukhutsina, Luca Bersanini, Eva-Mari Aro, and Herbert van Amerongen. Cyanobacterial light-harvesting phycobilisomes uncouple from Photosystem I during dark-to-light transitions. *Scientific Reports*, 5(1):14193, 2015.

[19] Aurélia Chenu, Niklas Christensson, Harald F. Kauffmann, and Tomáš Mančal. Enhancement of vibronic and ground-state vibrational coherences in 2D spectra of photosynthetic complexes. *Scientific Reports*, 3:2029, 2013.

[20] E. Collini, C. Y. Wong, K. E. Wilk, P. M. Curmi, P. Brumer, and G. D. Scholes. Coherently wired light-harvesting in photosynthetic marine algae at ambient temperature. *Nature*, 463(7281):644–7, 2010.

[21] Peter D. Dahlberg, Graham J. Norris, Cheng Wang, Subha Viswanathan, Ved P. Singh, and Gregory S. Engel. Communication: Coherences observed *in vivo* in photosynthetic bacteria using two-dimensional electronic spectroscopy. *The Journal of Chemical Physics*, 143(10):101101, 2015.

[22] Marco Ferretti, Vladimir I. Novoderezhkin, Elisabet Romero, Ramunas Augulis, Anjali Pandit, Donatas Zigmantas, and Rienk van Grondelle. The nature of coherences in the B820 bacteriochlorophyll dimer revealed by two-dimensional electronic spectroscopy. *Physical Chemistry Chemical Physics*, 16(21):9930–9939, 2014.

[23] M. L. Flanagan, P. D. Long, P. D. Dahlberg, B. S. Rolczynski, S. C. Massey, and G. S. Engel. Mutations to *R. sphaeroides* reaction center perturb energy levels and vibronic coupling but not observed energy transfer rates. *J Phys Chem A*, 120(9):1479–87, 2016.

[24] Franklin D. Fuller, Jie Pan, Andrius Gelzinis, Vytautas Butkus, S. Seckin Senlik, Daniel E. Wilcox, Charles F. Yocum, Leonas Valkunas, Darius Abramavicius, and Jennifer P. Ogilvie. Vibronic coherence in oxygenic photosynthesis. *Nat Chem*, 6(8):706–711, 2014.

[25] G. S. Schlau-Cohen, A. Ishizaki, T. R. Calhoun, N. S. Ginsberg, M. Ballottari, R. Bassi, and G. R. Fleming. Elucidation of the timescales and origins of quantum electronic coherence in LHCII. *Nat Chem*, 4(5):389–95, 2012.

[26] V. Tiwari, W. K. Peters, and D. M. Jonas. Electronic resonance with anticorrelated pigment vibrations drives photosynthetic energy transfer outside the adiabatic framework. *Proc Natl Acad Sci U S A*, 110(4):1203–8, 2013.

[27] A. W. Chin, J. Prior, R. Rosenbach, F. Caycedo-Soler, S. F. Huelga, and M. B. Plenio. The role of non-equilibrium vibrational structures in electronic coherence and recoherence in pigment–protein complexes. *Nature Physics*, 9(2):113–118, 2013.

[28] V. Tiwari, W. K. Peters, and D. M. Jonas. Energy transfer: Vibronic coherence unveiled. *Nat Chem*, 6(3):173–5, 2014.

[29] Sungchul Hohng, Chirlmin Joo, and Taekjip Ha. Single-molecule three-color FRET. *Biophysical Journal*, 87(2):1328–1337, 2004.

[30] Susan Buckhout-White, Christopher M. Spillmann, W. Russ Algar, Ani Khachatrian, Joseph S. Melinger, Ellen R. Goldman, Mario G. Ancona, and Igor L. Medintz. Assembling programmable FRET-based photonic networks using designer DNA scaffolds. *Nature Communications*, 5(1), 2014.

[31] Paul D. Cunningham, Young C. Kim, Sebastián A. Díaz, Susan Buckhout-White, Divita Mathur, Igor L. Medintz, and Joseph S. Melinger. Optical properties of vibronically coupled Cy3 dimers on dna scaffolds. *The Journal of Physical Chemistry B*, 122(19):5020–5029, 2018.

CHAPTER 8

CONCLUSIONS

Photosynthetic organisms use networks of coupled pigments perfected by billions of years of evolution to capture solar photons with unparalleled efficiency. These pigment networks maximize charge separation under low light conditions and dissipate excess excitations in high light. This thesis has lent new photophysical insight into the strategies employed by *Rhodobacter sphaeroides* and *Synechocystis* sp. PCC 6803 to funnel excitations to their reaction centers with minimal losses. Additionally, the work presented in this thesis demonstrates how we can take a photosynthetic design principle, long-lived vibronic coherence, and engineer it into a synthetic system for potential artificial light-harvesting applications. The technical advances made to the GRAPES instrumentation have made it possible to analyze two-dimensional lineshapes in living cells and acquire the first two-dimensional electronic spectra of a living oxygenic phototroph.

I adapted *in vivo* GRAPES to recover absorptive lineshapes in living *Rba. sphaeroides* cells. Two-dimensional lineshape analysis of these fully absorptive spectra reveal an ultrafast intracomplex relaxation within the B875 band of LH1 *in vivo*. Higher lying excitonic states in the B875 manifold maximize spectral overlap with the B850 band of LH2 and the subsequent sub-100 fs relaxation prevents back transfer. Our lineshape analysis also reveals a decrease in dipole strength of a strong transition in LH1 on the red side of the B875 band. This decrease in dipole strength is due to rapid localization of an initially delocalized exciton, further frustrating back transfer between B875 to B850.

Vibronic coupling has been purported as the design principle responsible for long-lived vibronic coherence in photosynthetic pigment-protein complexes. We use vibronically coupled Cy5 dyes on a DNA scaffold to investigate if such a molecular design can support long-lived vibronic coherences. Beating frequency analysis of 2DES data reveal high frequency oscillations in Cy5 homodimers separated by 0 bp and 1 bp on the DNA scaffold. We assign

these spectral oscillations to coherences between vibronic exciton states. Our conclusions are supported by a vibronic exciton model that calculates the transition energies of the vibronic exciton states in the dimers. The observed vibronic coherences persist for hundreds of femtoseconds, establishing DNA as an attractive scaffold for synthetic light-harvesting applications.

I acquired the first two-dimensional spectrum of a living cyanobacterium. Cyanobacterial peripheral light-harvesting antenna dissociate from the fused antenna/reaction center complexes embedded in the thylakoid membrane upon cell disruption. *In vivo* studies are the only way to map the native energy transfer pathways from the most distal, highest energy pigments to the reaction centers. We see spectral features corresponding to all the light-harvesting and reaction center components. This was an important first step to being able to track ultrafast energy transfer dynamics in oxygenic photosynthesis.

Power-dependent transient absorption experiments revealed that trapping by the PSI reaction center in *Synechocystis* sp. PCC 6803 is trap-limited for excitations in the bulk Chl pool, but diffusion-limited for excitations in the red Chl pool. We measured inter-complex hopping times between red Chl pools on neighboring PSI monomers. The observed dynamics were conserved in thylakoids prepared from wild-type cells and PSI-only cells.

Adapting *in vivo* GRAPES for measurements on Chl-containing organisms has opened many doors to studying how living photosynthetic organisms adapt to changing environmental conditions. We will continue to improve the GRAPES instrumentation to gain higher experimental signal-to-noise and we will use mutant cell strains to parse dynamics from spectrally overlapped complexes. I have proposed experiments to study qE quenching in living green algae as a result of high light exposure and to study how *State 1* and *State 2* differ in their ultrafast energy transfer pathways in cyanobacteria. These experiments will inform on how ultrafast energy transfer dynamics respond to changes in incident illumination quality and quantity. I have also proposed future work to investigate the role of vibronic cou-

pling and vibronic coherence, important photosynthetic design principles, in energy transfer between cyanine dyes on a DNA scaffold. Turning to photosynthetic design principles in engineering synthetic systems can help make more efficient, biologically-inspired artificial light-harvesting tools.